Electron cloud formation in CERN particle accelerators and its impact on the beam dynamics

Entstehung von Elektronenwolken in den Teilchenbeschleunigern des CERN und ihre Auswirkungen auf die Strahldynamik
Zur Erlangung des akademischen Grades Doktor-Ingenieur (Dr.-Ing.)
genehmigte Dissertation von Annalisa Romano, M.Sc. aus Benevento / Italien
Tag der Einreichung: 30.04.2018, Tag der Prüfung: 20.08.2018
Darmstadt — D 17

1. Gutachten: Prof. Dr. rer. nat. Oliver Boine-Frankenheim TU Darmstadt
2. Gutachten: Prof. Dr. rer. nat. Ursula van Rienen Universität Rostock

TECHNISCHE
UNIVERSITÄT
DARMSTADT

Fachbereich Elektrotechnik
und Informationstechnik
Institut für
Theorie Elektromagnetischer Felder

Electron cloud formation in CERN particle accelerators and its impact on the beam dynamics
Entstehung von Elektronenwolken in den Teilchenbeschleunigern des CERN und ihre Auswirkungen auf die Strahldynamik

Genehmigte Dissertation von Annalisa Romano, M.Sc. aus Benevento / Italien

1. Gutachten: Prof. Dr. rer. nat. Oliver Boine-Frankenheim TU Darmstadt
2. Gutachten: Prof. Dr. rer. nat. Ursula van Rienen Universität Rostock

Tag der Einreichung: 30.04.2018
Tag der Prüfung: 20.08.2018

Darmstadt — D 17

URN: urn:nbn:de:tuda-tuprints-80716
URL: http://tuprints.ulb.tu-darmstadt.de/8071

TECHNISCHE
UNIVERSITÄT
DARMSTADT

Electron cloud formation in CERN particle accelerators and its impact on the beam dynamics

Dem Fachbereich Elektrotechnik und Informationstechnik
der Technischen Universität Darmstadt

zur Erlangung des akademischen Grades
einer Doktoringenieurin (Dr.-Ing.)
vorgelegte Dissertation

von
Annalisa Romano, M.Sc.
geboren am 28.04.1989 in Benevento

1. Gutachter: Prof. Dr. rer. nat. Oliver Boine-Frankenheim
2. Gutachter: Prof. Dr. rer. nat. Ursula van Rienen

Tag der Einreichung: 30.04.2018
Tag der mündlichen Prüfung: 20.08.2018

Darmstadt 2018
D17

Erklärung laut §9 PromO

Ich versichere hiermit, dass ich die vorliegende Dissertation allein und nur unter Verwendung der angegebenen Literatur verfasst habe. Die Arbeit hat bisher noch nicht zu Prüfungszwecken gedient.

Darmstadt, den 30.04.2018

Kurzfassung

In Beschleunigern, die positiv geladene Teilchen zu hohen Energien beschleunigen, können Photo-, und Sekundäremissionen zu exponentieller Elektronenvermehrung in der Strahlkammer führen. Daraus kann sich eine sogenannte Elektronenwolke (Electron Cloud, EC) bilden. Eine EC kann in einem Teilchenbeschleuniger für lokal auftretende Phänomene wie z.B. thermische Belastung der Kammerwände, Druckanstieg oder Rauschen in der Strahldiagnostik verantwortlich sein. Auch können elektromagnetische Kräfte die von der EC auf die Teilchen des Strahls ausgeübt werden zu einer Verminderung der Strahlqualität führen. Die vorliegende Arbeit behandelt am CERN auftretende EC Effekte mittels Simulationen und experimenteller Studien. Der Fokus liegt hierbei auf dem Large Hadron Collider (LHC) und dessen Injektor, dem Super Proton Synchotron (SPS).

Im LHC wurde die EC in den tieftemperatur Ringsegmenten als eine der Hauptlimitierungen für die Leistungsfähigkeit der Maschine ausgemacht, da sie das Wärmeschild der Magnete zusätzlich thermisch belastet. Im Rahmen der Entwicklung des Wärmeschilds für die neuen High Luminosity LHC (HL-LHC) Magnete wurden die Vakuumpumpenöffnungen abgeschirmt, um die Magnete im supraleitenden Zustand zu halten. Der Einfluss dieser Schirmung auf den Prozess der Elektronenmultiplikation wird in dieser Arbeit untersucht. Dafür wurde eine neue Funktion im PyECLOUD Code implementiert.

Neben den lokalen Effekten kann die EC auch die Strahldynamik bezüglich kohärenter und inkohärenter Effekte erheblich beeinflussen. Das Verständnis dieser Mechanismen hängt hauptsächlich von numerischen Simulationen ausgeführt mit der PyECLOUD - PyHEADTAIL Software ab. Dieser innovative Ansatz verbessert die Modellierung der durch die EC beeinflusste Strahldynamik deutlich. Erstmals konnte das Einwirken der EC auf die Strahldynamik in den Quadrupolen simuliert werden. Der Mechanismus hinter zahlreichen EC Beobachtungen während des LHC Protonen Laufs von 2015 bis 2017 konnte so analysiert werden. Zusätzlich wurden potentielle Stabilisierungstechniken untersucht.

EC Effekte sind auch ein Hauptanliegen im SPS, da dieser für das LHC Injectors Upgrade (LIU) Projekt Strahle mit höherer Intensität produzieren soll. Die vorliegende Arbeit untersucht die Effektivität einer amorphen Kohlenstoffbeschichtung, welche die Elektronenmultiplikation unterdrucken soll, anhand von numerischer Simulationen. Die Strahlkammer wird hierfür mit einem variierenden

Sekundärelektronenemissionsprofil modelliert, um eine Beschichtungen mit der hollow-cathode Methode zu reproduzieren.

Abstract

In high energy accelerators operating with positively charged particles, photoemission and secondary emission can give rise to an exponential electron multiplication within the beam chamber, which leads to the formation of a so-called Electron Cloud (EC). The formation of an EC in a particle accelerator can be responsible for local detrimental phenomena (e.g. heat load on the chamber's wall, pressure rise, noise in beam diagnostics) and for the deterioration of the beam quality due to the electromagnetic forces exerted by the EC on the beam particles. The present thesis work addresses EC effects in the CERN Large Hadron Collider (LHC) and in its injector the Super Proton Synchrotron (SPS) by means of numerical simulations and experimental studies.

At the LHC, the formation of ECs in the cryogenic arcs has been identified as one of the main limitations for the performance of the machine, due to the additional heat load deposited on the perforated beam screen. In the framework of the design of the beam screens of the new High Luminosity LHC magnets, the impact of the pumping slot shields (added to preserve the superconducting state of these magnets) on the multipacting process has been addressed by introducing new features in the PyECLOUD simulation code.

Besides these local effects, the EC can also significantly influence the beam dynamics in terms of both coherent and incoherent effects. The understanding of these phenomena heavily relies on numerical simulations carried out with the PyECLOUD-PyHEADTAL interface. This new setup offers significant improvements to the modeling of EC induced beam dynamics. Indeed, it allowed simulating for the first time the impact on the beam stability of the EC in the quadrupoles and explaining the driving mechanism of several EC observations at the LHC during the 2015-2017 proton run. Furthermore, potential mitigation techniques have been investigated.

EC effects are also found to be a major concern for the SPS, in particular for the production of the high intensity beam foreseen by the LHC Injectors Upgrade project. In this framework, the efficiency of the coating realized with a newly developed technique to suppress the electron multipacting has been investigated with numerical simulations. In this case, the beam chambers have been modeled with a non-uniform Secondary Electron Yield profile in order to reproduce the coating as achievable with the hollow cathode procedure.

Contents

Introduction

The Electron Cloud (EC) phenomenon has long been recognized as being a major limiting factor in the performance for accelerators operating with intense positively charged beams. The term EC refers to an accumulation of electrons inside the vacuum pipe of an accelerator that, if sufficiently strong, can seriously affect its operation. Primary electrons can be generated in the beam chamber by different mechanisms like residual-gas ionization or photoemission from the pipe wall induced by synchrotron radiation. The amount of electrons in the pipe can further increase due to beam-induced multipacting mechanism: electrons accelerated by the electric field of the beam impact on the chamber's wall and, if the Secondary Electron Yield (SEY) of the surface is sufficiently high, the emission of secondary electrons can trigger an avalanche multiplication process. The formation of an EC in a particle accelerator can be responsible for local detrimental phenomena (e.g. heat load on the chamber's wall, pressure rise, noise in beam diagnostics) and for the deterioration of the beam quality due to the exerting electromagnetic forces exerted on beam particles. This can lead to coherent instabilities, emittance growth, particle losses.

EC effects have been identified among the major performance limitations for the Large Hadron Collider (LHC), presently the world's largest and most powerful particle accelerator and collider. It was built by the European Organization for Nuclear Research (CERN) in a 27 km underground tunnel across the Franco-Swiss border near Geneva, Switzerland. Inside the accelerator, two counter rotating beams are guided around their circular orbit by powerful superconducting magnets (operated at a cryogenic temperature of 1.9 K) and accelerated to increasingly higher energy before colliding with one another. The aim of the LHC is to investigate the properties of the Higgs boson (discovered in 2012), consolidate the validity of the super-symmetric theories and answer other open questions about high energy physics. The present thesis addresses EC effects both in the LHC and in its injector, the Super Proton Synchrotron (SPS), by means of numerical simulations and experimental observations.

At the LHC EC effects have been observed for the first time during the Run 1 (2010-2012), becoming more and more severe when operating with tight bunch spacing of 25 ns at the beginning of the Run 2 (2015-2018). One of the major concern for the operation near and beyond nominal beam current is the heat load generated by EC in the cold magnets. While this effect is typically negligible in room temperature accelerator components, it can be a serious issue in devices operating at cryogenic temperatures, where the EC induced heat load can become compatible to the cooling capacity limit of the cryogenic system. In order to preserve the superconducting state of the magnets, pumping slot shields have been added on the outer side of the perforated beam screens. In the framework of the design of the new beam screens foreseen by the High Luminosity LHC project, we have studied the impact of these shields on the multipacting process using the PyECLOUD simulation code. For this purpose, a detailed model of the vacuum chamber, including the pumping hole and corresponding shield, has been developed. In order to allow the EC buildup simulations with the required geometry, new features had to be implemented in the simulation code.

Besides these local effects, the EC can also significantly influence the beam dynamics. When the bunch enters an EC, electrons are attracted towards the bunch center resulting into an increase electron density near the beam axis. The distortion of the EC distribution is the mechanism that couples the motion within the bunches and gives rise to coherent and incoherent effects.

Since 2015, the first year of luminosity production with 25 ns bunch spacing in the LHC, beam quality degradation due to the EC has been observed in different phases of the machine cycle. These observations included both transverse instabilities, leading to a fast emittance blow-up, and incoherent particle losses. Of particular interest has been the systematic observations of an anomalous instability at beginning of the 2016 run. The distinguishing characteristic of this instability is that it suddenly appeared while the beams were kept stably for several hours in collision at 6.5 TeV, in spite of the high chromaticity and octupoles current and of the increased beam rigidity with respect to the injection energy. The understanding of the limitations due to the EC effects is crucial not only for the presently LHC runs but also in the perspective of the planned future upgrade aiming at increasing the LHC intensity and luminosity. For this reason, an extensive simulation campaign has been carried out with a recently developed interface that combines PyECLOUD with the PyHEADTAIL beam dynamics code. This setup offers significant improvements to the modeling of EC induced beam dynamics. An obstacle that prevented from benefiting fully from the capabilities of this new approach was the impractically long run-times required to approach the time scale of the machine observations (instability rise time of the order of 10^4 turns). In order to be able to study the effects observed in the LHC, new advanced features had to be therefore included in the codes and parallel computing resources had to be exploited. This allowed simulating different effects of the EC on the beam dynamics in increasingly complex scenarios and for longer simulation spans, which were previously inaccessible. For example it was possible to study EC driven instabilities for the nominal LHC at collision energy.

EC effects are also found to be a major concern for the SPS, in particular for the production of the high intensity beam foreseen by the LHC Injectors Upgrade project. While beam induced surface conditioning (scrubbing) has proved successful for the production of the nominal LHC beams, the high intensity beams were found to still suffer from strong EC effects. Thus, it was decided to apply amorphous carbon (a-C) coatings to the critical components in the SPS ring by means of a newly developed *in-situ* technique, called hollow-cathode sputtering. The efficiency of the coating realized with this technique has been addressed with PyECLOUD simulations for the MBA and MBB dipole magnets and for the QF quadrupole magnets. The main feature of these simulations is that, in order to reproduce the coating as achievable with the hollow cathode procedure, the beam chambers were needed to be modeled with a non-uniform SEY profile.

The present work has the following structure. Chapter 1 introduces the mechanisms involved in the EC formation and describes the main features of the numerical codes used for the simulation studies. Chapter 2 focuses on the studies of the EC formation process (buildup) in the LHC and SPS. Chapter 3 presents simulation and experimental studies on coherent instabilities due to EC in the LHC. Particular emphasis is put on the description of encountered limitations and potential mitigation strategies. Finally, incoherent effects are discussed in Chap. 4.

1 Electron cloud in particle accelerators: basic concepts and simulation tools

When electrons with sufficient kinetic energy impinge on the surface of a solid, emission of secondary electrons by the solid may be observed. This phenomenon, known as secondary electron emission, was discovered by Austin and Stark [1] more than 100 years ago. In particle accelerators operating with closely spaced positron or proton bunches, secondary electron emission in resonance with the time-varying electric field from the beam can give rise to an exponential electron multiplication within the beam chamber. This multipactor effect leads to the formation of the so called EC. The presence of a large electron density in the beam pipe is responsible for various unwanted effects like beam instabilities, transverse emittance growth, dynamic pressure rise and heating of the chamber's surface [2, 3, 4].

Since 1965 [5] these effects are considered among the major limiting performance factors for many high energy circular accelerators around the world as the DAΦNE electron positron collider in Italy [6], the KEKB electron positron machine in Japan [7], the CERN SPS and, more recently, the CERN LHC [8]. EC related effects observed in the LHC and SPS will be extensively discussed in this work. In the present chapter we will introduce the different mechanisms involved in the formation of an EC and the simulation codes used to perform the studies presented in this thesis.

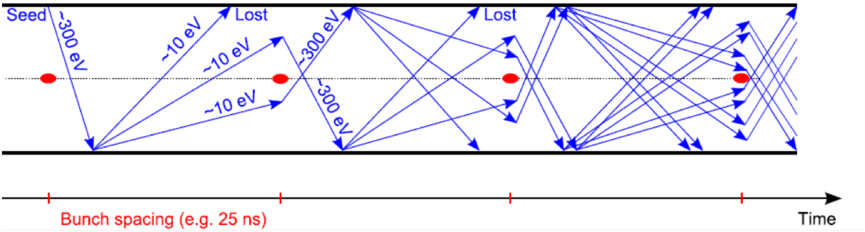

Figure 1.1.: Sketch of the electron cloud formation in a particle accelerator for the case of a bunch spacing of 25 ns [9]

1.1 The EC buildup mechanism

Figure 1.1 illustrates a qualitative picture of the EC build-up process at a certain location in the vacuum chamber of an accelerator ring. Each circulating bunch can generate primary electrons due to different mechanisms, e.g. ionization of residual gas in the beam chamber or photoemission from chamber's wall due to the synchrotron radiation from the relativistic beam. These are called "primary" or "seed electrons". Seeds are accelerated by the beam electric field to energies up to several hundreds of eV and travel inside the chamber.

When an electron with this energy impacts on the wall "secondary electrons" will be emitted, provided that the SEY of the chamber's surface is greater than unity at the impact energies. These secondaries are released into the chamber at low energies, e.g. few tens of eV. If secondary electrons impact with these energies, they are either absorbed or elastically reflected but cannot produce any secondaries. Instead, if they survive until the arrival of the next bunch, they can be accelerated and yield new secondary electrons which are added in turn to the existing electron population. In this way, the number of electrons in the vacuum chamber increases as more bunches go through, leading to the build-up of the EC.

The conditions needed for the formation of an EC depends on several parameters like bunch intensity, bunch spacing, transverse beam size, presence of externally applied magnetic fields and, of course, on chamber's surface properties.

1.1.1 Primary Electron sources

In this Section we will describe the two possible mechanisms of the electron production which are relevant for the CERN accelerators, namely the ionization of the residual gas and the photoemission due to the Synchrotron Radiation (SR).

Below a certain energy threshold, the main source of primary electron is the ionization of residual gas in the beam chamber. Due to the collision of fast beam particle with a neutral atom or molecule, a certain number of free electron-ion pairs can be produced. The ionization rate for a certain ion species is given by:

$$\frac{dn_{\text{ion}}}{dt} = \sigma_{\text{ion}} n_{\text{gas}} \phi_p \tag{1.1}$$

where σ_{ion} is the ionization cross section of the considered species [10], n_{gas} is the gas density (supposed to be uniform in space and constant on the time scale of few beam revolutions), and ϕ_p is the beam particle flux per unit area. The ionization cross section differs for the different gas species composing the residual gas and it scales with the square of the atomic number of the beam particle and of the gas atoms [11]. Slow incident particles provide a larger σ_{ion} [12].

In the case of the LHC top energy, due to the high SR, photoelectrons generated via photoemission are the dominant source of seeds. When relativistic charged particles travel along circular trajectories (e.g. in a bending magnet) they emit electromagnetic radiation in the direction tangent to the beam trajectory, known as synchrotron radiation. The amount of photons generated per unit time is related to the total power emitted by the beam (P) and to the critical energy of the radiation (E_{c}) [13]. These two quantities are given by:

$$P = \frac{q\gamma_{\text{rel}}^4}{3\varepsilon_0\rho} I_{\text{beam}} \tag{1.2}$$

$$E_{\text{c}} = 3\frac{\hbar\, c\gamma_{\text{rel}}^3}{2\rho} \tag{1.3}$$

where q is the particle charge, γ_{rel} is the relativistic factor corresponding to the beam energy, I_{beam} is the beam current and $\hbar$ is the reduced Planck constant.

Photons with energies larger than the work function of the beam chamber's can extract electrons from the surface via photoelectric effect [14]. These electrons are called *photoelectrons* and, for sufficiently large energy, they constitute the main mechanism of primary electrons production. The large amount of photons produced by SR are radiated within a very narrow cone characterized by an opening angle scaling with $\frac{1}{\gamma_{rel}}$. Only a faction of these photons are absorbed and therefore produce photoelectrons, at their first impact against the chamber's wall. The remaining photons are reflected by the metallic surface and can impact anywhere in the vacuum chamber. The relevant parameters to describe the surface are the photon reflectivity and the photoelectron yield of the beam chamber, i.e. the probability of electron emission per impinging photon. At the LHC, photoemission properties have been extensively studied with dedicated measurements in the laboratory. More details can be found in [15, 16].

1.1.2 Secondary Electron Emission

Primary emission mechanisms are often insufficient to lead a significant electron density within the beam chamber. The main contribution to the build-up of an EC will then come from the beam-induced multipacting. As shown in the simplified sketch in Fig. 1.1, primary electrons accelerated by the circulating proton bunches can produce new electrons when hitting the chamber surface. The capability of

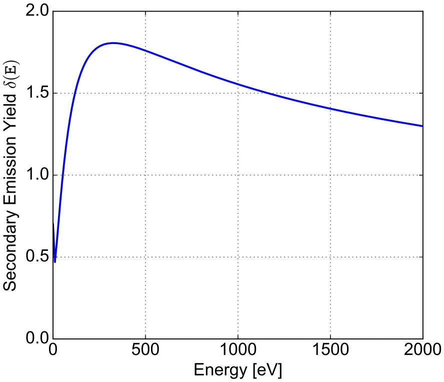

Figure 1.2.: SEY curve for δ_{max}=1.8.

a solid to emit secondaries is called SEY, indicated in the following with δ. It is defined as the ratio between the electron current impinging the chamber's walls and the corresponding emitted current:

$$\delta(E,\theta_{\text{i}}) = \frac{I_{\text{emit}}}{I_{\text{imp}}(E,\theta_{\text{i}})} \tag{1.4}$$

The SEY is a property of a surface material and it has a strong dependence on the energy at which primary electrons hit the chamber's wall (E), their angle of incidence (θ_{i}), the surface's material and its history. Typically, for materials employed for accelerator vacuum chambers, $\delta(E)$ has a peak (δ_{max}) ranging between 1 and 3 at an energy (E_{max}) between 200 and 400 eV. A typical SEY curve is presented in Fig. 1.2. Since the average impinging electron energy is typically few hundreds of eV [17], the secondary electron emission becomes significant in the build-up of an EC.

The model for the Secondary Electron Emission which has been used for all the calculations presented in this thesis relies mainly on laboratory measurements, which have been carried out on the copper surface of the LHC beam screen [18]. The SEY can be defined as sum of two components:

$$\delta(E,\theta_{\text{i}}) = \delta_{\text{elas}}(E) + \delta_{\text{true}}(E,\theta_{\text{i}}) \tag{1.5}$$

where $\delta_{\text{elas}}(E)$ and $\delta_{\text{true}}(E,\theta_{\text{i}})$ correspond respectively to electrons which are elastically reflected by the surface and to the so called "true secondaries". The former are low energy electrons which are reflected at the same energy they had before impacting. The function $\delta_{\text{elas}}(E)$ can be parametrized by:

$$\delta_{\text{elas}}(E) = R_0 \left(\frac{\sqrt{E} - \sqrt{E + E_0}}{\sqrt{E} + \sqrt{E + E_0}} \right)^2 \tag{1.6}$$

Based on experimental data, the two parameters R_0 and E_0 are set to 0.7 and 150 eV for a copper surface as the LHC beam screen. The true secondary component depends on the parameters δ_{max}, E_{max} and on the angle of impact of the electrons, θ_{i}, following the relations:

$$\delta_{\text{true}}(E, \theta_{\text{i}}) = \delta_{\text{max}}(\theta_{\text{i}}) \frac{s \dfrac{E}{E_{\text{max}}(\theta_{\text{i}})}}{s - 1 + \left(\dfrac{E}{E_{\text{max}}(\theta_{\text{i}})} \right)^s} \tag{1.7}$$

$$\delta_{\text{max}}(\theta_{\text{i}}) = \delta_{\text{max}}(\theta = 0)\, e^{\dfrac{1 - \cos(\theta_{\text{i}})}{2}} \tag{1.8}$$

$$E_{\text{max}}(\theta_{\text{i}}) = E_{\text{max}}(\theta = 0)(0.3 + 0.7 \cos(\theta_{\text{i}})) \tag{1.9}$$

where, for the LHC chambers, we use the values $s = 1.35$.

Higher angles of incidence significantly increase the emission of secondary electrons. This dependence is motivated by the fact that electrons impacting with a large angle of incidence spend more time close to the surface. Therefore their chance of producing secondaries in enhanced. In the PyECLOUD code true secondaries are emitted with a cosine angular distribution with respect to the direction normal to the surface and their energy spectrum is well fitted by a log-normal distribution. See [9] for more details.

1.1.3 Electron cloud build-up regimes

A convenient phenomenological parameter for describing the EC build process is the effective SEY, δ_{eff} [19]. This quantity can be directly related to the SEY of the chamber's surface $\delta(E)$ and to the the energy spectrum of the impinging electrons ϕ_E. The analytical derivation of the following equation can be found in [9]:

$$\delta_{eff} = 1 + \int_0^\infty \phi_E(\delta(E) - 1) \mathrm{d}E \tag{1.10}$$

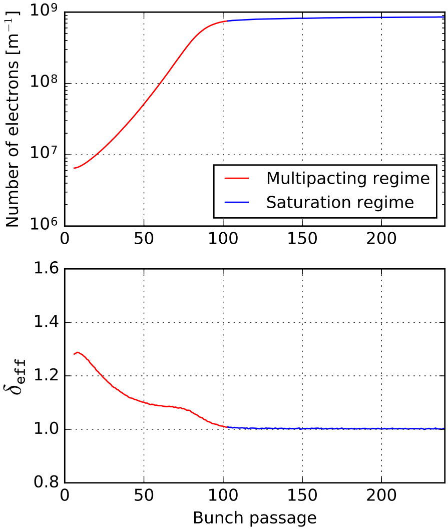

Figure 1.3.: EC buildup simulations for $\delta_{max} = 1.4$. Simulated case: SPS MBB bending magnet, 26 GeV, single train of 200 bunches, 25 ns bunch spacing. Top: number of electrons before each bunch passage. Bottom: Evolution of δ_{eff}. The multipacting and the saturation regime are plotted in red and blue, respectively.

The SEY curve can be divided in two regions, one in which $\delta(E) < 1$ (the surface acts as an electron absorber) and the other in which $\delta(E) > 1$ (the surface acts as an electron emitter). Looking at the Eq.1.10, we can infer that whether δ_{eff} is below or above unity depends on whether the energy spectrum overlaps more with the absorber or the emitter region of the SEY curve.

When δ_{eff} is lower than one, the chamber wall acts as a net absorber. In this situation an equilibrium is reached when the number of produced seeds balances the number of electrons absorbed by the surface. On the contrary, if δ_{eff} is larger than one the electron density increases exponentially becoming orders of magnitude larger than the primary electron production rate. This multipacting process is responsible for the electron cloud buildup in several machines. The growth slows down as the EC space charge repulsion becomes strong enough to prevent newly emitted electrons from freely moving inside the chamber. In this phase, the net electron production and loss rates become equal and a dynamical equilibrium is reached. This regime is called *saturation* and it is characterized by $\delta_{eff} = 1$.

The transition to the saturation regime can be observed in Fig.1.3. It shows the simulated EC buildup in the LHC type chamber assuming a uniform train of 25 ns spaced bunches. The simulation has been performed with the PyECLOUD code (described in Sec.1.3.1). In these plots we can recognize two different stages, one going from the first passage up to around the 100th, and the second from that point onward. In the first stage the number of electrons grows exponentially in the beam pipe and the EC builds up. This regime is characterized by $\delta_{eff} > 1$. Later on, we observe that the number of electrons deviates from the exponential growth and saturates to a constant value. By looking at the δ_{eff} evolution we can notice that at this point δ_{eff} is equal 1. This means that the increased space charge forces counteract the production mechanism and the EC reaches an equilibrium.

Electrons exhibit different transverse distribution in the beam chamber depending on the applied magnetic field. In the field free regions (e.g. drift sections) they tend to spread across the pipe section, whereas in the presence of externally applied magnetic field the cloud develops with a characteristic pattern. This can be understood considering the fact that the electrons are non relativistic ($v_e \ll c$). As consequence, in the presence of an external magnetic field, they are forced to move around the field lines following helicoidal trajectories [20]. The cyclotron radius of the helix (also called Larmor radius) depends on the magnetic field and on the orthogonal component of the electron velocity to the field lines.

An example of characteristic pattern of the electron density in different type of LHC magnets is shown in Fig.1.4. In the case of the bending magnet electrons can only move in the vertical (y) direction and they are essentially frozen in the horizontal (x) one. Electrons trapped by different field lines will receive a different y-kick from the beam which is x-dependent. For this reason, a different efficiency of the multipacting process takes place resulting in the characteristic high density vertical stripes. The position of these side stripes mainly depends on the beam intensity and on the position of the E_{max} on the SEY curve. Similar effects can be observed also in the quadrupole magnets. Here, the EC develops along the pole-to-pole magnetic field line assuming an x-like shape. The presence of the magnetic field gradient triggers a trapping effect which increases the electron density at the beam position [21]. Differently from the dipole case, trapped electrons can survive longer in the beam chamber making the EC buildup more severe.

1.1.4 Mitigation techniques

Over the years, different strategies have been studied and adopted in several particle accelerators in order to mitigate, or ideally suppress, the EC. They can be distinguished in active and passive [22].

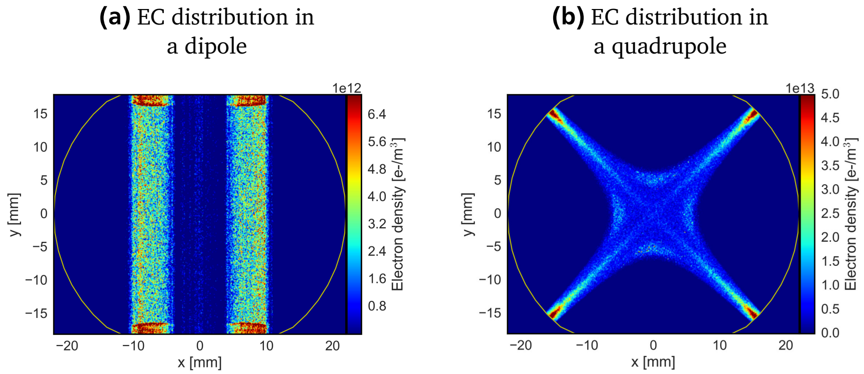
(a) EC distribution in a dipole

(b) EC distribution in a quadrupole

Figure 1.4.: Snapshots of the EC density in a dipole (a) and quadrupole (b) magnet of the LHC

Active metods rely on an externally applied electric/magnetic field to control the electron density around the beam. The most common are clearing electrodes [23] and weak solenoid fields (about 10-20 G) [24]. The former allows reducing the electron density by absorbing electrons through a static electric field, while the latter allows deflecting the emitted photoelectrons back to the wall, mitigating the subsequent beam-electron interaction.

Passive strategies instead act directly on the surface properties either through geometrical modifications of the pipe surface or by reducing its SEY. An example of surface modification is machining the wall surface to produce macroscopic grooves on it. These grooves essentially act as electron traps, as the electrons emitted by the surface are re-absorbed before being accelerated in the beam field. Much optimization work has been done to define the shape and the size of the grooves in order to obtain the best electron cloud suppression [25].

A well established method to reduce the SEY of the chamber' surface is the coating with low SEY materials like the amorphous-Carbon (a-C). This coating has been widely tested at the SPS where the suppression of the electron cloud was successfully proven in dedicated strip monitors [26].

A valid alternative to the coating is the scrubbing or "SEY conditioning". It consists in a chemical modification of a technical surface by means of a prolonged electron irradiation. It has been proved in the laboratory that the electron bombardament tends to decrease the SEY, especially when using relatively high energy electrons [28]. Figure 1.5 shows an example of SEY curves measured on the colaminated Cu of the LHC beam screen as-received and after the bombardament with

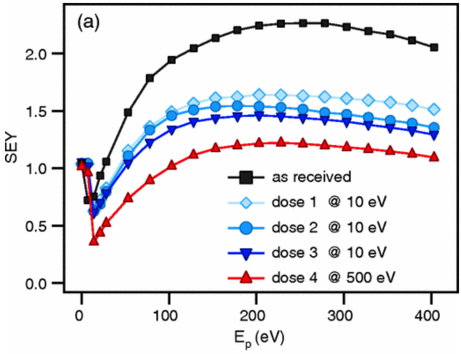

Figure 1.5.: SEY curves measured on the colaminated Cu of the LHC beam screen as a function of the electron and impinging energies (dose1: Q=$3.2 \cdot 10^{-3}$ C/mm^2, dose2: Q=$4.8 \cdot 10^{-3}$ C/mm^2, dose3: Q=$1.1 \cdot 10^{-2}$ C/mm^2, dose4: Q=$1.2 \cdot 10^{-3}$ C/mm^2) [27].

different electron doses and impinging energies [27]. A clear global reduction of the SEY curve is observed when increasing the electron dose and the energy.

The presence of a large density of electrons in the beam pipe can therefore be used to bombard the chamber's wall in order to reduce the SEY of the surface and thus, in turn, the total amount of electrons. This self-mitigation mechanism is commonly referred as "beam induced scrubbing". However, the scrubbing process is quite different from that obtained in the laboratory. Indeed, the beam induced scrubbing becomes much slower while it progresses, due to the decrease of the electron flux as the SEY decreases, and is localized according to the EC distribution pattern in the vacuum chamber. Nevertheless, beneficial effects of the beam scrubbing on the accelerator conditions (e.g. pressure rise, heat load) and beam quality have been observed over the years in most of the CERN rings. Figure 1.6 shows an example of heat load measured on the LHC beam screen during the intensity ramp up with 25 ns beams in 2015. Thanks to the accumulated scrubbing dose, an evident conditioning of the machine has been observed.

1.2 Impact of EC effects on the accelerator's performances

The presence of the EC in the beam pipes can limit the achievable performances of a particle accelerator through detrimental effects that affect both the beam properties and the machine operation.

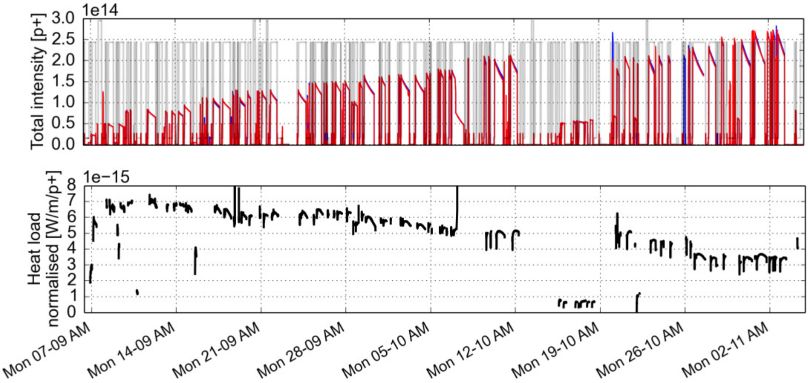

Figure 1.6.: Evolution of the beam intensity (top and heat load normalized to the beam intensity (bottom) measured in the LHC during the intensity ramp up with 25 ns beams in 2015 [29].

As described in [30], when a proton bunch passes through an EC, electrons traveling in the beam chamber will gain some energy due to the passage of the bunch itself. According to the their position two regimes can be defined. If an electron is initially located beyond a certain critical radius (e.g. photoelectrons first produced), it receives a kick (transverse change momentum) from the bunch which only depends on its radial position in the beam pipe. In this case, the electron is essentially stationary during the bunch passage. This is called "kick regime". On the contrary, if an electron lies closer to the beam core, i.e. below the critical radius, it is in the "autonomous regime". This means that it gets temporarily trapped in the bunch potential and will perform non linear oscillations around the bunch itself. This process results into an increased electron density seen by particles along the bunch, the so called "electron pinch". Figure 1.7 shows the pinch development in a dipole magnet during the passage of an LHC-type bunch. This simulation has been performed using the PyECLOUD-PyHEADTAIL tool (see Sec. 1.3.3). The two-dimensional color plot displays the evolution of the electron density on the vertical axis as a function of the longitudinal position z along the bunch. It is evident that several electron pinches take place especially in the tail part of the bunch.

This distortion of the electron distribution is the mechanism that couples the head and the tail motion of a single bunch coherent. Whether the bunch is perfectly centered on the pipe axis, the pinch also happens symmetrically and no coherent kick is generated along the bunch. On the contrary, if the head of the bunch enters the EC with a slight offset, an asymmetric pinch will take place resulting into a net

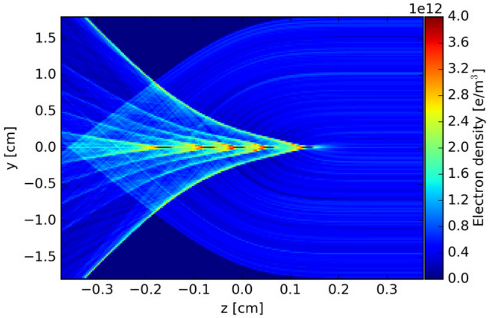

Figure 1.7.: Electron density evolution during the passage of a LHC-type bunch in a dipole magnetic field, obtained from a PyECLOUD-PyHEADTAIL simulation as a function of the longitudinal position. The head of the bunch is at z=0.35

kick felt by the bunch tail. After several passages through the EC, this intra-bunch dynamics can give rise to coherent instabilities and emittance growth [31, 32].

However, even when the beam remains transversely stable, its interaction with the EC can be source of incoherent effects which slowly degrade the beam quality [33, 34]. These effects are particularly worrying in storage rings and colliders where the aim is to store the beam in the ring for a very long time while preserving the beam quality.

Besides these beam observables, the EC can be also responsible for local detrimental effects such as pressure rise and degradation of the beam diagnostic equipment. Of particular relevance is the additional heat load that the impinging electrons can deposit on the chamber's wall. While this effect is typically negligible in room temperature accelerator component, it can become a serious issue in devices operating at cryogenic temperature, for which only a limited cooling capacity is available (e.g. LHC superconducting magnets) [35].

1.3 Physics simulation codes

The understanding of EC related effects heavily relies on numerical simulations. The main features of the Python toolkit [36] used to carry out the studies presented in this work are described in the following sections.

1.3.1 The PyECLOUD code

The PyECLOUD code was developed at CERN in order to study the formation of the electron cloud in accelerator structures [9]. It is based on the physics model used in ECLOUD [37] but owing to the implementation of new optimized algorithms, it exhibits a significantly improved performance in terms of accuracy, speed and flexibility.

PyECLOUD is a 2D code where the electrons are grouped in Macroparticle (MP) to allow both a satisfactory description of the phenomena and a reasonable computational burden. In the classical EC build-up simulation mode, the beam distribution is assigned *a priori* and it is not affected by the Columbian forces of electrons ("rigid beam" approximation). At each time step primary electrons are generated by the circulating bunch due to ionization of the residual gases and/or photoemission driven by synchrotron radiation. Seed electrons are created with position and momenta according to theoretical or empirical models described in Sec 1.1.1. The possibility to assume an initial electron density uniformly distributed within the beam chamber is also available.

The forces acting on each MP are evaluated as sum of the electric field generated by the beam and the space charge forces within the EC. Under the rigid beam approximation, the electric field of the beam can be precomputed on a suitable rectangular grid, stored and, then, obtained at each MP location by a interpolation. The space charge contribution of electrons themselves is instead computed using the Particle In Cell (PIC) algorithm. In both cases, the field calculation is mainly performed with the Finite Difference (FD) method which is more suited to model arbitrarily shaped chambers. This solver is included in a stand-alone general library called PyPIC (see Sec. 1.3.2).

Once the total electric field at each MP location is known, MPs positions and momenta are updated by integrating the equations of motion taking into account also the presence of an externally applied magnetic field. The last stage of the simulation flow is the detection of impacts and the generation of secondary electrons. The latter is based on the experimental model of the secondary electron emission described in Sec. 1.1.2. An important feature of this kind of simulations is that the MP size needs to be dynamically adapted during the simulation due to the fact the number of electrons grows exponentially throughout the buildup process. Figure 1.8 shows a typical picture of the simulated EC buildup for two trains of 72 bunches assuming different δ_{max}. The main input parameters of this simulation are listed in Table 2.1. As stated in Sec. 1.1.3, during the passage of the first 72 bunches the number of electrons within the beam pipe grows exponentially until it reaches the saturation. In correspondence of the gap between the two trains a decay of the number of electrons is observed. It is clearly evident that the EC buildup becomes more severe for increasing δ_{max}.

1.3.2 The PyPIC code

A simple PIC solver was originally contained in PyECLOUD. However due to the need of including new features and making it avalaible also to other applications, it was decided to provide it as a separate Python library called PyPIC. This library contains different Poisson solvers based both on the Fast Fourier Transform (FFT) methods and on the FD methods. As the PIC solution needs to be performed at each simulation time step, a significant effort was put into the performance optimization of this component [38].

EC buildup simulations are manily performed with FD solvers which are able to better handle curved boundaries using the Shortley-Weller method [39]. An important feature of this kind of simulations is that the required PIC resolution is not uniform over the simulation domain. In fact a strong gradient in the charge distribution is observed at the beam location (EC pinch effect) while the distribution is much smoother elsewhere. For this reason, a new solver has been recently implemented which allows employing nested grids with different resolution to refine the PIC accuracy only were needed. This solver was developed following the approach described in [40] and it showed a significant improvement in terms of the simulation speed [41].

Thanks to the support of this new feature, more complex scenarios can be simulated like LHC instabilities at top energy and where the beam size is extremely small with respect to the chamber, which were previously inaccessible.

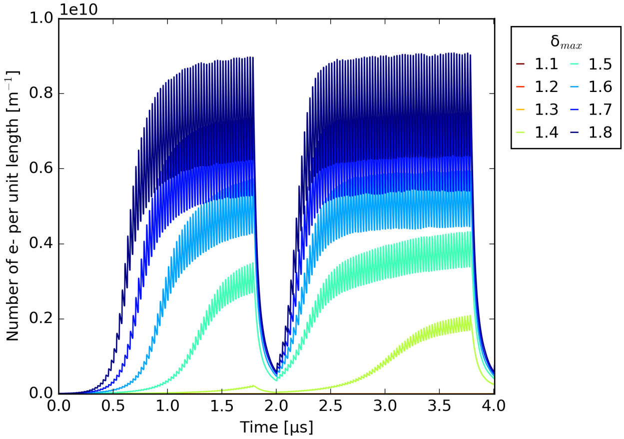

Figure 1.8.: Simulated buildup of an EC using PyECLOUD for different δ_{max}. Simulated case: SPS MBB bending magnet, two trains of 72 bunches with 225 ns gap. The parameters used in simulations can be found in Table 2.1

Parameters	Symbol	Value
Beam energy [GeV]	E	26
Bunch population [ppb]	N_b	$2.5{\cdot}10^{11}$
Bunch spacing [ns]	s_b	25
Rms. beam size [μm]	$\sigma_{x,y}$	2.5
Rms. bunch length [m]	σ_z	0.25
Average beta function [m]	$\beta_{x,y}$	45.50,78.40
Peak dipole field [T]	B	0.12

Table 1.1.: Input parameters for the simulations shown in Fig.1.8. Simulated case: SPS MBB bending magnet, two trains of 72 bunches with 225 ns gap.

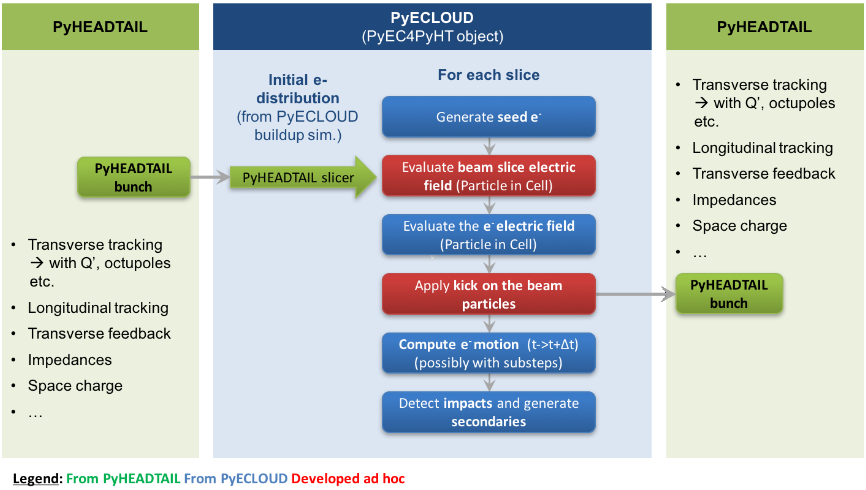

Figure 1.9.: A graphical illustration of how PyHEADTAIL interacts with PyECLOUD [42]

1.3.3 The PyECLOUD-PyHEADTAIL setup for beam dynamics simulations

To simulate the beam behavior in the presence of an EC we use a newly developed interface that combines PyECLOUD with the PyHEADTAIL beam dynamics code [42]. This integration, which was possible thanks to the modular structure and flexible nature of both codes, allows to drop the traditional approach of having separate tools for the EC buildup and beam dynamics simulations with several advantages. Indeed all the advanced features implemented in PyECLOUD and PyPIC become naturally available also for the beam dynamics simulations in presence of EC.

A graphical illustration of how the different parts of the codes interact with each other is shown in Fig. 1.9. In PyHEADTAL the accelerator is modeled as a list of Python objects arranged in a ring structure which performs different actions on the beam such as longitudinal and transverse tracking, wake fields, feedbacks and space charge. PyECLOUD allows to define electron cloud objects which are lumped in the PyHEADTAIL ring at selected interaction. In each of these interaction points, the state of the bunch macroparticles is passed to PyECLOUD. At this point, the bunch is sliced and the particles contained in each slice successively interact with the electrons. Their dynamics is computed as for the buildup simulation but with two notable differences. The first one is that since the beam is no longer considered rigid, its beam field has to be calculated at each simulation time step. The algorithm used for this computation is the PIC solver form the PyPIC library. The other one is that the electric forces from the EC are not only applied to the electron MPs but also to the beam MPs. The updated beam phase space coordinates are subsequently passed back to PyHEADTAIL to continue tracking.

This setup offers significant improvements to the modeling of EC induced beam dynamics. An obstacle that prevented from benefiting fully from the capabilities of this new approach was the impractically long run-times required, e.g. for studying coherent effects at the LHC at collision energy. In this case, even profiting from the the speedup from the PyPIC nested grids, the time requirements to approach the machine observations (instability rise time of the order of 10^4 turns) were still prohibitive (several weeks). To tackle these cases and boost the computing speed, parallel computing resources have been exploited. The parallelization was realized through an additional Python layer, called PyPARIS, which is independent from PyECLOUD and PyHEADTAIL. This allows keeping as separated ad possibile the physics and the parallelization code. More information on the implementation can be found in [36] and references therein. This simulation mode has been extensively used to study the LHC electron cloud driven instabilities discussed in Chap. 3.

2 Electron cloud buildup studies in the CERN particle accelerators

Particle accelerators are important instruments to explore a wide range of processes related to the high energy physics, material science, molecular biology and medical applications. CERN operates the largest particle physics laboratory in the world with the aim of testing different theories in high energy physics and probing the fundamental structure of the matter.

Figure 2.1 shows a schematic of the CERN accelerators complex which is a succession of machines that accelerate beams of protons and/or lead ions to increasingly higher energies. In the present work, we will focus only on the proton accelerator chain. Protons are produced by a duoplasmatron source and accelerated up to 50 MeV kinetic energy in the LINear ACcelerator 2 (LINAC2) before being injected into the Proton Synchrotron Booster (PSB). In the four superimposed rings of which the PSB is made, protons are accelerated up to 1.4 GeV and transferred to the Proton Synchrotron (PS), which is the oldest machine of the accelerators complex. The PS plays a central role in the preparation of the LHC nominal beam. In fact, it is responsible for producing the required 25 ns bunch spacing through a series of Radio Frequency (RF) manipulations [43]. Then the LHC-type beam is extracted at a momentum of 26 GeV/c and stored in the SPS ring. Here the beam is accelerated up to 450 GeV and sent to the LHC, where the beam is further accelerated and collisions take place when the maximum beam energy is reached as explained in the next section.

In the present chapter, we discuss the performance limitations caused by the EC buildup both in the LHC and in the SPS ring.

2.1 The Large Hadron Collider

The LHC is the world's largest and most powerful particle accelerator hosted in a 27 km underground tunnel, on average 100 m deep, across the Franco-Swiss border. It aims at colliding two counting rotating beams in order to investigate the properties of the Higgs boson (discovered in 2012), consolidate the validity of the super-symmetric theories and answer other open questions about high energy physics.

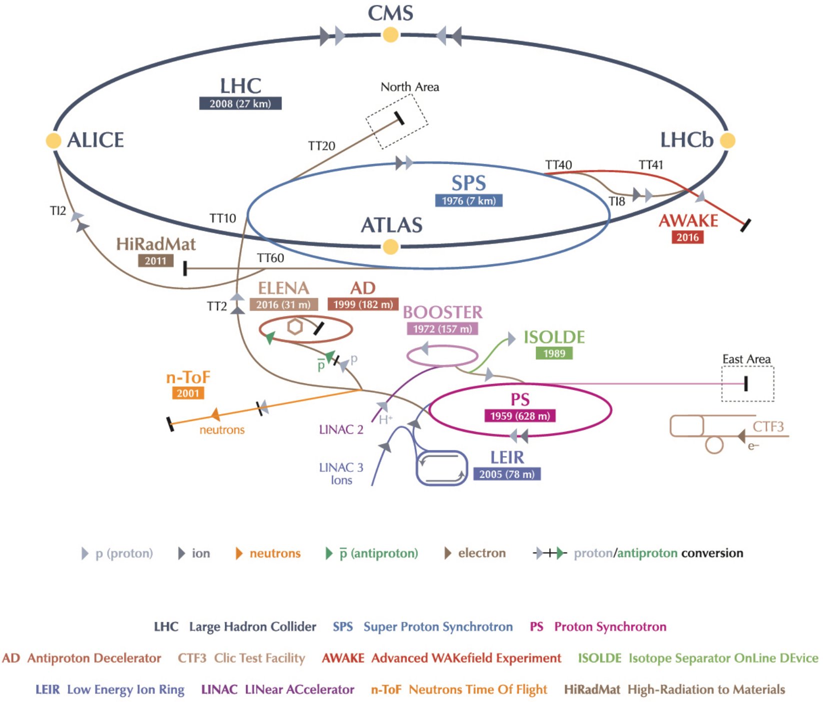

Figure 2.1.: The CERN accelerator complex. Courtesy of CERN®

The properties of particles emerging from the collision are collected and analyzed by four particle detectors placed along the accelerator ring, each having different properties. More precisely, A Toroidal LHC ApparatuS (ATLAS) and Compact Muon Solenoid (CMS), which are the two large general-purpose experiments, look for rare events like the long-awaited Higgs particle, whereas, A Large Ion Collider Experiment (ALICE) studies the quark–gluon plasma from heavy ion (Pb-Pb nuclei) collisions, that existed shortly after the Big Bang, and Large Hadron Collider Beauty (LHCb) the matter-antimatter asymmetry of the Universe.

Even thought the beams circulated for the first time in 2008, the LHC physics program started officially in March 2010 with colliding proton beams at an energy of 3.5 TeV per beam. Figure 2.2 shows the LHC timeline from 2011 to 2020. It operated at 3.5 TeV per beam until 2012, when it was decided to raise up the energy to 4 TeV per beam. The combined analysis of events recorded in 2011 and

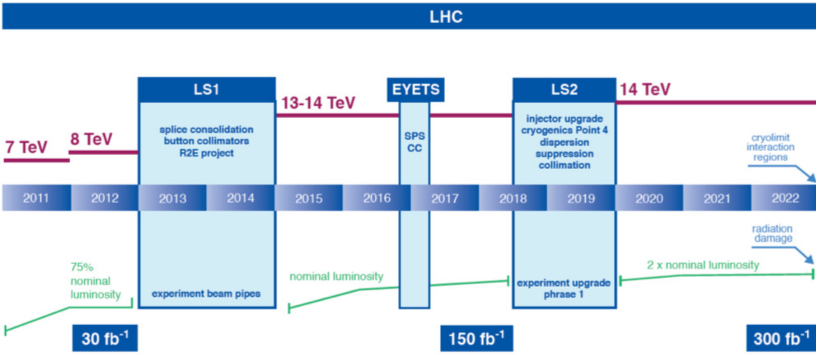

Figure 2.2.: The schedule of the LHC operation until 2022.

2012 led to the Nobel-prize winning discovery of the Higgs boson, as announced by the two main experiments ATLAS and CMS.

After a long consolidation campaign of two years, i.e. the Long Shutdown 1 (LS1), the beam operation restarted on April 2015, planning for a 4-year long run called Run 2. Thanks to the consolidation and maintenance activities performed during the shutdown, the LHC could operate at an energy of 6.5 TeV per beam, the highest ever reached in an accelerator, and with beams having the designed bunch spacing of 25 ns (i.e. in 2011 and 2012 LHC ran with 50 ns). Due to several challeges (e.g. EC formation, fast losses) that had to be faced, 2015 has been considered a year of commissioning and learning, dedicated to prepare a solid base for physics production in the rest of Run 2 [44].

The quantity that measures the ability of a collider to produce the required number of particle collisions is called Luminosity, $\mathcal{L}$ [45]. For Gaussian particle distributions colliding without any transverse offset can be written as:

$$\mathcal{L} = \frac{N_1 N_2 n_b f_{rev}}{2\pi\sigma_x\sigma_y}\mathcal{H}\mathcal{F}_g \tag{2.1}$$

where N_1, N_2 is the number of particles per bunch, n_b is the number of bunches, f_{rev} is the revolution frequency (11.2 kHz in the LHC), σ_x and σ_y are the rms horizontal and vertical beam size at the collision points. $\mathcal{H}$ and $\mathcal{F}_g$ are the hourglass effect and the geometrical reduction factor due to the crossing angle, respectively. The higher the luminosity the more data the experiments can gather to allow for the measurements of rare processes.

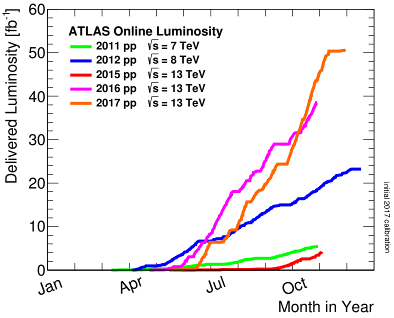

Figure 2.3.: Overview of the integrated luminosity delivered to ATLAS for 2011-2017. Courtesy of ATLAS experiment.

Figure 2.3 shows the integrated luminosity (i.e. the inverse femtobarn fb^{-1} is the unit used to measure the cumulative number of events over a given period) delivered to ATLAS for 2011-2017. It can be observed that the luminosity has been constantly increasing during the current Run 2 (i.e. apart from 2015 which is considered a year of commissioning). In particular the 2017 line, which exhibits the fastest accumulation of all the years, reveals that the LHC had outperformed its production target for the year (i.e. 45 fb^{-1}), delivering more collisions than expected to the experiments.

In order to push its luminosity even further from 2025, LHC will go through its major upgrade program under the High Luminosity LHC (HL-LHC) project [46]. This will increase the chances to observe rare processes, improve statistically marginal measurements and in general extend the LHC discovery potential. The objective of this project is to reach an instantaneous luminosity by a factor five beyond the design value and an integrated luminosity of 250-300 fb^{-1} per year. Thus the novel machine configuration will rely on innovative technologies which represent significant technological challenges. The HL-LHC upgrade requires also substantial changes in the full chain of the LHC injectors to reach the foreseen beam characteristics in terms of intensity and brightness. This massive upgrade and renovation is pursued under the LHC Injectors Upgrade (LIU) project [47].

2.1.1 Machine layout and configuration

A detailed description of the main features and subsystem of the LHC can be found in [48]. In the following we will briefly recall those more relevant for the present thesis work.

The LHC ring is composed by eight Long Straight Section (LSS) linked by eight arcs. Each LSS serves a different purpose, as pictured in Fig. 2.4. Four of these sections host the main experimental detectors, as described in the previous section. In these areas, the beams share a common beam pipe (approximately 130 m long). The remaining four LSS, which do not have beam crossing, are used for the RF cavities, the beam cleaning systems and the beam dump systems.

In the LHC lattice, the straight sections are interspaced with circular arcs. They are made by 23 classical FODO cell [49], 106 m long. Each half-cell consists of three bending dipole magnets 14.3 m long (Main Bend (MB)) and one 3.1 m long quadrupole magnet (Main Quadrupole (MQ)). These main magnets are interleaved by corrector magnets in different configurations used to cancel their field distortions, correct chromatic effects and introducing amplitude detuning (e.g sextupoles, octupoles and other higher order magnets [50]). The MBs, which fill about 65% of the LHC circumference, are used to bend the paths of the particles along the ring. The MQ magnets instead cover a smaller fraction of the machine circumference, about 7%. They have the purpose to keep the protons focused horizontally and vertically. The ones that focus in the horizontal plane are called Quadrupole Focusing (QF) and the ones that focuses in the vertical plane are called Quadrupole Defocusing (QD). In order to explore higher beam energy ranges, most of these magnets are kept in a superconductive state operating in super-fluid helium at 1.9 K and provide a nominal gradient of 175 T/m at 6.5 TeV.

In the LHC, the circulating beam is not uniformly distributed along the ring but organized in a set of bunches. From the SPS, the bunches are injected into the LHC in several trains separated by gaps of 925 ns in order to allow for the LHC injection kicker rise time. Each train is composed by two or four batches, i.e. group of 72 bunches spaced by 25 ns. Between the batches there are gaps of 225 ns, which account the rise time of the SPS injection kicker. An abort gap of at least 3 μs is also present at the tail of the full beam in order to enable a safe extraction towards the beam dump. The beam produced following this scheme is referred as standard beam. For this configuration, the main beam and machine parameters are reported in Table 2.1. However there is a large flexibility concerning the choice of the filling scheme. Indeed, over the years, several bunch patterns have been tested in order to optimize the machine performance, as for example the so-called Batch Compression Merging and Splitting (BCMS) scheme, i.e. the high brightness variant of the 25 ns beam, and "8b+4e" scheme, i.e. eigth bunches with 25 ns spacing separeted by four empty slots (with 30% less bunches compared to the nominal scheme). Due to its micro-bunch structure, "8b+4e" significantly reduces the EC formation. More details on the available operational beams can be found in [51].

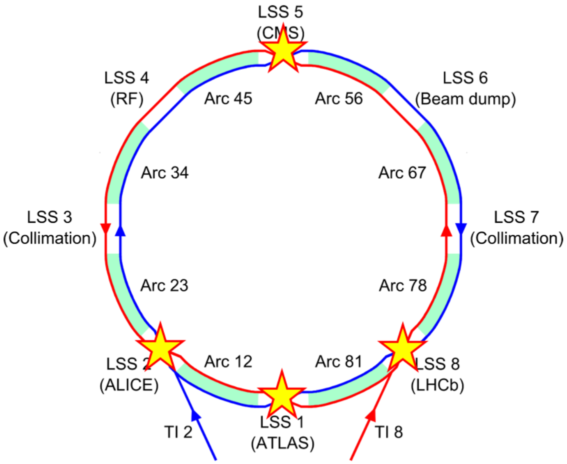

Figure 2.4.: Schematic layout of the LHC. Two beams circulate in opposite directions around the ring crossing at the designated Intersection Points (marked with a star). Each of the eight straight sections hosts either an experiment or different elements necessary for the correct operation of a particle accelerator

Parameters	Injection	Collision
Proton momentum [GeV/c]	450	6500
Bunch spacing [ns]	25	25
Bunch intensity [10^{11} proton/bunch]	1.3	1.25
Max colliding bunches	2820	2556
Bunch length [ns]	1.25	1.05
Norm transverse emittance [μm]	2.6	2.5
Peak Luminosity in IP5/6 [10^{34} cm^2 s^1]		1.5
β^* in IP1/5 [m]		0.4
Horizontal tune	62.270	62.310
Vertical tune	60.259	60.320
Revolution frequency [kHz]	11.245	
RF frequency [MHz]	400.8	

Table 2.1.: Main LHC machine and proton beam parameters

2.2 EC buildup and heat loads in the LHC arc beam screens

The experience with 25 ns beams has shown that EC effects could pose important challenges to the operation of the LHC. Indeed, starting from the 2015 proton run, a strong dynamic heat load due to the EC has been observed in the cold sections of the LHC [29]. While this effect is typically negligible in room temperature accelerator components, it can become a potential threat to the cryogenic components of the LHC superconducting magnets, like the dipole and quadrupole magnets of the cryogenics arcs.

Inside the 1.9 K cold bore of the superconducting magnets, the thermal loads caused by the circulating beam are intercepted by a perforeted beam screen, held at an intermediate temperature of 5-20 K, for which only a limited cooling capacity is available for the heat load induced by the EC. This can result in a limitation of the maximum beam intensity that can be stored and, therefore, on the luminosity. Therefore, a great effort has been put to study the EC formation in the main cryogenic arc components and its dependence on different beam parameters combining both numerical simulations and experimental studies [9, 52].

2.2.1 The LHC beam screen

The LHC beam screen (see Fig. 2.5-left) is made by a 1 mm thick non-magnetic stainless steel tube with a 75 um thin layer of copper coating on its inner surface which minimizes the wall resistivity. In order to limit the dynamic pressure rise, the beam screen contains pumping slots over few percents of its surface to allow cryo-pumping by the 1.9 K cold mass. The width of these slots in the LHC arcs is 1.5 mm [53]. The drawback of this configuration is that multipacting electrons could penetrate through the slots inducing a significant heat load onto the cold bore. For this reason baffle plates, i.e. shields installed 2 mm behind the pumping slots, were added on the outer side of the beam screens, such that the electrons are intercepted before reaching the cold bore of the dipole magnets, at the expense of a pumping speed which is reduced by a factor of two [54].

Presently new superconducting magnets for the LHC insertion regions as well as beam screens are being designed for the HL-LHC project. The question has been raised whether the electric shielding provided by the beam screen could be sufficient to prevent multipacting, even in the absence of baffle plates. This question has been addressed with detailed simulation studies using the PyECLOUD code. In the following subsections, we describe the implemented simulation model and summarize the outcome of the study.

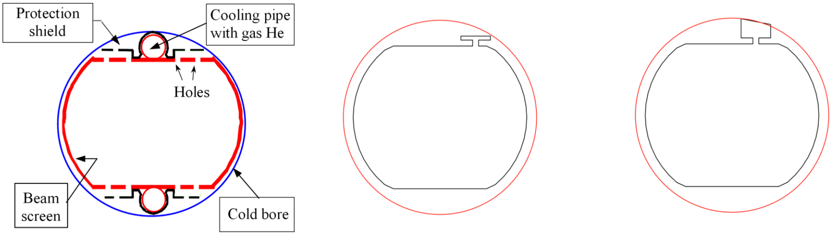

Figure 2.5.: Left: Cross section of the LHC beam pipe with beam screen and shield protections (taken from [55]). Center: Chamber shape used to model the beam screen with the shielding baffle plate. Right: Chamber shape used to model the beam screen without the shielding baffle plate.

2.2.2 PyECLOUD simulation setup and code upgrades

To study the effect of the baffle plates on the EC buildup we have considered the case of an LHC arc dipole. The effect of a single pumping hole has been studied modeling the hole and corresponding baffle by adding a T-shaped boundary as shown in Fig. 2.5-center. The situation with no baffle installed has been modeled as shown in Fig. 2.5-right. The width of the added part has been chosen such as not to perturb the field and the dynamics of the electrons. This kind of chamber geometry could not be simulated with the existing PyECLOUD code since some of the employed algorithms were assuming a convex boundary. Therefore, the following modifications had to be introduced in order to allow the EC buildup simulation with the required geometry.

In PyECLOUD the electrons, which are modeled with MPs, are tracked under the effect of the externally applied magnetic field and the electric fields of the proton beams and the electrons themselves. The code detects electron impacts on the beam screen by identifying particles that drift outside the chamber domain, as described in [9]. To check whether a given point is external or internal to the chamber, the algorithm previously used was assuming a convex polygonal boundary. In order to deal also with non-convex shapes, we added to the exiting routine a more general algorithm based on a ray-casting method (also called even-odd method). The even-odd method counts the number of times that an arbitrary ray, starting from a given electron position and going to a fixed direction (i.e. we assume a ray shooting in the positive x-direction), intersects the edges of the chamber. It can be proved [56] that, if the number of intersections is even, the point lies outside the chamber, otherwise the point is inside.

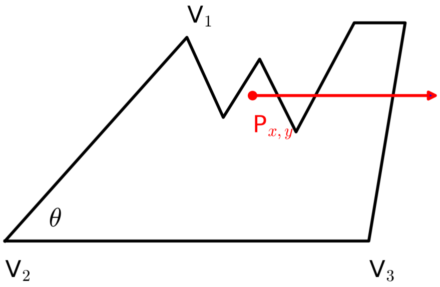

Figure 2.6.: Example of non-convex geometry. The red line shows the horizontal ray starting from a given point point P and shooting in the positive x-direction.

In PyECLOUD, the impact point on the chamber is found by intersecting the MP trajectory with the boundary. However in the case of non-convex shape, multiple crossing points can be found. For this reason, a loop for searching the physical impact point ("first impact") also needed to be implemented.

2.2.3 Simulation results

The simulations have been performed for the LHC injection energy (450 GeV), corresponding to a field in the main dipoles of 0.53 T. The LHC operational beam parameters have been assumed, i.e.$1.25 \cdot 10^{11}$ Proton Per Bunch (ppb) with transverse r.m.s. emittances of 2.5 μm, and the maximum of the SEY curve scanned between 1.0 and 2.0.

Figure 2.7a shows the distribution in the transverse plane of the electric field generated by the circulating proton beam. We can observe that the beam field is very low in the region between the screen and the baffle, meaning that electrons in this region can hardly be accelerated by the beam. However, from the snapshot in 2.7b, we can notice that the electron density can reach a quite high value around the baffle region already before the bunch passage. The electric field generated by this distribution is displayed in Figs. 2.7c and 2.7d. This non-negligible amount of electrons in the region of the hole suggests that multipacting on the baffle plate is nevertheless taking place. The reason is that a large fraction of the electrons from the baffle drifts inside the beam screen even before the following bunch passage. In fact, due to the strong magnetic field of the dipole, the electrons are constrained to follow helicoidal trajectories around the field lines. In Fig. 2.8, we show the dependence of the electron cyclotron radius on the kinetic energy associated to the motion in the plane orthogonal to the magnetic field. The energy of the secondary

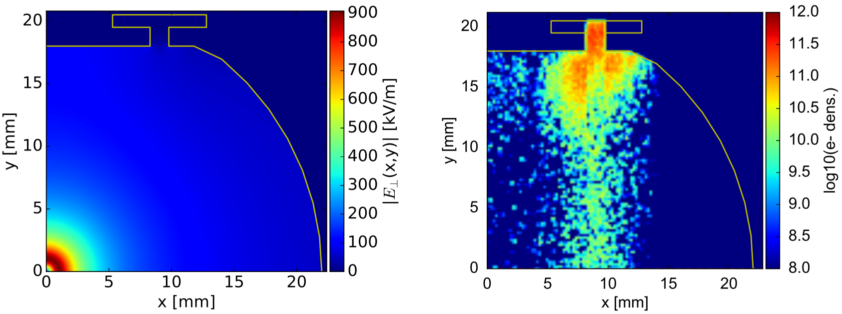

(a) Beam electric field

(b) EC distribution

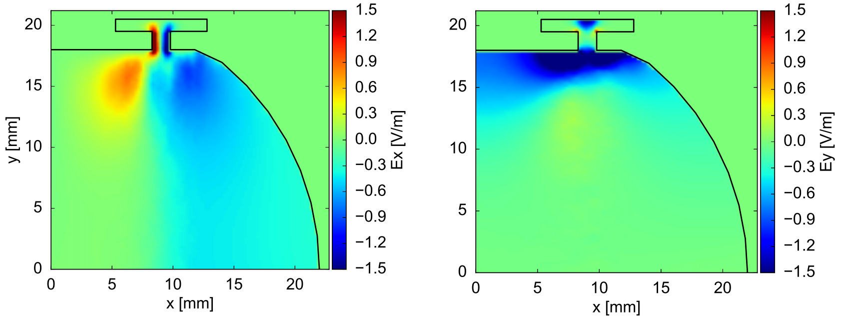

(c) Horizontal EC electric field

(d) Vertical EC electric field

Figure 2.7.: Results from PyECLOUD simulations for an LHC arc dipole: (a) Magnitude of the electric field of the proton beam within the simulation domain, (b) Snapshot of the electron distribution for an SEY=1.4 taken right before a bunch passage in the saturation regime, (c-d) Horizontal and vertical component of the electric field generated by the EC around the baffle region.

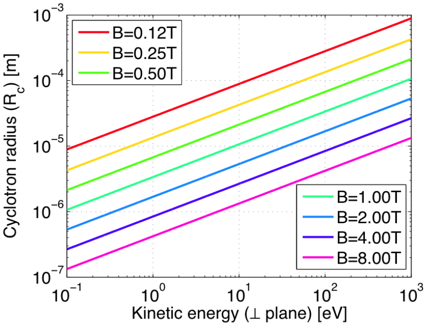

Figure 2.8.: Cyclotron radius as a function of the magnetic field and of the kinetic energy. Courtesy of G. Iadarola.

electrons does not exceed a few tens of electronvolts and so their cyclotron radius does not exceed a few hundreds of micrometer, which is significantly smaller than the size of the pumping slot. In practice the magnetic field is guiding the electrons emitted from the baffle plate towards the inside of the chamber.

The heat loads deposited on the baffle and on the cold bore, for the cases with and without baffle, respectively, have been simulated as a function of the SEY of the surface and compared with the heat load on the whole chamber. These results are shown in Fig. 4.8.

Even for SEY values as low as 1.4, as achieved in the LHC after the 2015 extended scrubbing campaign, the heat load deposited on the cold bore due to the effect of a single hole is of the order of 0.15 W/m, definitely non-negligible when compared to the cooling capacity available on the beam screens, which is of the order of 1.0 W/m. Therefore, this study confirms the importance of installing shielding baffles suggesting that they should be also included in the design of the new magnets foreseen by the HL-LHC upgrade.

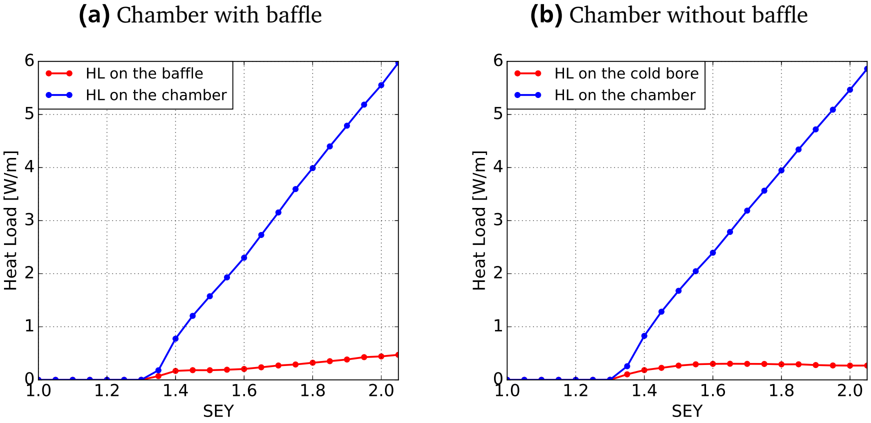
(a) Chamber with baffle

(b) Chamber without baffle

Figure 2.9.: Heat load induced by the EC as a function of the SEY: (a) Heat load deposited on the whole chamber and on the baffle plate, (b) Heat Load deposited on the whole chamber and on the cold bore, in the case in which the baffle plate is not installed.

2.3 EC buildup studies in the SPS main magnets

In the early years of 2000, observations of pressure rise, beam instability and emittance growth in the SPS pointed to the presence of the EC which limited the capability of this accelerator of handling LHC-type beams [57].

In order to mitigate these detrimental effects, regular scrubbing runs (lasting from few days to two weeks) were carried out almost every operational year between 2002 and 2010 in order to achieve the necessary reduction of the SEY of the vacuum chamber and ensure a satisfactory beam quality. This strategy has proved successful and the SPS could produce nominal LHC beams without any visible beam degradation coming from EC as from 2011.

However, the post LS1 experience showed that higher intensity beams, like those foreseen by the LIU project, were still suffered from strong EC effects, causing both poor lifetime and coherent instabilities at the tails of the batches. Thus, a further reduction of the SEY is required in order to deliver the future beam [58]. In order to determinate the values of SEY thresholds for the EC buildup in the different beam chambers, an intensive simulation campaign has been performed using the PyECLOUD code. This allowed defining which components of the SPS are the most critical for the future LHC beams.

In Fig. 2.10, a schematic layout of an SPS arc half arc-cell is shown. It consists of MBA and MBB-type bending magnets, QF and QD magnets and Short Straight Section (SSS). Shapes and sizes of the corresponding chambers are also displayed. The aperture of the SSS is of the MBA, MBB or QF type. The SPS beam chambers are made of Stainless Steel (StSt). Based on PyECLOUD simulations, the corresponding SEY thresholds have been estimated both for the nominal bunch intensity and

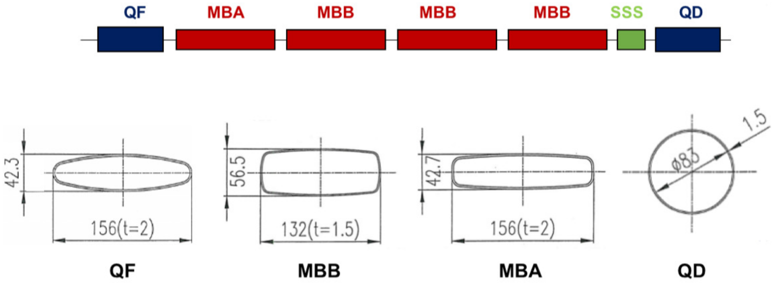

Figure 2.10.: Schematic layout of an SPS arc half-cell and drawings of the vacuum chamber types.

Machine element	Machine fraction	Field at 26GeV	Multipacting threshold (SEY)	
			$1.5 \cdot 10^{11}$ ppb	$2.5 \cdot 10^{11}$ ppb
MBA dipole	32.8%	0.2 T	1.60	1.60
MBB dipole	35.0%	0.2 T	1.35	1.40
QF quadrupole	4.8%	14.2 T/m	1.30	1.35
QD quadrupole	4.8%	14.2 T/m	1.05	1.15

Table 2.2.: SEY thresholds estimated for the five types of SPS vacuum chamber using the PyECLOUD code. Simulations were carried out for the standard 25 ns beam at injection energy (26 GeV) both with the nominal and the LIU target bunch current.

for the LIU parameters, and the results reported in Table 2.2. A detailed description of the obtained results of this study can be found in [59, 60].

According to the simulation results, the following features can be observed:

- the MBA-type chambers have the highest multipacting thresholds and, therefore, are the easiest to condition,
- MBB-type chamber, due to larger vertical size compared to MBA, exhibits lower threshold values at high intensity. Further studies showed that, under certain condition, they can be also responsible for triggering coherent instabilities [61],
- Quadrupole chambers show very low SEY thresholds. Particularly worrisome is the fact that these values are comparable or even lower compared to those achievable in conditioning experiments performed on StSt in the laboratory. This means that, even if they cover only a small fraction of the machine, they might suffer from large EC buildup even after extensive beam conditioning.

These results show that relying only on the scrubbing mitigation could be not sufficient to reach the required LIU performance target. For this reason, the option of coating different SPS componets with a thin film of a-C was also developed. Indeed, previous experimental studies showed that the a-C coating, which provides an SEY value around 1, can guarantee the full suppression of the EC in contrast to the case of uncoated StSt chambers. For more details see [26].

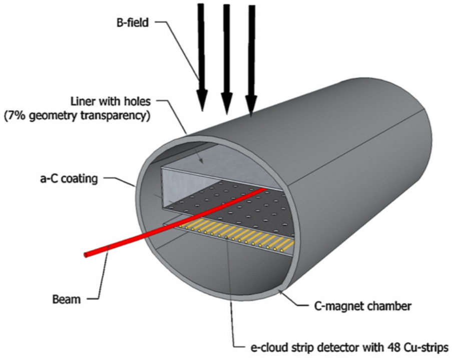

Figure 2.11.: Schematic view of the strip detector installed in the CERN SPS. Courtesy of C.Y. Vallgren

2.3.1 Comparison against experimental data

In order to crosscheck and improve our simulation model, data acquisition has been carried out with a EC dedicated equipment placed in the SPS machine. In the following, we will present the results of these measurements and compare them with the corresponding simulation outcome.

The strip detector (also called Electron Cloud Monitor (ECM)) measures the spatial distribution of the EC within the beam pipe with the aim of gaining additional insights of the EC buildup and its properties. In the SPS, four ECMs have been installed with different geometries and with different materials or treatments. A view of the detector installed in the SPS MBB is shown in Fig. 2.11. Each detector consists of 48 copper stripes parallel to the beam axis located in front of a perforated StSt liner having the same cross section as the vacuum chamber in the SPS bending magnets. The signal obtained corresponds therefore to the integrated electron current which penetrates through the holes (i.e. 2 mm diameter and 6 mm pitch). A detailed description of this device can be found in [26].

Figure 2.12a shows the EC cloud profile measured in the MBB chamber type for 25 ns beams at different magnetic field strengths. We can observe that when changing the magnetic field different EC patterns develop. This effect can be understood recalling that the electron cyclotron radius is strongly dependent on the magnetic field strength. In particular, at low field the motion of electrons is comparable to that in the free region due to their large cyclotron radius (e.g tens of millimeters). Conversely, for higher fields, the radius shrinks and electrons are practically constrained to move around the field line, resulting into the characteristic two-stripes structure.

In PyECLOUD, the ECM has been implemented such that it produces in output the signal obtained by the flux of electrons going through holes (modeled as perfect absorbers) in the chamber. A detailed description of the implemented model and the comparison between PyECLOUD simulations and previous studies performed with the ECLOUD code are discussed in [63, 64]. To benchmark against experimental data shown in Fig. 2.12a, simulations have been carried out assuming the same beam parameters and magnetic field configurations. The results are show in Fig. 2.12b. It can be observed that the simulation results closely represent the experimental data.

2.3.2 PyECLOUD simulations with coating profiles in the SPS

Over the years different techniques have been developed both for the *ex-situ* and *in-situ* a-C treatments in order to overcome potential constrains resulting from the geometry and surrading conditions of the object to be coated [65]. A better quality of the coating is usually obtained when it is realized in ad-hoc laboratories. The major drawback of the *ex-situ* option lies in the logistics to dismount the elements from the ring, transport them up to the facility and re-install after coating. To minimize the logistical impact of the coating implementation, an *in-situ* approach is, therefore, preferred [66]. In this case, the coating is realized directly inside the magnet with several advantages in terms of costs and required duration.

Recently, a new coating system has been developed at CERN to coat strings of component *in-situ* without removing them from their position inside the tunnel. This technique is called hollow cathode sputtering [67]. While the traditional *ex-situ* sputtering results in a more uniform coating, this method provides only two stripes of coating (i.e. one on the upper and the other on the lower surfaces of the vacuum chamber). First tests of this new configuration were performed in the SPS MBB-type chambers, showing promising results in terms of EC suppression.

The efficiency of the partial coating, as achievable with the hollow cathode procedure, has been also addressed with PyECLOUD simulations for the other components. In particular, the EC buildup in the MBB, MBA and QF-type chamber has been simulated for two different scenarios, one of which includes the presence of an externally applied magnetic field and the other one where the same chambers are used as drift. This is very common in the SPS SSS. The main results are summarized in Fig. 2.14, 2.13, 2.15. For all the components the EC buildup has been simulated at injection energy for the nominal bunch pattern made of four batches of 72 bunches with 25 ns spacing, with a 225 ns gaps between consecutive batches. The bunch intensity is $2.5 \cdot 10^{11}$ ppb, as foreseen by the LIU project. The applied

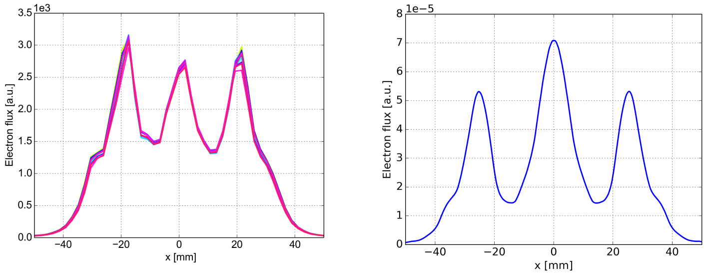
(a) Measurements
B=42 G

(b) Simulations
B=42 G

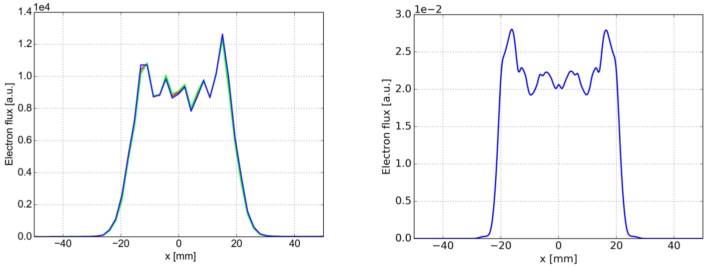
(c) B=125 G

(d) B=125 G

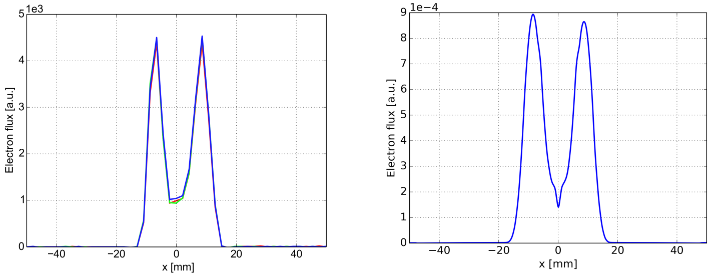
(e) B=830 G

(f) B=830 G

Figure 2.12.: Comparison between the measured (left) and the simulated (right) horizontal distribution of the electron flux in the SPS MBB-like chamber for a 25 ns beam with $1.2x10^{11}$ ppb and 2.3 ns long. The results are reported for different magnetic field strengths. At each configuration, the EC profile has been measured repeatedly over time and reported in the plots with different colors.

magnetic field for each type of magnet is listed in Table 2.2. Due to the presence of the coating, a non-uniform SEY distribution over the whole chamber has been assumed. In particular, the maximum value of SEY has been set at 1.1 at the position of the coating, while it has been scanned between 1.0 and 1.8 in the uncoated regions.

Figure 2.13 shows the simulation results for the MBB type chamber used both as dipole and as drift. Looking at Fig. 2.13b we can observe that for the MBB chamber used as dipole the partial coating is sufficient to fully suppress the EC buildup. In fact, as shown in Fig. 2.13d, the 6.5 cm wide layer of coating, placed on the top and on the bottom of the surface, matches exactly the position of the two-stripes structure preventing the EC to develop. The situation completely changes when the MBB profile is used as drift (see Fig. 2.13c). In this case, the EC buildup is more severe and it occurs even with the partial coating. This can be explained by the fact that in the drift space the electrons are free to move in the chamber (see Fig. 2.13e) and generate newly electrons when hitting the uncoated walls of the chamber. Even though the coating is not sufficient to suppress the EC, it provides a larger multipacting threshold (at around 1.55) compared to the bare StSt (at around 1.25) and, therefore, the chamber becomes easier to condition in an acceptable operational time. Indeed, measurements from the laboratory show that for the StSt the conditioning process saturates around SEY=1.3.

Figure 2.14 displays the simulation results for the MBA type chamber. Comparing Figs. 2.14b-2.14c against 2.13b-2.13c, we can observe the MBA profile exhibits larger SEY thresholds compared to the MBB, while the electron distribution within the beam pipe is very similar (see Figs. 2.14d-2.14e and 2.13d-2.13e). The difference between the two is mainly in the beam chamber's profile. Due to the smaller vertical size, the EC in the MBA chamber is less severe than in the MBB. For this reason, assuming an SEY below than 1.8 for the uncoated part, the partial coating is sufficient to fully suppress the EC both for the MBA used as dipole and as a drift space.

Concerning the QF profile, the behavior of the EC is very similar to the MBA case when it is used as drift space (see Fig. 2.15c). In the presence of the magnetic field, the situation is slightly different. In fact, due to the presence of the quadrupole magnetic field, the electron cloud distribution assumes a cross-like shape which covers a wider region of the beam chamber with respect to the stripe structure in the dipole (compare Figs. 2.14d and 2.15d). For this reason, layers of coating of 8 cm, instead of 6 cm, need to be implemented in order to suppress the EC.

(a) MBB-type chamber

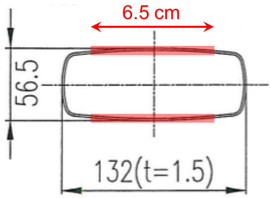

(b) As dipole **(c)** As drift

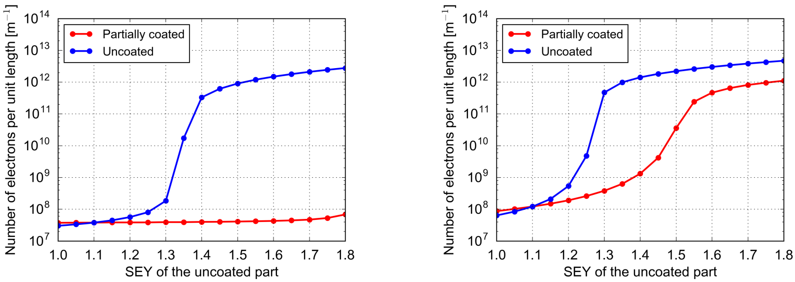

(d) As dipole (Uncoated chamber) **(e)** As drift (Uncoated chamber)

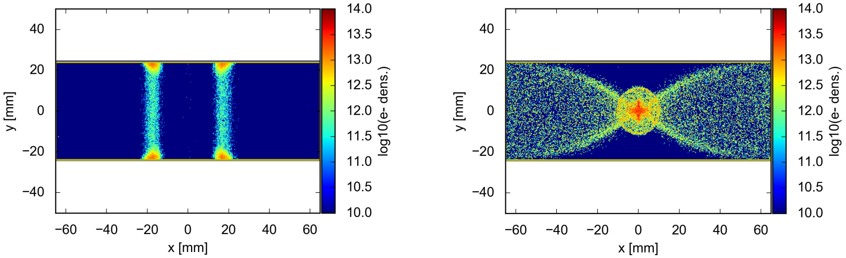

Figure 2.13.: Transverse profile of the MBB-type beam chamber with thin film a-C coatings as achievable with the hollow cathode procedure indicated in red. Results of the corresponding the PyECLOUD simulations are shown both for the dipole configuration (left) and for the drift (right): (b-c) number of electrons as a function of the SEY of the uncoated chamber's part, (d-e) snapshots of the electron cloud density within the uncoated beam pipe with the EC in a saturation regime for an SEY=1.4.

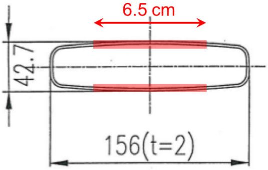

(a) MBA-type chamber

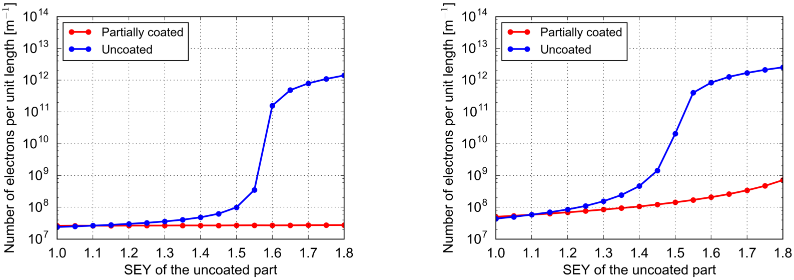

(b) As dipole

(c) As drift

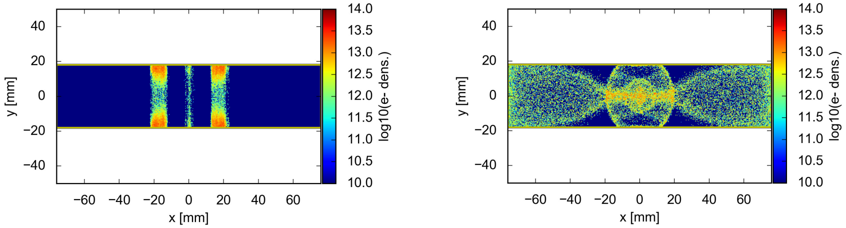

(d) As dipole (Uncoated chamber)

(e) As drift (Uncoated chamber)

Figure 2.14.: Transverse profile of the MBA-type beam chamber with thin film a-C coatings as achievable with the hollow cathode procedure indicated in red. Results of the corresponding the PyECLOUD simulations are shown both for the dipole configuration (left) and for the drift (right): (b-c) number of electrons as a function of the SEY of the uncoated chamber's part, (d-e) snapshots of the electron cloud density within the uncoated beam pipe with the EC in a saturation regime for an SEY=1.4.

(a) QF-type chamber

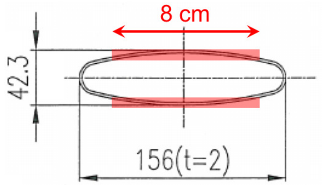

(b) As quadrupole

(c) As drift

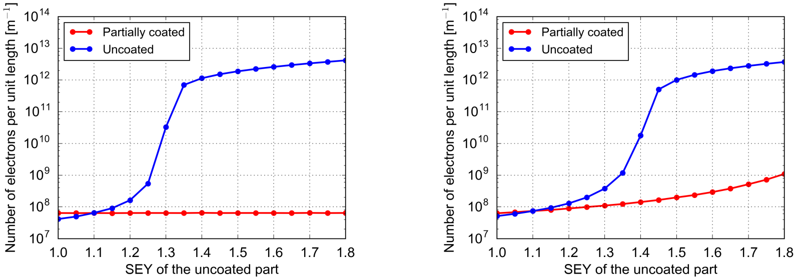

(d) As dipole
(Uncoated chamber)

(e) As drift
(Uncoated chamber)

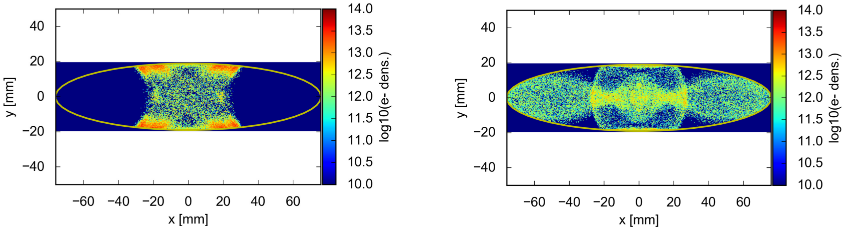

Figure 2.15.: Transverse profile of the QF-type beam chamber with thin film a-C coatings as achievable with the hollow cathode procedure indicated in red. Results of the corresponding the PyECLOUD simulations are shown both for the dipole configuration (left) and for the drift (right): (b-c) number of electrons as a function of the SEY of the uncoated chamber's part, (d-e) snapshots of the electron cloud density within the uncoated beam pipe with the EC in a saturation regime for an SEY=1.4.

3 Transverse beam instability studies for the LHC and HL-LHC

It is well-known that particle positively charges bunches going through an EC may suffer coherent instabilities caused by the coupled motion between the electrons and the particle beam [5]. In the present chapter, we will focus on the instabilities which develop within a single bunch, namely single-bunch instabilities.

When the head of the bunch enters the EC with a slight offset, an asymmetric pinch will take place resulting into a net kick felt by the bunch tail. After several turns, the offset in the head can be transferred and amplified at the tail of the bunch until the unstable coherent motion has propagated to the whole bunch [68]. This simplified picture of the beam-EC interaction can be applied only if the synchrotron period is much longer than the instability rise time.

In the past, several attempts have been made in order to develop analytical models and find correspondences with existing theories [33]. However, due to the complexity of this mechanism, numerical simulations appear indispensable for a proper prediction and understanding of the instability dynamics.

At CERN, these effects have been studied using the PyECLOUD-PyHEADTAIL simulation suite (see Sec. 1.3). Even though advanced features have been implemented in the codes, the computational burden is still quite heavy. Indeed, a typical instability simulation study to identify the instability threshold as a function of the EC density requires hundreds of CPU cores organized in jobs using 8-16 cores each. Three to four weeks of computing time are needed to simulate 10^4 turns, which is the time scale of the instability rise-time experimentally observed in the LHC.

In the following sections, we will discuss the main results of simulations studies performed to explain the underlying mechanism of these observations and estimate the threshold in different operating conditions. Unless stated otherwise, the main simulations parameters are listed in Table 4.1 and Table 3.2. Sensitivity studies are presented in the Appendix A.

Parameters	Symbol	Value	
		Injection	Collision
Beam energy [GeV]	E	450	6500
Bunch population [ppb]	N_b	$1.1\text{x}10^{11}$	$1.0\text{x}10^{11}$
Bunch spacing [ns]	s_b	25	
Rms. beam size [μm]	$\sigma_{x,y}$	3.0	2.5
Rms. bunch length [m]	$4\sigma_z$	0.09	0.075
Average beta function [m]	$\beta_{x,y}$	92.7, 93.2	
Peak dipole field [T]	B	0.53	7.8
Quadrupole gradient [T/m]		12.1	175
Chromaticities	$Q'_{x,y}$	15,15	
Octupoles current [A]	I_{oct}	26	471
Transverse feedback damping time [turns]		50	100

Table 3.1.: LHC beam and machine parameters.

Parameters	Symbol	Value	
		Injection	Collision
# of macroelectrons	Nel	$2{\cdot}10^6$	
# of macroprotons	Npr	$7{\cdot}10^5$	
# of slices	Nbin	150	
# of interaction point	nkick	15	
Internal grid size (within $10\sigma_x$) [m]		$1.4{\cdot}10^{-4}$	$4{\cdot}10^{-5}$
External grid size [m]		$0.8{\cdot}10^{-3}$	$0.8{\cdot}10^{-4}$

Table 3.2.: Numerical parameters used for the simulations.

3.1 EC induced instabilities in the LHC at injection energy

The experience from the 2015-2017 run has shown that the EC effects can pose important challenges to the LHC operation especially in terms of beam stability [29]. To address this point, tests at injection energy were performed with the so-called "8b+4e" bunch pattern. It consists of short trains of eight bunches with 25 ns spacing, separated by four empty slots, for which the EC is largely suppressed as illustrated in Fig 3.1. The plot shows a snapshot of bunch-by-bunch power loss from the phase shift measurements along a selected part of dedicated test [69]. The main characteristic of this test was that the filling scheme was made by alternating injections of "8b+4e" trains with 25 ns trains (in total 1908 bunches per beam).

One can observe a rising EC pattern along the 25 ns trains and a flatter structure, corresponding to negligible stable phase shift due to EC, for the "8b+4e" trains.

In order to confirm the EC is the main driver of the observed instabilities, we compared two test fills performed with "8b+4e" scheme (see Fig. 3.2a) and the 25 ns configuration (see Fig. 3.2b). In Fig. 3.2, the plots on the left side show the injection process, while those on the right side display snapshots of the horizontal emittance measurements from the Beam Synchrotron Radiation Telescope (BSRT). The color of each scan is chosen according to the convention shown in the left plots. The behavior in the vertical plane is very similar.

The "8b+4e" beam could be injected using low chromaticity and octupole settings ($Q'_{H,V}$=5 units, $\mathrm{I_{oct}}$=6.5 A) without observing any instability or fast emittance blow up. Conversely, when injecting the 25 ns beam with the same settings, a strong instability developed right after the first injection leading to a strong emittance blow up both in the horizontal and the vertical plane. A clear reduction of the emittance growth was reached by gradually increasing the chromaticity and octupoles settings. The background colors reported in Fig. 3.2b indicate the chromaticity and octupole settings when each train was injected, as labeled in the table reported in the upper part of the plot. It is evident that a satisfactory emittance preservation could be reached when approaching the operational machine settings ($Q'_{H,V}$=15/20 units, $\mathrm{I_{oct}}$=6.5 A), proving that the standard LHC beam is stable only with large values of chromaticity and octupoles current.

In order to explain the underlying mechanism of these observations, an extensive simulation campaign has been performed using the PyECLOUD-PyHEADTAIL

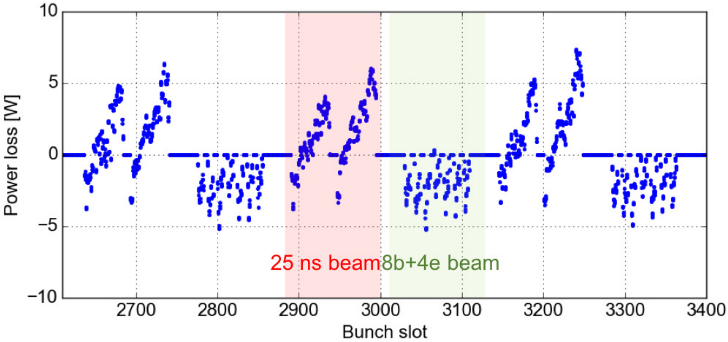

Figure 3.1.: Bunch-by-bunch stable phase shift for Beam 1 during a test fill combining trains with the "8b+4e" bunch pattern with the standard trains with 25 ns bunch spacing.

(a) "8b+4e" scheme

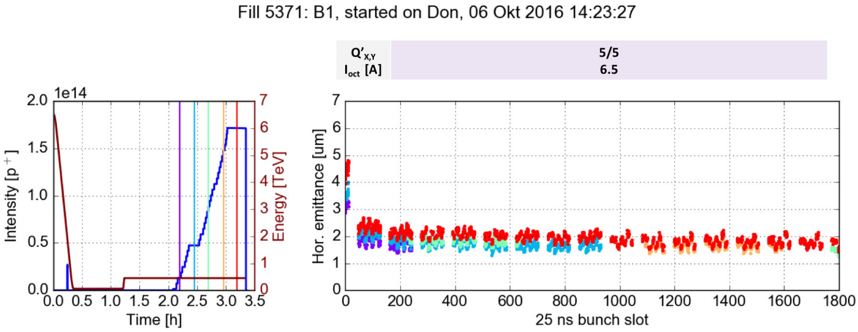

(b) 25 ns scheme

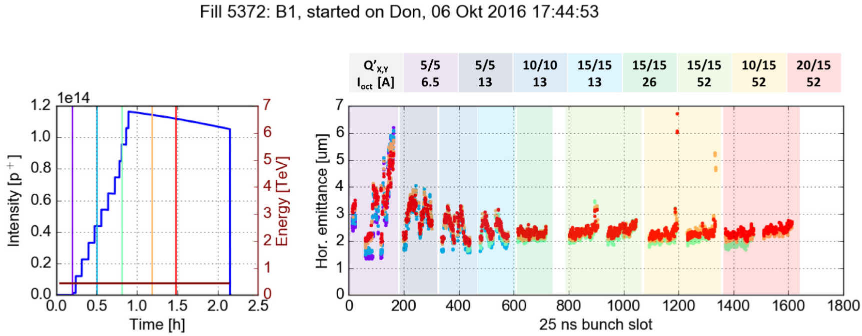

Figure 3.2.: Comparison of the bunch-by-bunch horizontal emittance measurements between the "8b+4e" scheme (a) and the standard 25 ns beam (b). Left: total beam intensity of Beam 1. Right: snapshots of the measurements from the BSRT. The color of each scan is chosen according to the convention shown in the left plots. The colored backgrounds associate the setting values to the different injections into the LHC, as reported in the table on top of each plot. The behavior in the vertical plane is very similar.

suite. The study aimed at evaluating the threshold for the coherent instability in the dipole and quadrupole magnets and at investigating potential mitigation strategies.

3.1.1 Effect of the EC in the dipole magnets at injection energy

We first look at the simulation results obtained for the dipole magnets, which cover the largest fraction of the LHC circumference, i.e. about 65%. In this case, the simulations have been initialized with a uniform electron distribution within the vacuum chamber, corresponding to the electron density at the beam location. This was found to be a good approximation in the presence of a dipolar magnetic field [70].

Figure 3.3 shows the evolution of the horizontal and vertical position of the bunch centroid and of the corresponding transverse emittance, for an initial electron density scanned from $1 \cdot 10^{11} \mathrm{e}^{-}/\mathrm{m}^3$ to $9 \cdot 10^{11} \mathrm{e}^{-}/\mathrm{m}^3$ (the electrons are at rest before the bunch passage). It can be observed that the behavior in the two planes is strongly asymmetric, as the presence of a dipolar magnetic field forces the electrons to move along the magnetic field lines. In particular, the horizontal instability exhibits a lower threshold electron density but, above threshold, the vertical instability has a much faster rise-time. The instability thresholds in the horizontal and vertical plane are found at around $5 \cdot 10^{11}$ and $9 \cdot 10^{11}$, respectively.

To check whether the EC in the dipole magnets is sufficient to drive the beam unstable at injection, we compared the instability threshold with the estimated electron density at the beam location. Figure 3.4 shows the horizontal distribution of the electron density within the beam chamber estimated with the PyECLOUD buildup simulation assuming a maximum SEY of the chamber surface of 1.4. This value has been inferred from heat load measurements performed at the end of the 2016 scrubbing run.

It is evident that the central electron density in the LHC dipole magnets, in the present conditioning state of the machine, is well below the identified threshold. This means that even with chromaticity and octupoles set to zero, the EC in dipoles is not expected to cause observable instabilities in the LHC at injection.

The impact of the machine settings such as chromaticity, octupoles and transverse feedback on the instability development has been also investigated. To that purpose, we considered the case in which the EC density in the dipole chamber is equal to $1 \cdot 10^{12} \mathrm{e}^{-}/\mathrm{m}^3$ as it is well above the instability threshold.

Firstly, we introduced in our simulation setup the transverse feedback, which has been modeled as an ideal bunch-by-bunch system. The aim of this device is to damp the transverse position of the bunch centroid with a specified gain [71]. Figure 3.5 shows the effect of the feedback system on the bunch oscillations both in the horizontal and in the vertical plane. It can be observed that in the horizontal plane

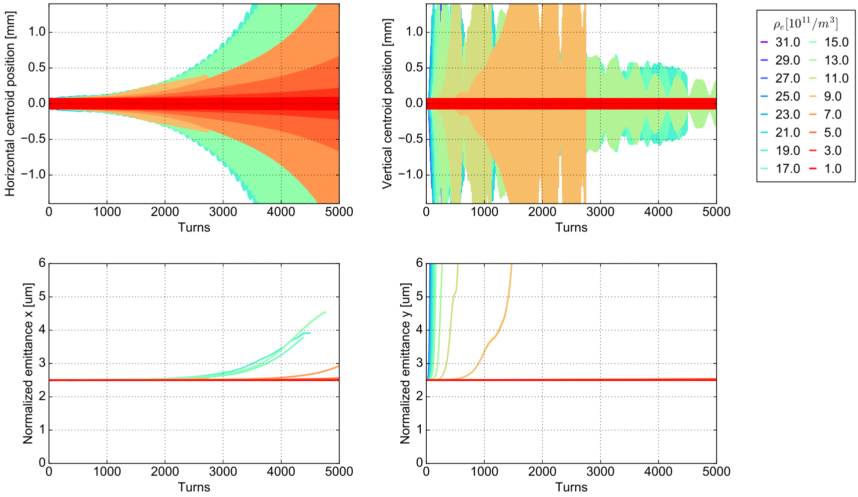

Figure 3.3.: Evolution of the horizontal and vertical position of the centroid of the bunch and of its transverse emittance for different initial EC densities in dipoles. No EC in the quadrupoles, no chromaticity, no current in the octupoles and no transverse feedback system are included in the simulation setup. The instability thresholds in the horizontal and vertical plane are found at around $5 \cdot 10^{11}$ and $9 \cdot 10^{11}$, respectively.

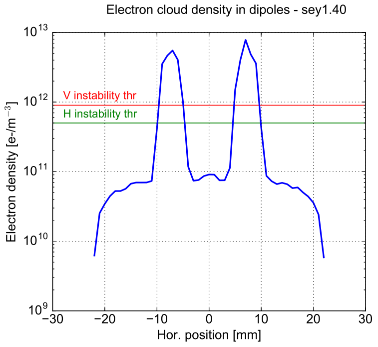

Figure 3.4.: Horizontal distribution of electron density in a dipole chamber estimated with the PyECLOUD buildup simulation for a maximum SEY of the chamber surface of 1.4. The red and green solid lines show the estimated density threshold as obtained from PyECLOUD-PyHEADTAIL simulations.

the bunch motion is detected and fully suppressed, while in the vertical plane the feedback system does not damp the transverse oscillation but it makes it less severe and delays it. This different behavior can be understood by looking at the Fig. 3.6. The plot shows the intra-bunch motion over 150 consecutive turns after the instability development both in the horizontal and in the vertical plane. It is evident that bunch particles oscillate differently in the two planes. In the horizontal plane the signal reveals a mode-0 (i.e. bunch slices having different longitudinal coordinates oscillate in phase) bunch oscillation, whereas in the vertical plane higher order intra-bunch modes are excited. Since the transverse feedback provides a constant kick along the bunch, only rigid transverse oscillations can be effectively damped. Therefore, when the feedback is active, the horizontal instability is not expected to be triggered by the presence of the EC in the dipole magnets.

Concerning the vertical instability, the most effective stabilizing effect is provided by chromaticity. Figure 3.7 shows the evolution of the vertical position of the bunch centroid and of its transverse emittance for different Q'_V. To realistically simulate the LHC operation conditions, we also included in the simulation model the feedback system and a transverse detuning from the octupoles of about $1 \cdot 10^{-3}$, which corresponds to a current of 26 A. We can note that the octupoles and feedback alone cannot guarantee the bunch stability for a such strong EC density. On the contrary, a large value of chromaticity both guarantees a full suppression of the bunch oscillations and avoids the strong emittance growth.

3.1.2 Effect of the EC in the quadrupole magnets at injection energy

In order to assess the underlying mechanism of the observed instabilities, especially in the horizontal plane, the role of the EC in quadrupoles alone has also been investigated. The quadrupole magnets constitute about 7% of the total length of the LHC. However, due to the trapping effect from the quadrupole gradient the electron density at the beam location can be very high, i.e. up to $10^{13}\mathrm{e}^-/\mathrm{m}^3$.

Previous studies [72] have shown in this case that the EC pinch dynamics is very sensitive to the initial phase space distribution of the electrons again due to the trapping effect. For this reason, we initialized the simulations using MPs coordinates and velocities imported directly from PyECLOUD buildup simulations. These were saved right before the bunch passage, with the EC in the saturation regime and for a maximum SEY of 1.3. With the EC density fixed according to the SEY, sensitivity studies have been performed by changing the weight of the EC kick, i.e. the fraction of the LHC circumference occupied by quadrupoles.

The evolution of the horizontal and vertical bunch centroid and of its transverse emittance are plotted in Fig. 3.8. The instability behavior in the two planes is very similar as the presence of a quadrupolar magnetic field does not cause a strong

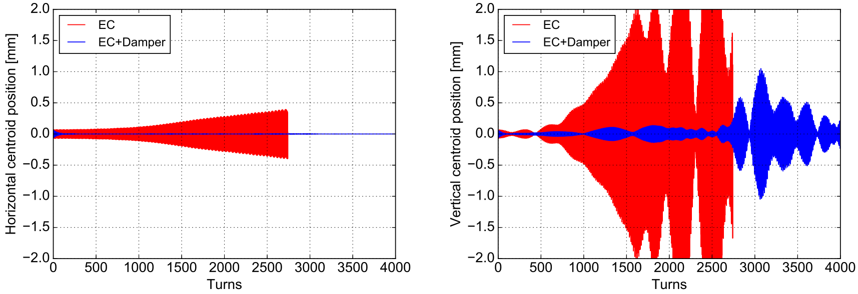

Figure 3.5.: Evolution of the horizontal and vertical bunch centroid position with (in blue) and without (in red) the transverse feedback system. The EC in the dipoles has been assumed equal to $1 \cdot 10^{12} \mathrm{e}^{-}/\mathrm{m}^{3}$. The damping time of the transverse feedback is listed in Table 4.1. No EC in the quadrupoles, no chromaticity, no current in the octupoles are included in the simulation setup.

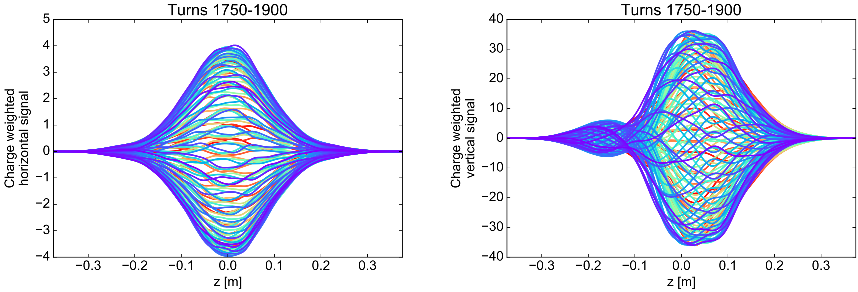

Figure 3.6.: Simulated intra-bunch oscillations in the horizontal and vertical plane over 150 consecutive turns and for an EC density in the dipoles of $1 \cdot 10^{12} \mathrm{e}^{-}/\mathrm{m}^{3}$. The damping time of the transverse feedback is listed in Table 4.1. No EC in the quadrupoles, no chromaticity and no current in the octupoles are included in the simulation setup.

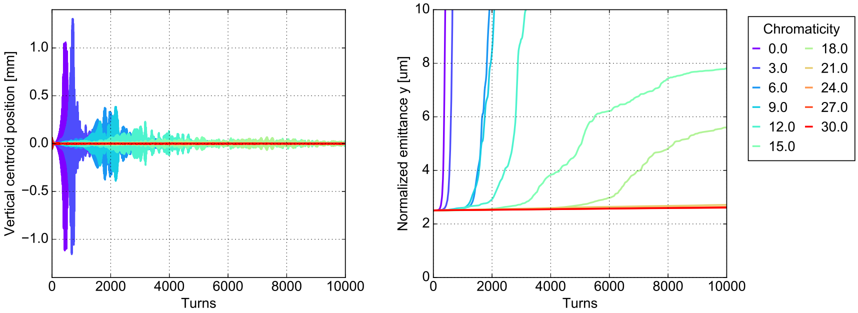

Figure 3.7.: Evolution of the vertical position of the bunch centroid and of its transverse emittance for different values of chromaticity. The octupole current and the transverse feedback damping time are listed in Table 4.1. The horizontal plane has been stabilized with Q'_h=40. No EC in the quadrupoles is included in the simulation setup.

asymmetry. It can be observed that in both cases the instability threshold is found to be below the actual total length of the quadrupoles. This indicates that, in the absence of octupoles and chromaticity, the EC in the quadrupoles alone is indeed able to drive the beam unstable at injection.

Figure 3.9 shows the simulated intra-bunch motion for the realistic length of the quadrupoles. It is evident that this type of instability cannot be damped by the standard bunch-by-bunch transverse feedback because it excites high order intra-bunch modes. In fact, as shown in Fig. 3.10, the feedback system helps in reducing the bunch oscillation but does not mitigate the emittance growth.

Alternative mitigation strategies have been therefore investigated. As first step, we introduced 5 units of chromaticity in both planes ($Q'_{H,V}$=5/5) and powered the octupoles with a current ranged between 6.5 A to 52 A. The combined effects on the instability development of these settings, including also the feedback system, is shown in Fig. 3.11. The presence of the octupoles does not seem to stabilize the beam at any reasonable current close to the operation value of 26 A. Indeed, even if the bunch oscillation is significantly reduced, a strong emittance growth starting either from horizontal or from vertical plan is still visible. An overall instability suppression is achieved only when doubling the current.

The most effective stabilizing effect comes again from the chromaticity, as shown in Fig. 3.12. In order to simulate the LHC operational conditions, we fixed the octupole current at 26 A and scanned the chromaticity from 5 units up to 20 units. It can be observed that the chromaticity increase prevents the instability to develop

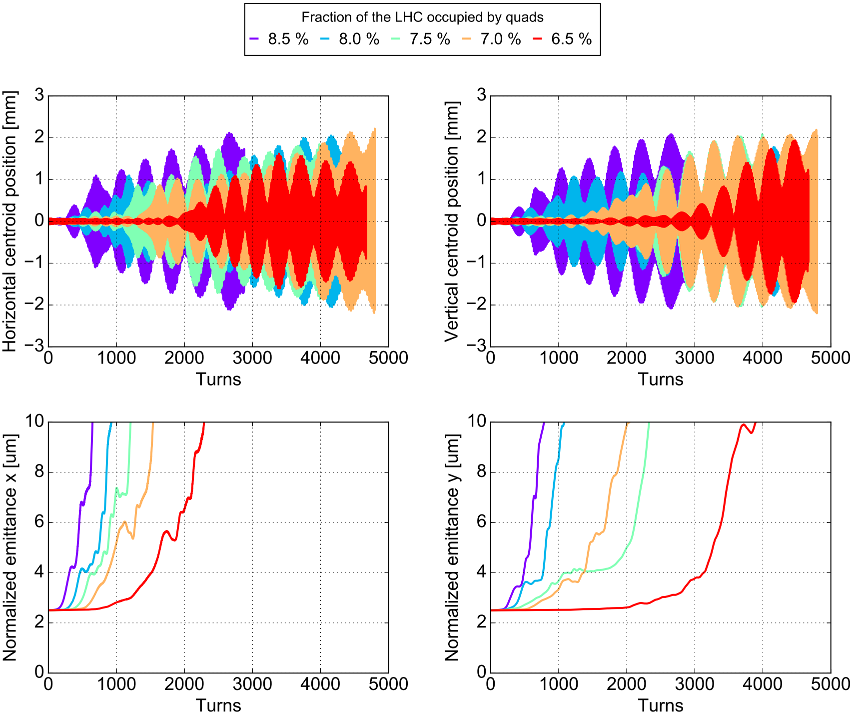

Figure 3.8.: Evolution of the horizontal and vertical position of the bunch centroid and of its transverse emittance for different fractions of the LHC circumference occupied by quadrupoles. No EC in the dipoles, no chromaticity, no current in the octupoles and no transverse feedback system are included in the simulation setup. The instability thresholds in the horizontal and vertical plane are found to be below 7%, which is the actual total length of the quadrupoles.

in the two transverse planes, consistently both with experimental observations and with previous studies performed on a much smaller number of turns [73]. This confirms that the beam stability with the standard 25 ns scheme can only be preserved with large $Q'_{H,V}$, relatively high octupole current and a fully functional transverse feedback.

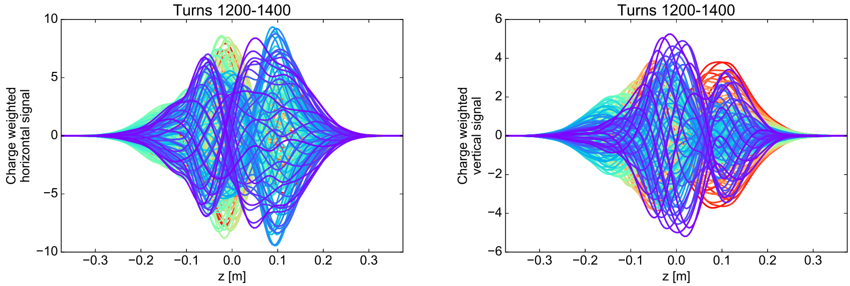

Figure 3.9.: Simulated intra-bunch oscillations in the horizontal and vertical plane over 150 consecutive turns assuming the realistic total length of quadrupoles. No EC in the dipoles, no chromaticity, no current in the octupoles and no transverse feedback system are included in the simulation setup.

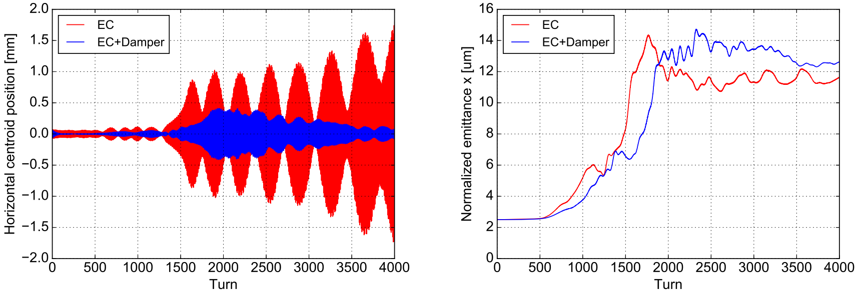

Figure 3.10.: Evolution of the horizontal and vertical bunch centroid position with (in blue) and without (in red) the transverse feedback system assuming the realistic total length of quadrupoles. The damping time of the transverse feedback is listed in Table 4.1. No EC in the dipoles, no chromaticity and no current in the octupoles are included in the simulation setup.

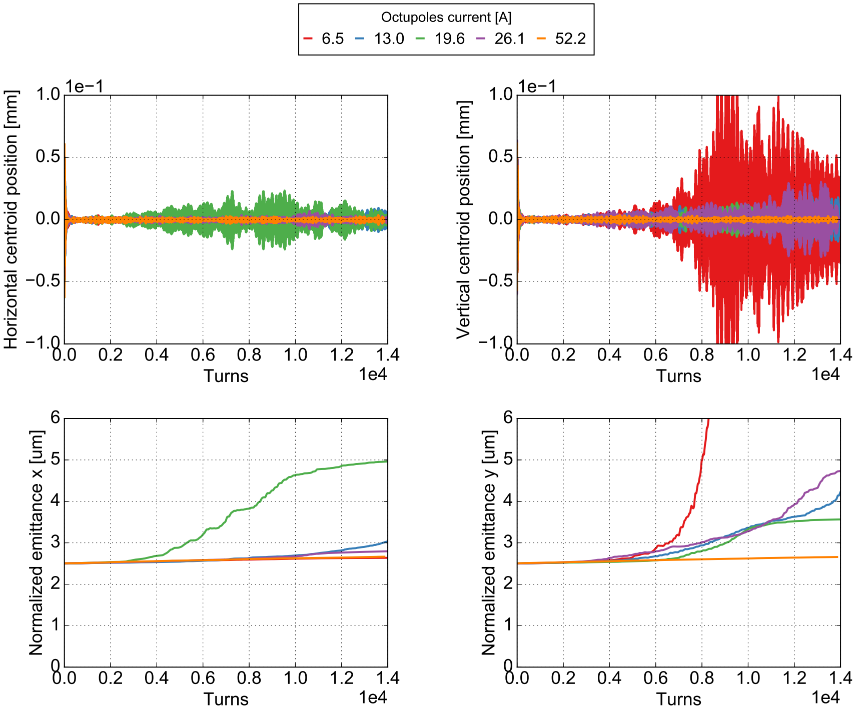

Figure 3.11.: Evolution of the horizontal and vertical position of the bunch centroid and of its transverse emittance for different currents in the octupoles. The chromaticity is equal to 5 units in both planes. The damping time of the transverse feedback system is listed in Table 4.1. No EC in the dipoles is included in the simulation setup.

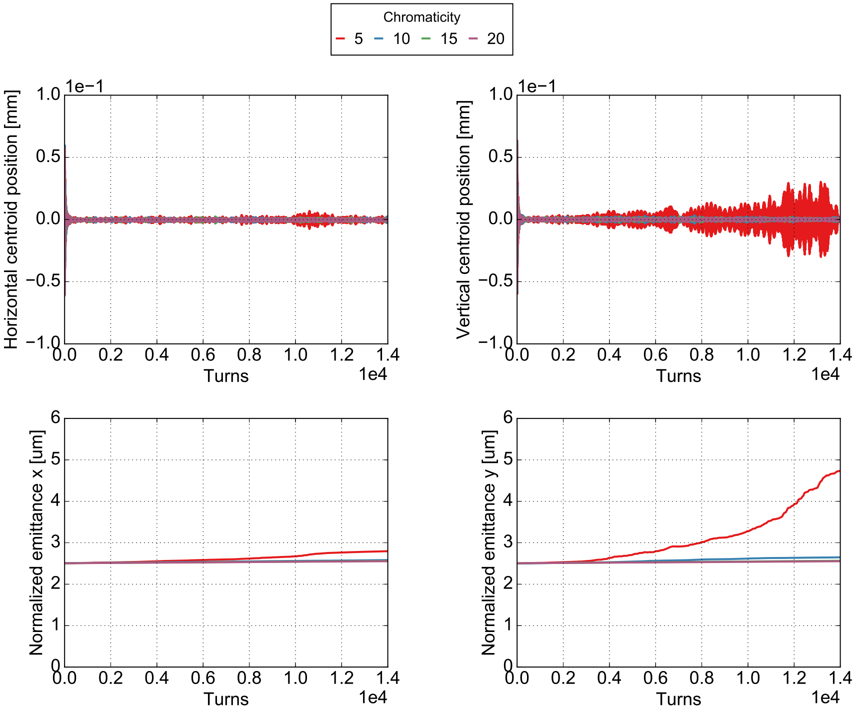

Figure 3.12.: Evolution of the horizontal and vertical position of the bunch centroid and of its transverse emittance for different for different chromaticity values. The octupole current and the transverse feedback damping time are listed in Table 4.1. No EC in the dipoles is included in the simulation setup.

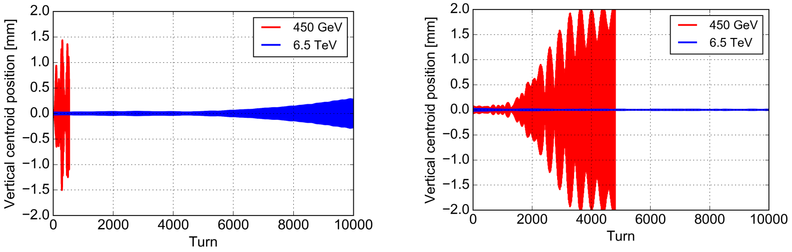
(a) EC in the dipoles

(b) EC in the quadrupoles

Figure 3.13.: Effect of the increased beam rigidity on the instability by the EC in the dipoles (left), assuming ρ_e=$26 \cdot 10^{11}\mathrm{e}^-/\mathrm{m}^3$], and in the quadrupoles assuming their realistic total length and SEY=1.3. No chromaticity, no current in the octupoles and no transverse feedback system are included in the simulation setup.

3.2 EC induced instabilities in the LHC at collision energy

The impact of the EC on the beam dynamics has been also studied at the LHC collision energy (i.e. 6.5 TeV for the 2015-2018 run). Simulation results show that an increase of the particle energy leads to an increase of the beam rigidity, which in turn results into a significantly lower instability growth rate. This effect is evident for the dipoles and even more for the quadrupoles, as shown in Figs. 3.13a and 3.13b. In fact, looking at the Fig. 3.14, we can note that, unlike in the 450 GeV case, the EC in the quadrupoles does not drive any clear instability or emittance growth over 10^4 turns. In the dipoles (see Fig. 3.15), instabilities triggered by the EC can still be observed but they are predominately vertical and the threshold is much larger compared to the injection one, $26 \cdot 10^{11}\mathrm{e}^-/\mathrm{m}^3$ instead of $9 \cdot 10^{11}\mathrm{e}^-/\mathrm{m}^3$. The possibility that an horizontal instability can be triggered by the EC in the dipoles will be discussed in Sec. 3.2.1. Relying on PyECLOUD buildup simulations, we compared the instability threshold with the estimated density at the beam location for a maximum SEY of 1.4. In order to correctly estimate the electron density within the chamber, we included in the buildup simulations the contribution of the photoemission from SR using the module described in [74]. As shown in Fig. 3.16, the estimated central density is found to be below the instability threshold, meaning that also the EC in the dipoles should not excite coherent instabilities. However, the situation changes significantly when the bunch intensity is lower than the nominal value. In this case, the central electron density can become significantly large to cross the instability threshold and can drive the beam unstable. This mechanism will be detailed in Sec. 3.2.2.

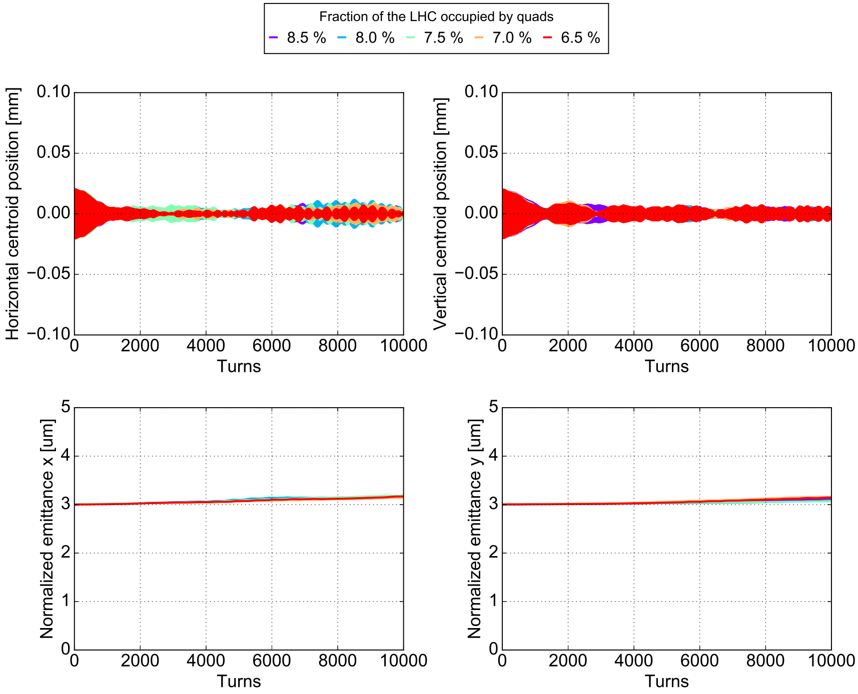

Figure 3.14.: Evolution of the horizontal and vertical position of the bunch centroid and of its transverse emittance for different fractions of the LHC circumference occupied by quadrupoles. No EC in the dipoles, no chromaticity, no current in the octupoles and no transverse feedback system system are included in the simulation setup. Any visible bunch degradation due to the EC is visible in this range.

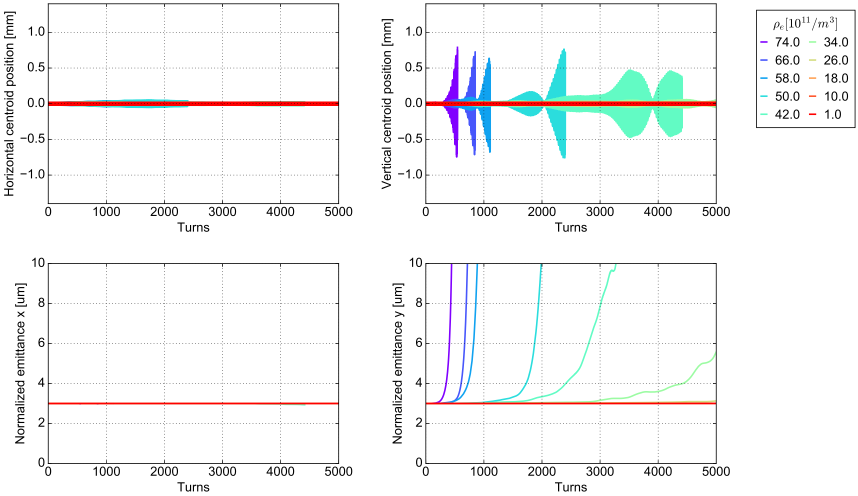

Figure 3.15.: Evolution of the horizontal and vertical position of the bunch centroid and of its transverse emittance for different initial EC densities in dipoles. No EC in the quadrupoles, no chromaticity, no current in the octupoles and no transverse feedback system are included in the simulation setup. The instability is predominantly vertical and its threshold is found at around $26 \cdot 10^{11} \mathrm{e}^{-}/\mathrm{m}^3$.

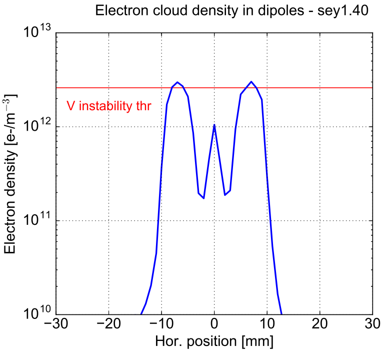

Figure 3.16.: Horizontal distribution of electron density in a dipole chamber estimated with the PyECLOUD buildup simulation for maximum SEY of 1.4. The red line shows the estimated density threshold as obtained from PyECLOUD-PyHEADTAIL simulations.

3.2.1 Horizontal instabilities arising from the EC in dipole magnets

In order to better understand the horizontal instability driven by the EC in the dipoles, we consider the case in which an EC density of $38\cdot 10^{11}\mathrm{e}^-/\mathrm{m}^3$ is uniformly distributed into the dipole chamber and we scan the horizontal chromaticity between -20 units and +20 units. Looking at the Figs. 3.17 and 3.18a, we can observe that a mode-0 like instability develops for chromaticities larger than 8 units, whereas for negative and low-positive values no bunch degradation is visible. Here the vertical plane has been stabilized with $Q'_V=40$.

Assuming a constant wake, the stability criterion for coherent mode-0 bunch oscillation can be written as [75]:

$$\frac{W_x \zeta}{\eta} < 0 \tag{3.1}$$

where ζ and η are the chromaticity and the slip factor, respectively, and W_x is the horizontal wake-field defined as:

$$W_x = -\frac{E_0}{q_p^2}\frac{\Delta x_2^{'}}{\Delta x_1} \tag{3.2}$$

where E_0 is the rest energy of the particles charge q_p, Δx_1 is the head displacement and $\Delta x_2^{'}$ is the kick felt by a trailing particle. To check the sign of W_x, we computed the transverse forces exerted by the EC over a single turn using the PyECLOUD-PyHEADTAIL suite. In the simulation, we displaced half of the bunch at the head side by an amount $\Delta x_1 = 0.5\cdot\sigma_x$ (see Fig. 3.19-top graph). For different bunch slices, we saved the average momentum (x') before and after the passage through the EC. Figure 3.19 shows the net kick from the EC as a function of the longitudinal position along the bunch. The same simulation has been repeated several times regenerating the bunch and the EC MP sets and the results were averaged. It can be observed that the horizontal forces on the tail tend to be opposite to the displaced head.

To some extent this is equivalent to having a positive horizontal wake-field, which is consistent with the fact that the stability can be only guaranteed with negative chromaticities (i.e η is positive for machine operating above transition). However, having a mode-0 structure, this type of instability can be fully suppressed by the feedback system, as confirmed by the simulation shown in Fig.3.18b. For this reason, this mechanism does not affect the nominal machine operation.

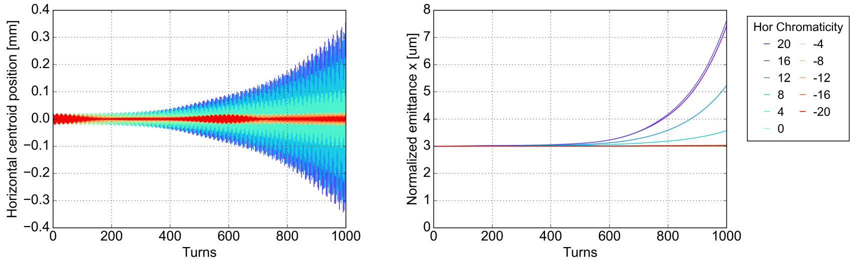

Figure 3.17.: Evolution of the horizontal centroid position of the bunch and of its normalized emittance for different values of horizontal chromaticity. The EC density in the dipoles is assumed equal to $38 \cdot 10^{11} \mathrm{e}^-/\mathrm{m}^3$. The vertical plane has been stabilized (Q'_V=40) in order to avoid the coupling as source of instability. No EC in the quadrupoles, no current in the octupoles and no transverse feedback system are included in the simulation setup.

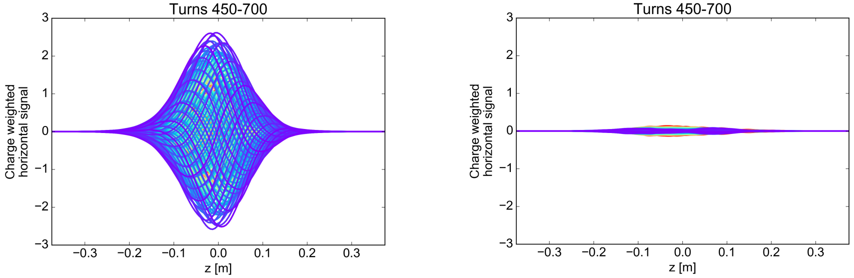
(a) Only Q_H

(b) Q_H and feedback system active

Figure 3.18.: Simulated intra-bunch signal for an EC density in the dipoles of $38 \cdot 10^{11} \mathrm{e}^-/\mathrm{m}^3$. Left: the horizontal chromaticity is set at 20 units. Right: combined effect of the same horizontal chromaticity (Q_H=20) and the transverse feedback system.

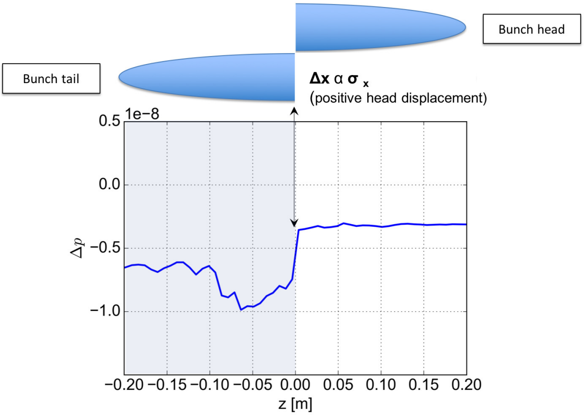

Figure 3.19.: Simulated net kick from the EC as a function of the longitudinal position along the bunch. A positive displacement, i.e. $\Delta x_1 = 0.5 \cdot \sigma_x$, has been applied to the head as schematically shown by the model on top of the plot.

3.2.2 Vertical instabilities driven by the EC in dipole magnets

The results discussed so far pointed out that the two-stripe structure of the EC in the dipoles cannot drive a nominal LHC bunch to go unstable, due to the very low central density. The situation changes for lower bunch intensities, for which the electron density at the beam location can become sufficiently large to trigger vertical instabilities even at 6.5 TeV, in spite of the significantly increased beam rigidity. This mechanism was indeed found to be responsible for the development of an anomalous instability observed at the beginning of 2016 run in the LHC. Some highlights on these observations and on the related simulation studies will be given in the following, while a more detail analysis can be found in [76].

During the first phase of the 2016 run, the LHC operation was affected by an anomalous instability which was observed systematically in most fills with more than 600 bunches. Its main characteristic was that, despite high chromaticity and octupoles current, it spontaneously appeared while both beams were stored for several hours in collision 6.5 TeV to provide data for the experiments, the so-called stable beams mode. Figure 3.20-left shows an example of bunch by-bunch emittance evolution along a circulating bunch train. The measurements were acquired in stable beams and they have been performed with the LHC BSRT. The instability manifested itself few hours after the collisions were established leading to a sudden emittance blowup exclusively in the vertical plane. Based on these measurements, we could also investigate which bunches along the train were mostly affected. Figure 3.20-right shows the bunch-by-bunch emittance pattern along four trains. In particular, the grey region highlights the same train shown in the plot on the left side. Measurements were taken 2 h and 6 h after the beginning of the collisions, respectively. It is evident that the bunches becoming unstable are those at the tails of the bunch trains.

More generally, Fig. 3.21 displays the occurrence of the vertical emittance blow-up as a function of the bunch number within the trains, calculated over all physics fills in which the instability was observed. The plot shows a very clear instability pattern. Moreover, it also suggests that shorter trains (e.g. 48 bunches) could be less affected by the EC effects and thus result in being more stable. Due to these distinguishing features, the EC was strongly suspected as the main driving mechanism for these instabilities.

In order to gain a further insight into the origin of this phenomenon, we investigated the dependence of the instability onset on the beam intensity. In fact, due to the collisions, an unavoidable beam intensity decay occurs when the beams are in collision. This mechanism includes the luminosity burn-off and possibly the effect of dynamic aperture limitations coming from head-on and long range beam-beam interactions. We found out that most of the instabilities were observed when the beam intensity had decreased to values corresponding to bunch intensities between $1 \cdot 10^{11}$ and $0.7 \cdot 10^{11}$ ppb.

The strategies employed to mitigate and experimentally characterize this instability can be summarized as follows.

Starting from the beginning of June 2016, the vertical chromaticity was increased from 15 up to 22 units for both beams right after the stable beams started. This approach provided sufficient mitigation against the beam instability, as shon by previous studies [77], and allowed to keep injecting 72-bunch trains into LHC. The beneficial impact of the chromaticity on the beam stability is shown in Fig. 3.22. The graphs display the bunch-by-bunch luminosity measured by the CMS experiment during two fills with different vertical chromaticities. The luminosity of each bunch is normalized to the value measured at the beginning of stable beams and a red point marks any sudden reduction in luminosity due to the emittance blowup. Figure 3.22a refers to a physics fill operated with $Q'_y = 15$, whereas Fig. 3.22b refers to a fill for which the vertical chromaticity was increased by 7 units. In the latter case, an overall reduction of the number of unstable bunches could be observed as well as a delay in the instability development.

At the end of June 2016, the production scheme in the injectors was changed to increase the beam brightness [78]. With the new scheme the beam was made of trains of 48 consecutive bunches instead of the nominal 72 bunches. The first physics fills after the change were performed by following the same approach as

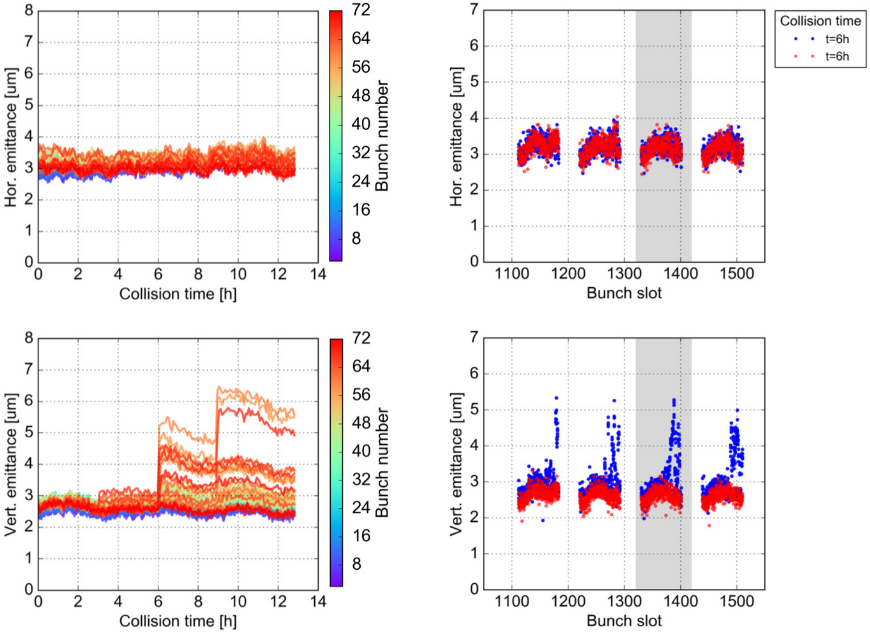

Figure 3.20.: Instability observations at the LHC at 6.5 TeV. Left: evolution of the horizontal and vertical bunch-by-bunch emittance for one of the circulating bunch train. Different bunches are marked with different colors. The measurements were acquired in stable beams and they have been performed with the LHC BSRT. The gray region highlights the train shown in the plot on the left. The measurements were taken about 2 h and 6 h after the collisions were established.

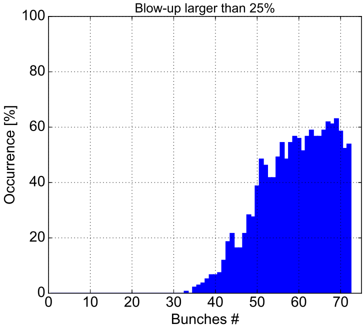

Figure 3.21.: Occurrence of a vertical emittance blow-up larger than 25% as a function of the position within the bunch train. The analysis includes all physics fills in which the instability was observed. The plot refers to Beam 1. A similar behavior was observed in Beam 2.

described above. However, as this filling pattern is naturally less prone to EC effects, it was possible to gently reduce the increase of vertical chromaticity, (from 22 → 18 → 16) until the nominal setting was restored (i.e. $Q'_y = 15$), without any instability observation.

In August 2016, dedicated tests have been done during Machine Development sessions to better assess the impact of the bunch intensity and the chromaticity on the instability development. Three fills were performed in trains of 72 bunches with various bunch intensities (e.g. $1.1 \cdot 10^{11}$, $0.9 \cdot 10^{11}$, $0.7 \cdot 10^{11}$ ppb). The full operational cycle to bring the beams into collision was performed and, after 1.5 h in stable beams, the vertical chromaticity was reduced to 5 units in small steps. Based on the BSRT and CMS luminosity data, no detrimental effects on the beam stability were observed. The instability disappeared, even with low chromaticity, probably thanks to the scrubbing of the central region of the beam screen accumulated with physics fills in the previous weeks.

In order to understand the driving mechanism of this instability, an extensive simulation campaign with the PyECLOUD-PyHEADTAIL suite. To best mimic the experimental conditions in which the instabilities were observed, we included in our simulation model:

- EC in the dipole magnets;
- EC in the quadrupole magnets;
- Chromaticity;

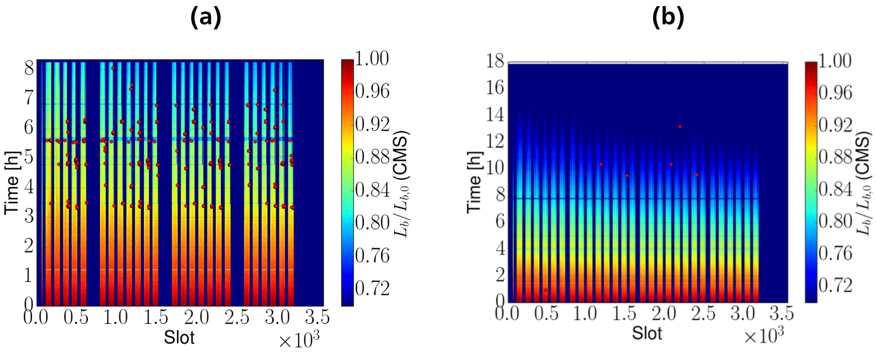

Figure 3.22.: Bunch-by-bunch luminosities from the CMS experiment normalized to the value measured at the beginning of stable beams. Instabilities are marked by red dots. Right: vertical chromaticity of both beams set at 15 units. Left: vertical chromaticity increased to 22 units in stable beams.

- Transverse amplitude detuning from octupoles,
- Bunch-by-bunch transverse feedback.

Firstly, we have identified the instability thresholds scanning the electron density in the dipoles for different bunch intensities. In the dipoles, the central cloud density has been scanned between $1 \cdot 10^{11} \mathrm{e}^-/\mathrm{m}^3$ and $22 \cdot 10^{11} \mathrm{e}^-/\mathrm{m}^3$ whereas, in the quadrupoles, the electron distribution has been loaded from an earlier dedicated buildup simulation for a maximum SEY of 1.3 and kept unchanged.

Figure 3.23 shows the results obtained for a bunch intensity of $0.7 \cdot 10^{11}$ppb. It is evident that the behavior in the two planes is strongly asymmetric. In fact, it can observed that the bunch becomes unstable only in the vertical plane. Such coherent motion, which leads to a strong emittance blow-up, cannot be damped by the transverse bunch-by-bunch feedback system because it excites high order intra-bunch modes [79], as shown in Fig. 3.23 (bottom). The study suggests that EC densities larger than $5 \cdot 10^{11} \mathrm{e}^-/\mathrm{m}^3$ are sufficient to drive vertical instabilities in spite of the presence of a fully functional transverse feedback, high chromaticity and high Landau octupole settings, consistently with previous simulation studies [73]. The simulations have been repeated for $1.0 \cdot 10^{11}$ ppb finding a very similar instability threshold in terms of initial electron density in the dipole.

Since the instability onset does not seem to be very sensitive to the bunch intensity for a given EC density, we have also investigated how the central electron density in the dipoles varies with the bunch intensity. Figure 3.24 shows the EC profiles estimated with PyECLOUD buildup simulations for selected bunch intensities.

In dipole regions, the electron motion is confined along the lines of the magnetic field. Electrons trapped by different magnetic field lines will receive a different kick from the beam resulting in the characteristic high density vertical stripes. The position and the number of these side stripes mainly depends on the beam current and on the position of the maximum impinging energy in the SEY curve. At bunch intensities above $1 \cdot 10^{11}$ ppb, like in the range between the present operational value and the one required by the HL-LHC upgrade ($1 \cdot 10^{11}$-$2.3 \cdot 10^{11}$ ppb), the LHC density within the chamber features a two-stripe structure and its density around the bunch is very low. Conversely, for lower bunch current a third stripe develops at the center of the chamber and the region around the beam position gets densely populated with electrons. This range of bunch intensities is usually reached due to the intensity decay while the beams collide in stable beams.

To check whether the LHC is responsible for the instability development, we compared the estimated central densities with the instability threshold. Figure 3.25 shows the electron density at the beam position for different SEY values in the dipole magnets. It can be observed that for an SEY of 1.4, when the bunch intensity decreases from $1.0 \cdot 10^{11}$ to $0.5 \cdot 10^{11}$ ppb, the central density increases until crossing the identified instability threshold (marked with a red line). This growth is significantly reduced at lower SEY. This reveals that, consistently with the machine observations, the conditioning of the beam screen due to the beam scrubbing can have a beneficial impact on the instability development. However, the beam stability can also be improved by increasing the chromaticity. In Fig. 3.25, the black dot shows the identified instability threshold for a bunch intensity of $1.0 \cdot 10^{11}$ ppb assuming $Q'_y = 22$, instead of 15 units, and a SEY of 1.4 in the dipole magnets. As a result, the instability threshold becomes higher but it can still be crossed at lower bunch currents. This beneficial impact of the chromaticity was observed also experimentally. In fact, as shown in Fig. 3.22, the chromaticity increase did not suppress completely the instability but it made it less severe and delayed it.

Finally, we compared the obtained simulation results with the experimental data for the same fill as in Fig 3.20. The plot on the top of Fig. 3.26 shows the bunch intensity evolution measured during the stable beams, while the plot on the bottom displays the evolution of the electron density at the beam position in a dipole chamber, as inferred from buildup simulations. The red line marks the identified instability threshold. It is clear that, when the beam intensity drops, the electron density at the beam position increases, reaching the threshold after several hours in stable beams. Thus, simulation results are shown to closely represent the experimental data. These results allowed not only to interpret the observed instability, but are particularly relevant also in the framework of the HL-LHC upgrade. In fact, they show that this instability mechanism, which is triggered only for relatively low bunch intensity, is not expected to become more critical after the foreseen two-fold increase of the bunch intensity.

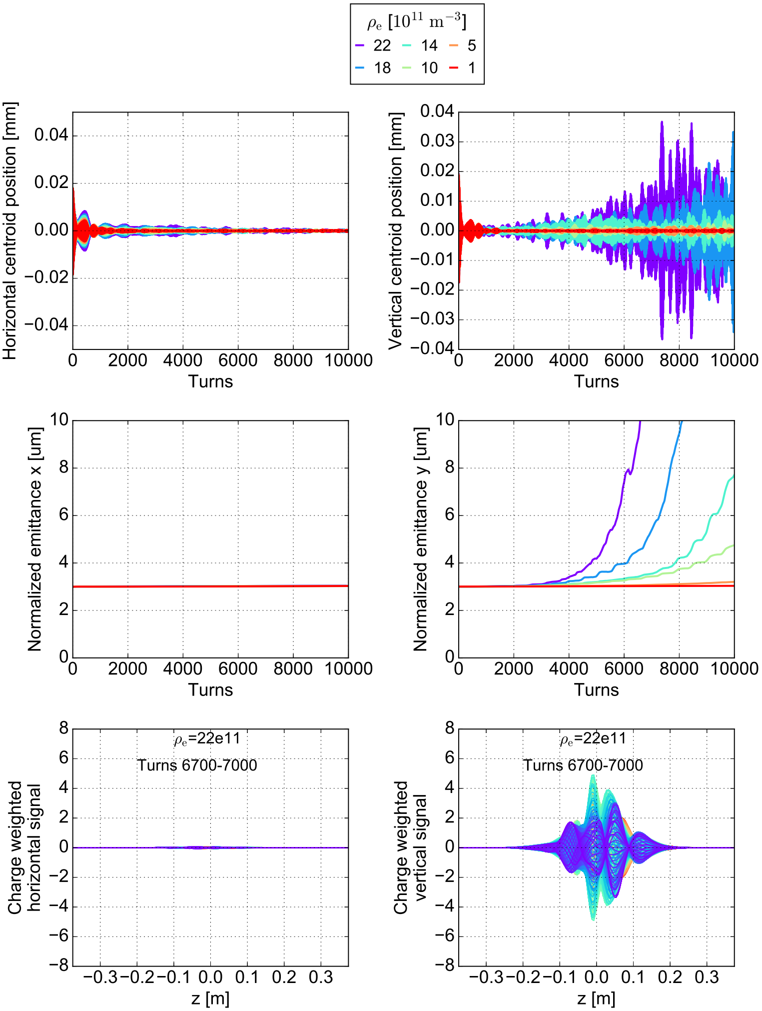

Figure 3.23.: Top: Evolution of the horizontal and vertical position of the bunch centroid. Middle: Evolution of the horizontal and vertical normalized emittance (results are shown for different central cloud densities in the dipoles as labeled). Bottom: Simulated intra-bunch oscillations in the horizontal and vertical plane for an EC density in the dipoles of $22 \cdot 10^{11} \mathrm{e}^-/\mathrm{m}^3$. The traces have been selected for 300 consecutive turns marked with different colors.

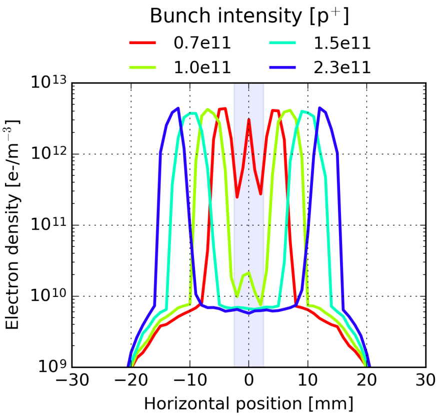

Figure 3.24.: Horizontal distribution of the electron density profile in a dipole chamber for selected bunch intensities. The blue rectangle refers to the electron density at a distance of ±2.5 m from the beam position (x=0).

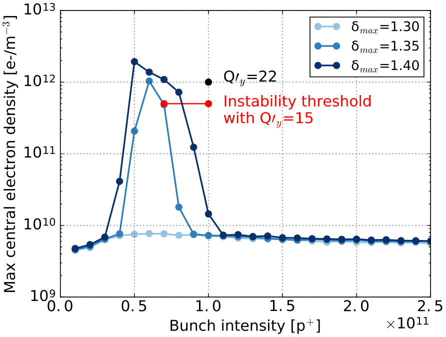

Figure 3.25.: Electron density estimated around the beam position (±2.5 mm) as a function of different bunch intensities. The red line shows the estimated instability as obtained from PyECLOUD-PyHEADTAIL simulations for Q'_y=15. For a bunch intensity of $1.1 \cdot 10^{11}$ the threshold has been estimated also for Q'_y=22 (black dot).The arrows indicate the bunch intensity at the beginning of the collisions for the LHC ($1.0 \cdot 10^{11}$ ppb) and for the HL-LHC ($2.2 \cdot 10^{11}$ ppb).

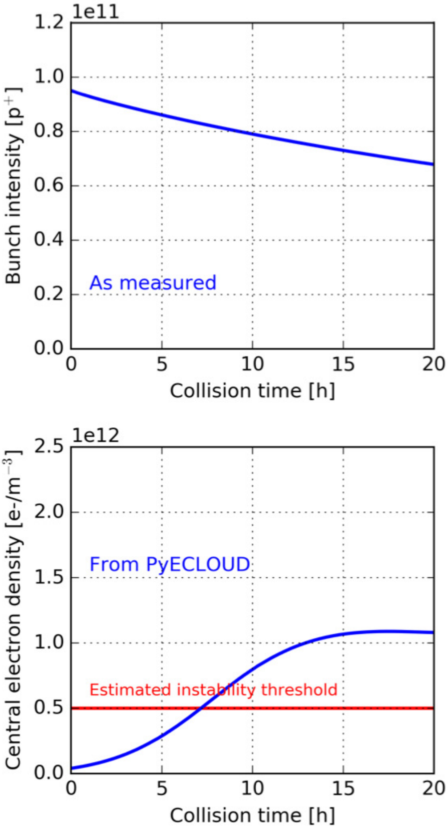

Figure 3.26.: Top picture: Measured bunch intensity during the stable beams. Bottom picture: Evolution of the central electron density in the LHC arc dipoles as inferred from buildup simulation. The SEY in dipoles is assumed equal to 1.4. The red line shows the instability threshold evaluated from PyECLOUD-PyHEADTAIL simulations.

3.3 EC studies for the LHC High Luminosity upgrade

In the framework of the HL-LHC project, simulation studies at injection energy have been carried out in order to evaluate the impact of the bunch intensity on the instability development. The range of bunch currents exploited goes from $0.6 \cdot 10^{11}$ to $2.4 \cdot 10^{11}$ ppb, where the nominal value is foreseen to be $2.3 \cdot 10^{11}$ ppb (i.e. twice the present LHC intensity). In these studies, we assume the same conditioning state as presently achieved in the LHC.

Based on the results presented in Sec. 3.1.2, we first studied the EC effects in the quadrupole magnets. Due to the sensitivity of the EC pinch dynamics to the initial EC phase space distribution, the simulations have been initialized with the EC distribution as produced by the PyECLOUD code per each bunch current. Figure 3.27 shows the EC density profiles for selected bunch intensities. We can note that for increasing bunch intensities, the electron density decreases significantly all over the chamber. This was found to be favorable also in terms of beam stability.

Figure 3.28 shows the evolution of the transverse position of the centroid of the bunch and of its normalized emittance for different bunch currents. We can therefore observe that the instability develops only for bunch intensity below $1.2 \cdot 10^{11}$ ppb. Thus, unlike the LHC case, the EC in the quadrupoles is not expected to drive instabilities at injection within the foreseen beam intensity upgrade.

Finally, in Fig. 3.29, we present also the simulation results for instabilities driven by EC in the dipole magnets. In these simulations, the bunch intensity is fixed at $2.2 \cdot 10^{11}$ ppb, while the central cloud density has been scanned between $1 \cdot 10^{11} \mathrm{e}^-/\mathrm{m}^3$ and $5 \cdot 10^{12} \mathrm{e}^-/\mathrm{m}^3$. We can note that fast instabilities occur only in the vertical plane for electron densities larger than $1 \cdot 10^{12} \mathrm{e}^-/\mathrm{m}^3$. Looking at Fig. 3.30, the estimated central density is well below the identified threshold and therefore no instability are expected to be triggered.

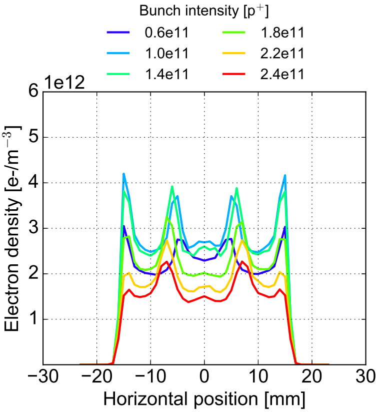

Figure 3.27.: Horizontal distribution of the electron density profile in a quadrupole chamber for selected bunch intensities and a maximum SEY of 1.3. The blue rectangle refers to the electron density at a distance of $\pm 2.5\ mm$ from the beam position.

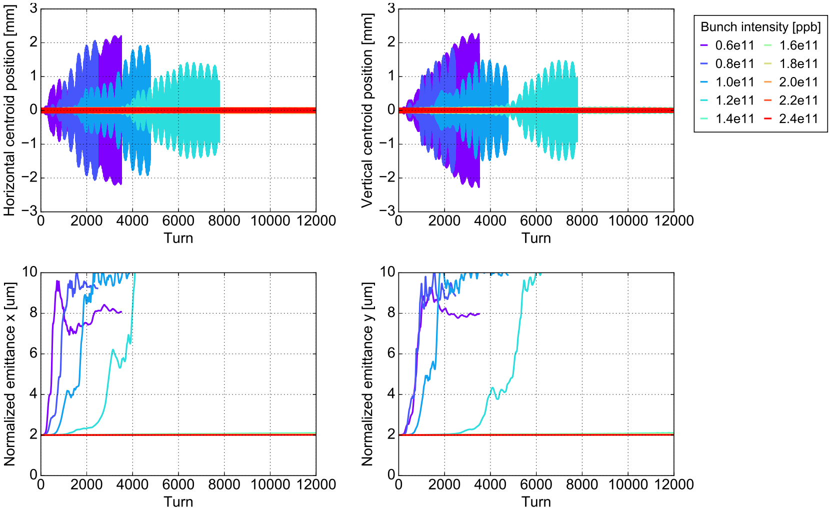

Figure 3.28.: Evolution of the horizontal and vertical position of the bunch centroid and of its transverse emittance for for different bunch currents in the quadrupole magnets. The realistic total length of quadrupoles has been assumed. No EC in the dipoles, no chromaticity, no current in the octupoles and transverse feedback system are included in the simulation setup.

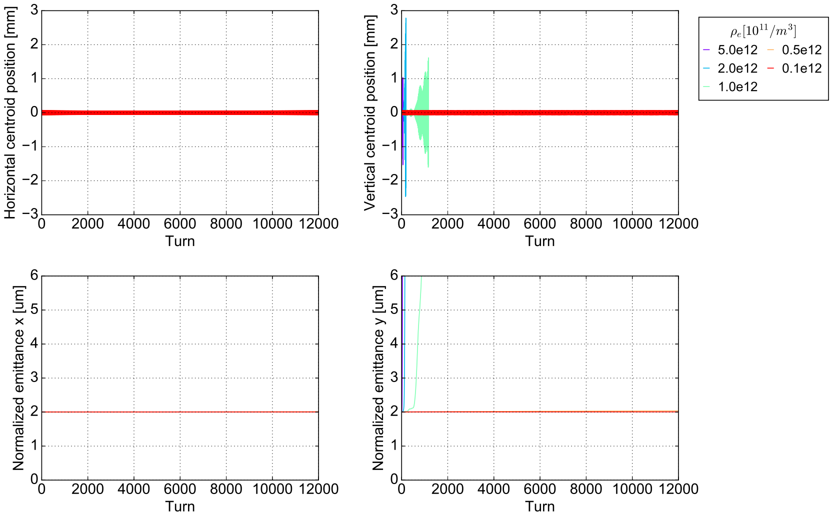

Figure 3.29.: Evolution of the horizontal and vertical position of the bunch centroid and of its transverse emittance for different initial EC densities in dipoles. No EC in the quadrupoles, no chromaticity, no current in the octupoles and no transverse feedback system are included in the simulation setup. The bunch intensity is fixed at $2.4 \cdot 10^{11}$ ppb. The instability develops entirely in the vertical and its threshold is found at around $1 \cdot 10^{12} \mathrm{e}^{-}/\mathrm{m}^{3}$.

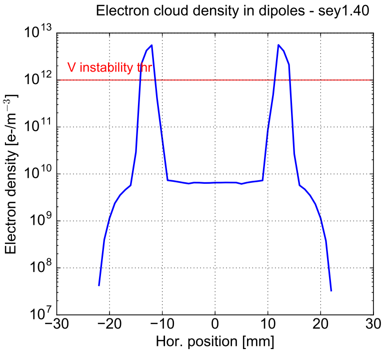

Figure 3.30.: Horizontal distribution of electron density in a dipole chamber estimated with the PyECLOUD buildup simulation for maximum SEY of 1.4. The red line shows the estimated density threshold as obtained from PyECLOUD-PyHEADTAIL.

4 Estimation of the incoherent tune spread from the EC

The interaction of localized electrons with a proton beam can be responsible not only for the development of coherent instabilities but also for the creation of incoherent effects that can potentially affect the beam quality. In fact, even if the electron density is not sufficient to drive the beam unstable, the pinched EC can create a large z-dependent tune spread along the bunch that may cause slow losses and emittance growth [80].

In the present chapter, we will present the simulated tune footprints due to the EC in different operational conditions. The impact on beam quality preservation will be also discussed, explaining in particular the origin of the incoherent losses observed at the LHC during the 2015 run.

4.1 Simulation setup

Unlike for the instability, a simplified model can be used to study the incoherent effects. Assuming that the beam distribution stays stationary, the forces due to the EC-bunch interaction at each interaction point can be calculated only once, during the first bunch passage through the EC, and then stored. On the following turns, the recorded forces are applied when the bunch returns to the same interaction point. As we are interested in the instantaneous tune footprint, the longitudinal motion is also frozen. Using a recorded EC pinch speeds up considerably the computation burden. Therefore these calculations are often made without resorting to parallel computing. Unless stated otherwise, the main simulation parameters used in these studies are listed in Tables 4.1 and 4.2.

In order to validate the developed simulation setup, we estimated analytically the small amplitude detuning due to the EC and compared the simulated detuning with the analytic result. Under the influence of the external linear focusing fields, the vertical single-particle motion is described by the so-called Hill's equation [49]:

$$y'' + K(s)y = 0 \tag{4.1}$$

Parameters	Symbol	Value	
		Injection	Collision
Beam energy [GeV]	E	450	6500
Bunch population [ppb]	N$_b$	1.1x10^{11}	1.0x10^{11}
Bunch spacing [ns]	s$_b$	25	
Rms beam size [μm]	$\sigma_{x,y}$	3.0	2.5
Rms bunch length [m]	$4\sigma_z$	0.09	0.075
Average beta function in the arcs [m]	$\beta_{x,y}$	92.7, 93.2	
Peak dipole field [T]	B	0.53	7.8
Quadrupole gradient in the arcs[T/m]		12.1	175
Chromaticities	$Q'_{x,y}$	15,15	
Octupoles current [A]	$\mathrm{I}_o ct$	26	471

Table 4.1.: LHC beam and machine parameters.

Parameters	Symbol	Value	
		Injection	Collision
# of macroelectrons for field calculation	Nel-field	$3{\cdot}10^6$	
# of macroelectrons for tracking	Nel-tr	$5{\cdot}10^3$	
# of macroprotons	Npr	$7{\cdot}10^5$	
# of slices	Nbin	150	
# of interaction point	nkick	15	

Table 4.2.: Numerical parameters used for the simulations.

where s is the position along the reference orbit and $K(s)$ is the strength of the quadrupole field component defined as:

$$K(s) = \frac{qg(s)}{m_0 \beta c \gamma} \tag{4.2}$$

where q is the charge of the particle, β the relativistic factor, c the speed of light and g the gradient of the quadrupole magnet.

The electric fields due to the EC can be considered as perturbations of the particle motion and thus it can be introduced on the right-hand side of Eq. 4.1 as:

$$y'' + Ky = \frac{qE_y}{m_0 \beta^2 c^2 \gamma} \tag{4.3}$$

In the first order (linear approximation) the vertical electric field E_y can be written as:

$$E_y = Gy \tag{4.4}$$

where:

$$G = \left.\frac{\mathrm{d}E_y}{\mathrm{d}y}\right|_{y=0} \tag{4.5}$$

and the equation of motion becomes:

$$y'' + (K_y + \Delta K^{EC})y = 0 \tag{4.6}$$

where:

$$\Delta K^{EC} = -\frac{qG}{m_0\beta^2c^2\gamma} \tag{4.7}$$

Therefore, the resulting tune shift is given by:

$$\Delta Q = \frac{1}{4\pi}\oint \Delta K^{EC}\beta(s)ds \tag{4.8}$$

Let us consider a test case in which the detuning from the EC in the LHC quadrupole magnets is computed both analytically and through the beam dynamics simulation. The PyECLOUD-PyHEADTAIL simulation has been initialized with a realistic EC distribution from a dedicated PyECLOUD buildup simulation, which has also been used to compute the electric field gradient used in the Eq. 4.8. To perform this calculation additinional diagnostics had to be implemented in the PyECLOUD code as explained in detaild in [81]. The obtained results, reported in Fig. 4.1, show a good agreement between the simulated detuning and the analytic estimation.

4.2 Tune footprints at LHC injection energy

Being strongly non-linear, the EC forces may induce different betatron frequencies of particles within the bunch which can lead to a large tune spread. The representation of the induced tune spread in the two-dimensional tune space (Q_x, Q_y) is usually called a "tune footprint". The tune footprint gives very important information on what resonances, showing whether particles can reach potentially dangerous resonant frequencies, which can induce beam degradation [49]. In particular, care must be taken to prevent the beam tune spread from crossing any low-order resonances for which the effect on the beam tends to be stronger.

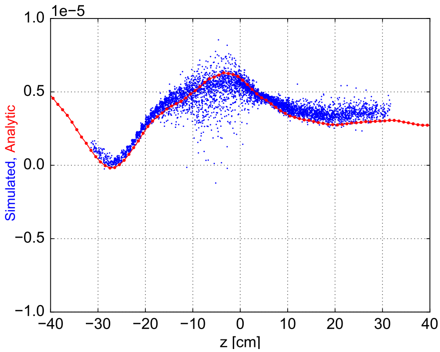

Figure 4.1.: Comparison between the vertical analytic and simulated detuning as a function of longitudinal position along the bunch (z).

In the following, we will discuss the tune footprint computed through PyECLOUD-PyHEADTAIL simulations at 450 GeV. Together with the tune spread generated by the EC, we have also investigated the effect of the chromaticity and octupole settings on the tune footprint. In fact, even if they are needed to ensure the beam stability (see Chapter 3), large values of chromaticity and octupole currents can produce a large tune spread which is difficult to accommodate in the space between the dangerous resonance lines in the tune diagram. The outcome of this study is shown in Figs. 4.2-4.6.

Figure 4.2-top shows the tune footprint computed for the dipole magnets assuming an initially uniform EC distribution in the dipole magnets, having a density of $1 \cdot 10^{12} \mathrm{e}^{-}/\mathrm{m}^{3}$. Particles are colored according to their longitudinal positions along the bunch. Blue corresponds to particles towards the tail while red are particles towards the head of the bunch. It can be observed that particles towards the tail of the bunch experience a larger tune shift predominantly in the vertical plane which results into an asymmetric footprint. This is clearly shown in the plots on the bottom. Here the horizontal and vertical detuning have been evaluated along the bunch as a function of the corresponding J_x and J_y, namely the betatron horizontal and vertical action variables [49]. The overall horizontal detuning is significantly smaller than the vertical as the presence of a dipolar magnetic field restricts the horizontal motion of the electrons.

Figure 4.3-left shows the corresponding electron density evolution in the $x-z$ plane at $y=0$. Electron stripes develop initially at the transverse bunch center and later shift outwards. Instead, in the vertical plane (see Fig. 4.3-right) the electrons pinch several times at the bunch position. These local density enhancements are

due to the non linearity of the EC force. Particles located at the z position for which the EC density is higher experience a larger detuning. It is worth noting that for every peak particles with smaller J_y have a larger detuning. Particles sitting at the bunch head experience the lowest tune deviation because the pinch has not yet started, while particles in the middle and at the tail of the bunch show a larger tune shift.

Figure 4.4 shows the tune footprint generated by the EC in the LHC quadrupole magnets. The simulation has been initialized using macroparticles coordinates and velocities imported directly from PyECLOUD buildup simulations. These were saved right before the bunch passage, with the EC in the saturation regime and for a maximum SEY of 1.3. The tune footprint as well as the evolution of the detuning along the bunch exhibit a similar shape in the two planes as the presence of quadrupole magnetic field is not expected to cause any strong asymmetry. Once again, the maximum detuning is reached at the EC pinch location.

Figures 4.5 and 4.6 show the tune footprints generated by the chromaticity alone, $Q'_{x,v}$ =15 units, and the octupole magnets alone powered with 26 A. The induced tune spread from the chromaticity is proportional to the particle momentum spread and it can be defined as:

$$\begin{aligned} \Delta Q_x &= Q'_x \delta, \\ \Delta Q_y &= Q'_y \delta \end{aligned} \tag{4.9}$$

where δ is relative momentum deviation with respect to the reference momentum.

Conversely, the forces provided by the octupole magnets depend on the transverse action of particles leading to the characteristic triangular shape of the tune footprint. The detuning with amplitude from the octupoles can be written as:

$$\begin{aligned} \Delta Q_x &= \alpha_{xx} J_x + \alpha_{xy} J_y, \\ \Delta Q_y &= \alpha_{yx} J_x + \alpha_{yy} J_y \end{aligned} \tag{4.10}$$

where α_{xx}, α_{xy}, α_{yx} and α_{yy} are the anharmonicity coefficients of the machine [82].

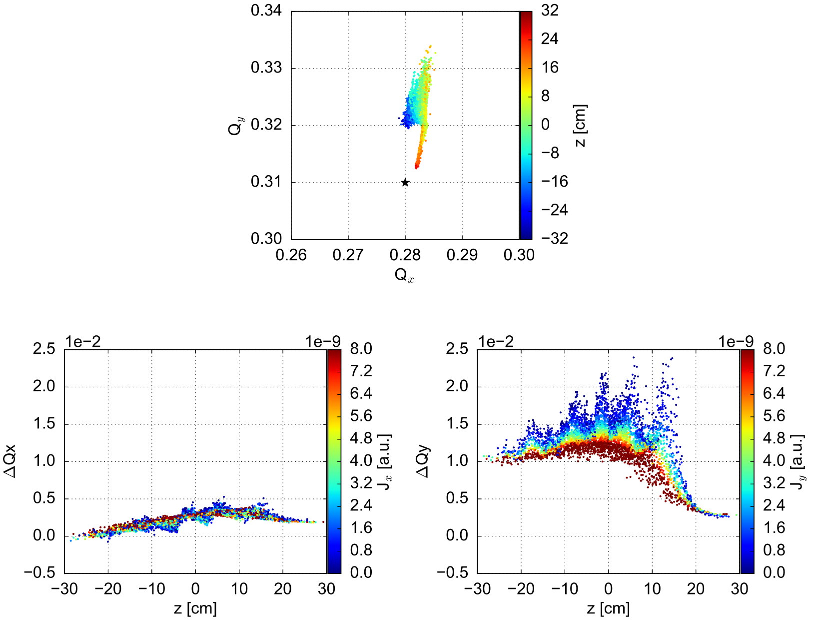

Figure 4.2.: Tune spread induced by the EC in the LHC dipole magnets. Top: tune footprint computed from an initially uniform electron distribution of $1 \cdot 10^{12}\mathrm{e}^{-}/\mathrm{m}^3$. The designed LHC tune at injection is marked by a black star. Bottom: horizontal (left) and vertical (right) detuning within the bunch as a function of the action variables J_x and J_y, respectively.

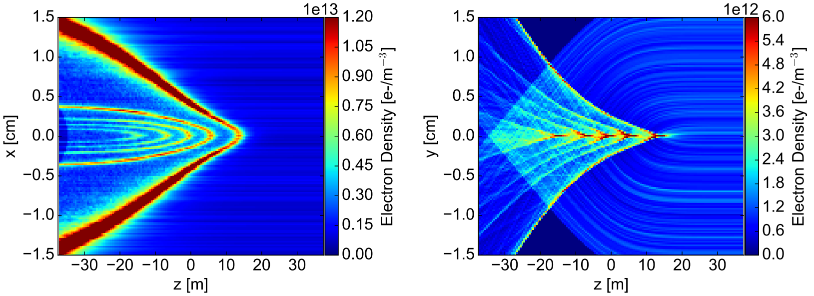

Figure 4.3.: Simulated electron density evolution in the $x - z$ plane at $y = 0$ (left) and in the $y - z$ plane at $x = 0$ (right) in a dipole magnet for an LHC bunch at 450 GeV.

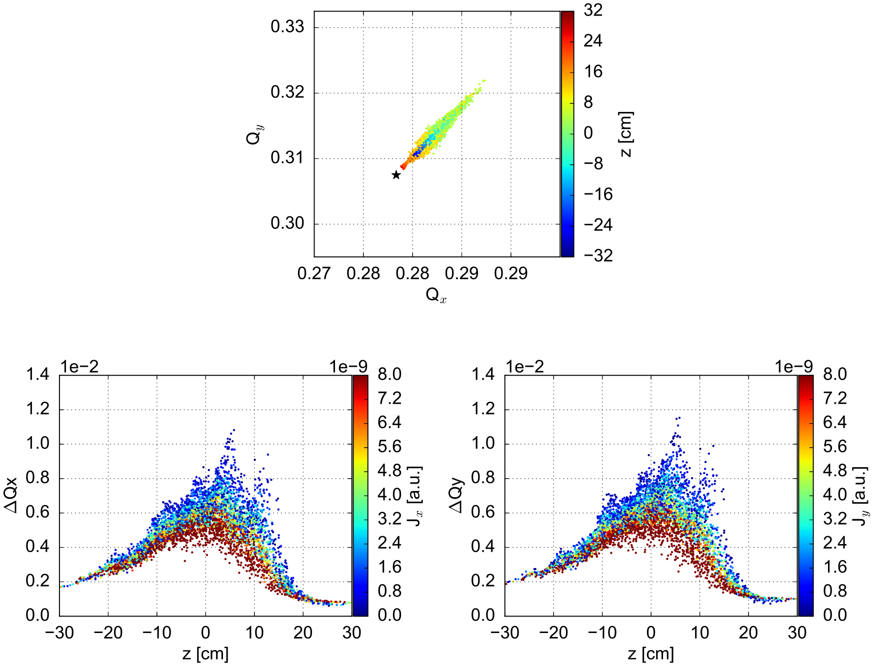

Figure 4.4.: Tune spread induced by the EC in the LHC quadrupole magnets. Top: tune footprint for a maximum SEY of 1.3 using the realistic macroparticles coordinates from a PyECLOUD buildup simulation. The designed LHC tune at injection is marked by a black star. Bottom: horizontal (left) and vertical (right) detuning within the bunch as a function of the action variables J_x and J_y, respectively.

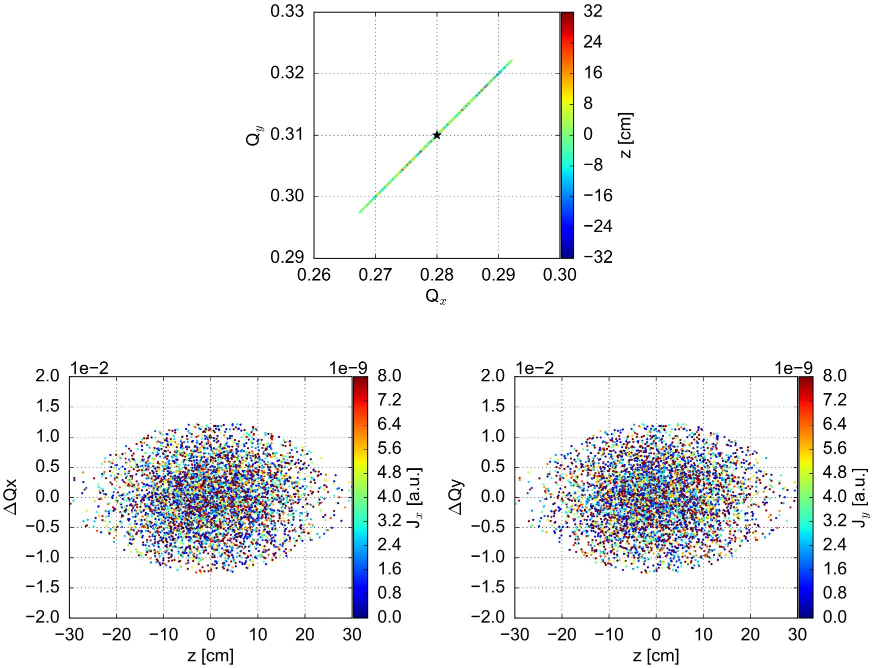

Figure 4.5.: Beam particles tune spread due to the chromaticity. Top: tune footprint generated by $Q'_{h,v}$=15. The LHC designed tune at injection is marked by a black star. Bottom: horizontal (left) and vertical (right) detuning within the bunch as a function of the action variables J_x and J_y, respectively.

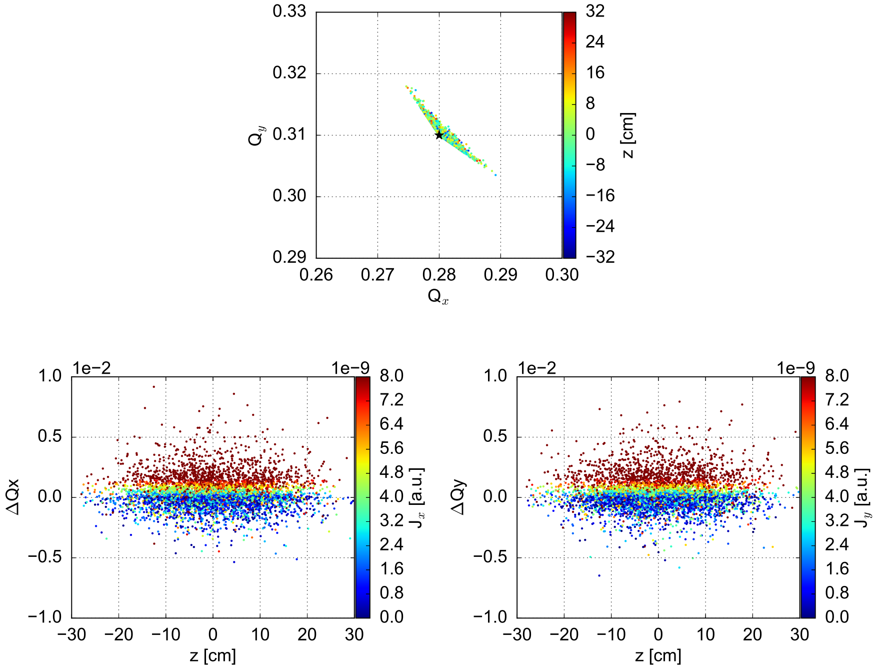

Figure 4.6.: Beam particles tune spread due to the octupoles. Top: tune footprint generated by a current of 26 A in the octupoles. The designed LHC tune at injection is marked by a black star. Bottom: horizontal (left) and vertical (right) detuning within the bunch as a function of the action variables J_x and J_y, respectively.

4.2.1 LHC observations and comparison against simulation results

As discussed in the previous chapter, in the presence of a strong EC, the beam stability can be only preserved with large chromaticity values and relatively high octupole currents. In mid 2015, at the early stages of the intensity ramp-up with 25 ns, it was noticed that, in order to achieve a good beam quality at injection energy, it was necessary to lower the vertical tune with respect to the designed value.

Figure 4.7a shows the measured beam lifetime as a function of the time while the vertical tune and chromaticity were changed to different values. A drop can be observed when the vertical chromaticity was increased from 10 to 15 units, then the lifetime could be recovered by lowering the vertical tune by $5 \cdot 10^{-3}$ units keeping the chromaticity at 15 units. Bunch-by-bunch intensity measurements (see Fig. 4.7b) show that the bunches which are most affected by the losses are those located at the tail of the trains, suggesting that they could be driven by the EC.

The need of operating with an optimized working point has been fully confirmed via numerical simulations [83, 84]. Figure 4.8 shows the tune footprints estimated for the LHC design fractional tunes (Q_x=0.28, Q_y=0.31) and for the tunes used operationally in 2016 (Q_x=0.27, Q_y=0.295). In both cases the tune spread has been computed assuming a chromaticity of 15 units in both planes, an octupole current of 26 A and the effect of the EC in dipole and quadrupole magnets. Thus, the optimized working point is needed to accommodate the large tune spread and avoid the third order resonance Q_y=.33 responsible for fast incoherent losses.

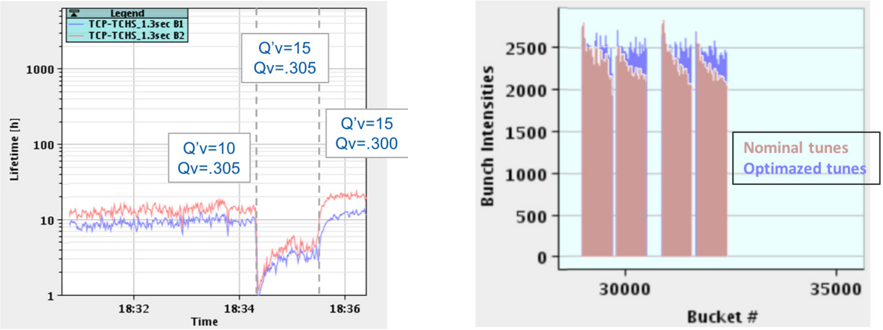

(a) Beam lifetime measurements

(b) Bunch intensity measurements

Figure 4.7.: Left: beams lifetime measured with 25 ns beams in the LHC at injection energy for different settings of vertical tune and chromaticity (Beam 1 is reported in blue and Beam 2 in red). Right: beam intensity measurements for the nominal LHC fractional tunes at injection ($Q_{x,y}$=0.28,0.31) and the optimazed ones ($Q_{x,y}$=0.27,0.295). In both cases $Q'_{h,v}$ was set to 15 units.

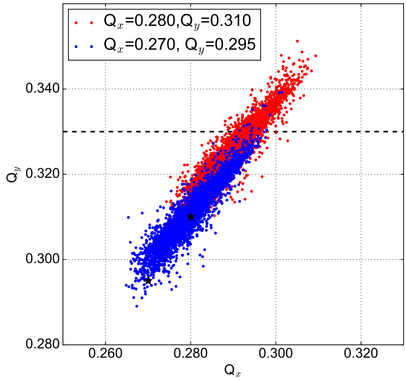

Figure 4.8.: Tune footprints evaluated for the LHC designed fractional tunes and for the tunes used operationally in 2016 including the effect of octupoles powered at 26 A, $Q'_{h,v}$ at 15 units, and EC in the dipole (ρ_e=$1 \cdot 10^{12}$e$^-$/m^3) and quadrupole magnets (SEY=1.3). The dashed line shows the third order resonance Q_y=0.33.

4.3 Tune footprints from the EC in the LHC insertion regions

The LHC experiments are hosted in the Insertion Regions (IRs) 1, 2, 5 and 8. In the following we will mainly refer to IR 1 and IR 5 which house the high luminosity experiments, namely ATLAS and CMS. The main feature of these regions, which are identical in terms of hardware and optics (except for the fact that the crossing-angle in IR 1 is in the vertical plane and in IR 5 is in the horizontal plane), is the small β-function at the Interaction Points (IPs) (e.g. during the 2016 run β^* $=0.4$ m). This allows achieving a small beam size and increase the luminosity.

These IRs are comprised of the following sections (see Fig. 4.9) [48]:

- A 31-m long superconducting low-β triplet assembly, so-named because provides the final focusing of the proton beams at the IPs. They consist of 3 quadrupole elements and 4 magnets (Q1, Q2a, Q2b, Q3) operated at a temperature of 1.9 K and providing a nominal gradient of 205 T/m. Here the two beams share a common beam pipe.
- A pair of separation/recombination dipoles. The D1 dipole located next the triplets has a single bore (the two beams share the same vacuum chamber), while the D2 dipoles has a double core.
- Four matching quadrupoles which match the beam optics in the insertion region to the arc's FODO lattice. The Q4 operates at a temperature of 4.5 K and yield a nominal gradient of 160 T/m, Q5 and Q6 operate at a temperature of 4.5 K and provide a nominal gradient of 200 T/m, and the Q7 operate at a temperature of 1.9 K and provides a nominal gradient of 200 T/m.

Figure 4.10 shows the beta functions and the reference orbit of Beam 1 around the IP1. Due to the peculiarities of the such optics, as the large beta functions and

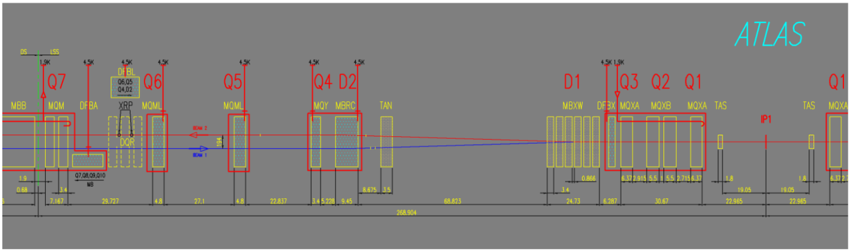

Figure 4.9.: Layout of the Insertion Region 1 (IR1), right side [9].

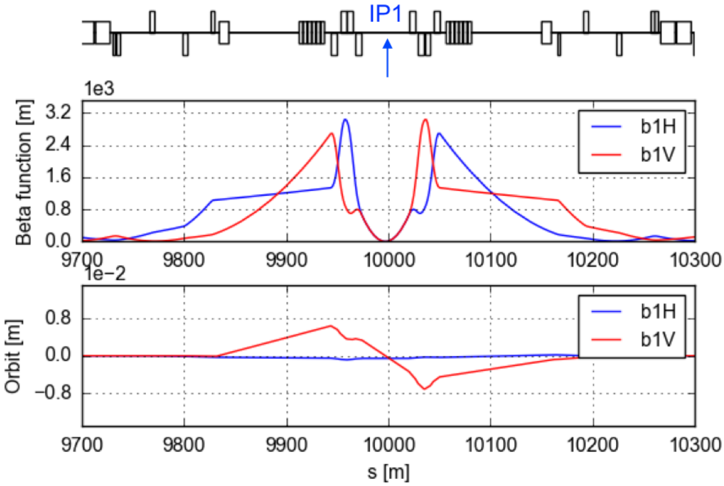

Figure 4.10.: Beam 1 optics at the Insertion Region 1 (IR1).

the off-centered orbit in the triplets, the impact on the detuning from EC in the IRs has been studied in detail. To that purpose, the realistic optics at β^*=40 cm has been included in the simulation setup and the EC-bunch interaction calculated at each quadrupole in the IR 1 and IR 5.

Figure 4.11 shows the tune footprints estimated for the effect of the EC in the triplets and in the matching quadrupoles separately assuming an LHC bunch at 6.5 TeV. Looking at the plots, it can be observed that the triplets have a lower effect on the tune spread compared to the matching quadrupoles, in spite of their much larger beta functions and magnet lengths. However, it is worth noting that in the triplets the beam is off-centered with respect to EC distribution, which is mainly concentrated around the center of the beam chamber (see Fig. 4.12a). This is not the case in the matching quadruples where the beam is centered on the pipe axis. In order to the explain the above-mentioned results, the detuning dependency from the crossing-angle and from the electron density in the chamber in the triplets has been therefore investigated.

Figure 4.12b shows the average detuning and the corresponding rms spread evaluated for different crossing-angle between 0 and 400 μrad (the real crossing-angle for the optics β^*=40 cm is about 200 μrad). The stronger detuning is observed with the centered beam as in the matching quadrupoles (i.e. 0 crossing-angle), whereas for large crossing-angle the tune footprint becomes very small.

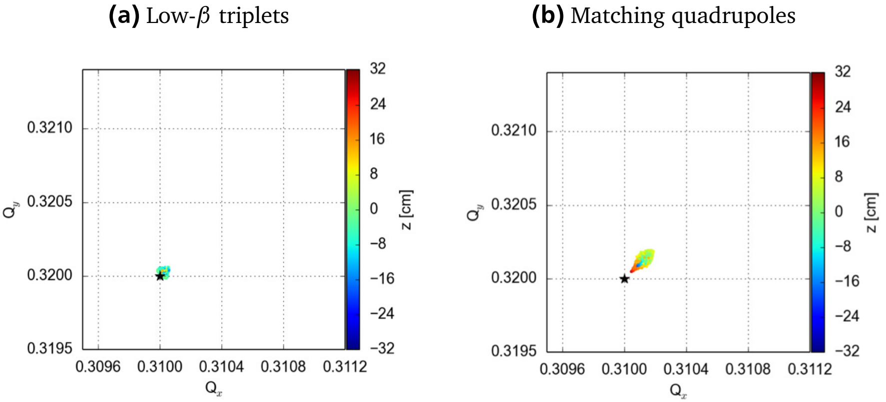

Figure 4.11.: Tune footprints due to the presence of the EC in the inner triplets and in the matching quadrupole magnets for a maximum SEY of 1.25. The color coding refers to the logitudinal position along the bunch (z). The designed LHC tune at injection is marked by a black star.

To have a measurable impact of the EC in the triplets on the general tune footprint, a much larger electron density is needed at the beam location. This is clearly shown in Fig.4.13. Here, the averaged detuning and the rms spread have been computed for different densities of the EC in the chamber obtained by adding a uniform electron distribution on top of the one naturally formed by the buildup process for a maximum SEY of 1.3. The additional EC density has been scanned between $4 \cdot 10^9 \mathrm{e}^-/\mathrm{m}^3$ and $4 \cdot 10^{14} \mathrm{e}^-/\mathrm{m}^3$. It can be observed that an electron density of about $4 \cdot 10^{13} \mathrm{e}^-/\mathrm{m}^3$ is needed to generate a visible tune shift, which is in the same order of magnitude of the density in the center of the chamber, as calculated from the buildup simulation.

(a) EC distribution from PyECLOUD

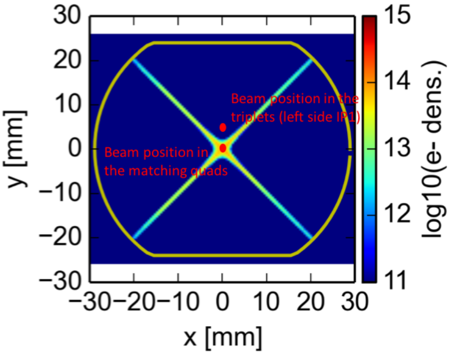

(b) Detuning versus crossing-angle

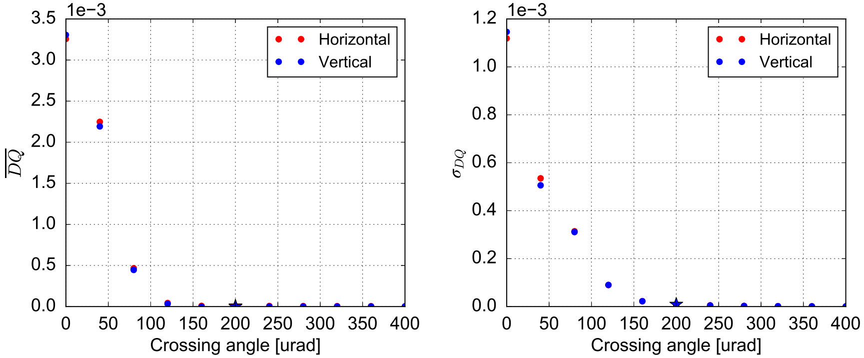

Figure 4.12.: Detuning dependency from the crossing angle in the inner triplets.Top: EC distribution from PyECLOUD buildup simulation assuming a maximum SEY of 1.3. The beam position within the chamber is also shown. Bottom: estimated average detuning and its rms spread evaluated for different crossing-angle in the triplets. The star indicates the realistic value of the crossing-angle for the optics β^*=40 cm.

(a) EC distribution
from PyECLOUD

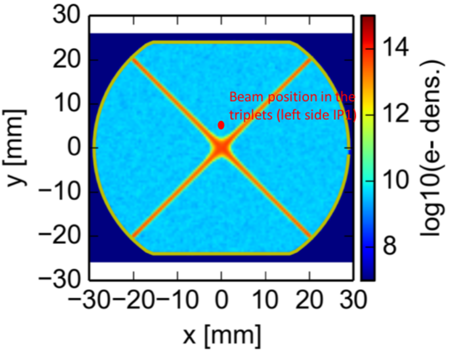

(b) Detuning versus EC density

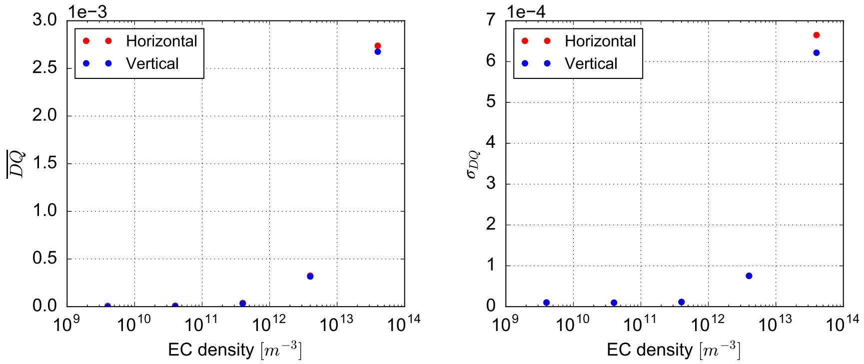

Figure 4.13.: Detuning dependency from the EC density uniformly distributed in the inner triplets. Top: EC distribution from PyECLOUD buildup simulation assuming a maximum SEY of 1.3 together with additional uniform EC density added on top of it. In this plot we refer to an EC density of $4 \cdot 10^{10}\mathrm{e}^{-}/\mathrm{m}^{3}$. The beam position within the chamber is also shown. Bottom: estimated average detuning and its rms spread evaluated for different EC density added on top of the realistic configuration.

Summary and conclusions

The EC has been identified as one of the major limiting factor for the 25 ns beams in the CERN SPS and LHC accelerators. In the present work, the formation of the EC and its impact on the beam dynamics have been studied by means of numerical simulations and experimental observations.

At the LHC EC effects have been observed for the first time during the Run 1 (2010-2012), becoming more and more severe when operating with tight bunch spacing of 25 ns at the beginning of the Run 2 (2015-2018).

In 2015, a strong heat load due to the EC has been observed in the cold sections of the LHC, with a significant impact on the operation of the cryogenic system. Inside the 1.9 K cold bore of the superconducting magnets, the induced thermal loads are intercepted by a perforated beam screen, held at an intermediate temperature of 5-20 K, for which only a limited cooling capacity is available. In order to preserve the superconducting state of the magnets, pumping slot shields (baffle plates) have been added on the outer side of the beam screen so that the electrons are intercepted before reaching the cold bore. In the framework of the design of the new superconducting magnets for HL-LHC insertion region, the question has been raised whether the electric shielding provided by the beam screen could be sufficient to prevent the multipacting even in absence of the baffle plates. This point has been addressed with detailed simulation studies using the PyECLOUD code. The effects of a single pumping slot has been studied by modeling the hole and the corresponding baffle with a T-shape boundary around the slot. Dealing with this geometry has required the implementation of new features in the simulation codes. The results showed that, in the absence of these shields, the multipacting could indeed occur on the cold bore, inducing a non-negligible heat load onto the 1.9 K surface. This suggested that shielding baffle behind the pumping slots should included also in the design of the new element for the HL-LHC insertion regions.

EC effects can also significantly influence the dynamics of the particle beam. The understanding of these phenomena heavily relies on numerical simulations performed with a recently developed interface that combines PyECLOUD with the PyHEADTAIL beam dynamics code. In order to be able to study the effects observed in the LHC, especially those which require long run spans (e.g. instabilities with rise time of the order of 10^4 turns), new advanced features had to be included in the codes and parallel computing resources had to be exploited.

Relying on these tools, an extensive simulation campaign has been carried out aiming at assessing the role of the EC in different LHC regions and at evaluating the threshold for the coherent instabilities as well as the incoherent tune spread. This allowed explaining the driving mechanism of several EC observations at the LHC during the 2015-2017 proton run and to find appropriate mitigation techniques.

In particular, PyECLOUD-PyHEADTAIL simulations showed that the EC in the LHC quadrupole magnets plays an important role in the dynamics of coherent instabilities at injection energy. In fact, even if these magnets cover only a small fraction of the LHC circumference (i.e. about 7%), due to the trapping effects from the quadrupole gradient, the electron density at the beam location can be very high,up to 10^{13} e^{-}/m^{3}. Our simulations showed that, in the absence of octupoles and chromaticity, the EC in the quadrupoles alone can drive coherent instabilities both in the horizontal and in the vertical plane. In simulation, the beam stability could only be restored using large chromaticity values, relatively high octupole currents together with the transverse feedback systems. These findings were found to be consistent with experimental observations during standard operation and dedicated test runs at the LHC. Differently from the injection energy case, instabilities due to the EC in the quadrupoles are not expected at 6.5 TeV as the increase of the particle energy results into a significantly increased beam rigidity.

The EC effects on the beam dynamics have been studied also for the LHC main dipole magnets. The results revealed that, in the present conditioning state of the machine, coherent instabilities from the EC in these elements alone are not expected to be triggered neither at injection nor at high energy. This is due to the fact that for the nominal intensity the two-stripe structure of the EC in the dipoles does not affect the beam dynamics, as the electron density at the beam location is very low. Conversely, for lower bunch currents, a third stripe develops at the center of the chamber resulting into an enhancement of the EC density seen by the bunch itself, which can render the beam unstable. These numerical predictions are shown to be in good agreement with the LHC observations. Indeed, they allow explaining the anomalous instability observed in the LHC in 2016, while the beams were kept stably for several hours in collision at 6.5 TeV.

The understanding of the limitations due to the EC effects is crucial not only for the present LHC runs but also in the perspective of the planned upgrade (HL-LHC) aiming at increasing the LHC intensity and luminosity. For this reason, first simulation studies have also been carried out for the HL-LHC scenarios. In this cases, the foreseen two-fold increase of the bunch intensity has been found to be favorable for beam stability.

Even when the beam remains transversely stable, the bunch-EC interaction can be source of beam quality degradation caused by incoherent effects. Being strongly non-linear, the EC forces can induce different betatron frequencies on different particles within the bunch, leading to a large tune spread, which can reach dangerous resonant frequencies. This is particularly worrying in storage rings and colliders as the aim is to store the beam for a very long time while preserving a good beam quality. For this reason, the tune footprint due to the EC has been estimated through PyECLOUD-PyHEADTAIL simulations in different operational conditions. It has been found that in the LHC high octupoles and chromaticity settings (required to avoid EC induced instabilities), together with the detuning induced by the EC itself, lead to a quite large tune footprint which could reach the third order resonance $Q_y = 0.33$. In order to avoid incoherent beam losses and improve the beam lifetime, the tunes of the machine had to be carefully optimazed. The identified need for operating with an optimized working point to better accommodate the large tune spread is fully consistent with experimental observations. Based on these results, optimal settings for the LHC fractional tunes have been found and used in operation for the 2016-2017 run.

At high energy the impact of the detuning from the EC has been mainly studied for the LHC inner triplets. Here the beams, which travel off-axis as they share the same vacuum pipe, are squeezed before colliding at the interaction point. In order to obtain the required small beam size, the β function has to be made very large in these particular magnets, i.e. up to 10^3 m. Parametric studies, made by scanning the crossing angle and the electron density in the chamber, pointed out that the extent of the tune footprint increases with lowering crossing angle, becoming maximum when the two beams are on-axis.

EC effects are also found to be a major concern for the SPS, in particular for the production of the high intensity beams foreseen by the LHC Injectors Upgrade project. While beam induced surface conditioning has proved successful for the production of the nominal LHC beams, the high intensity beams were found to still suffer from strong EC effects. Therefore, it was decided to apply an amorphous carbon coating to the critical components of the SPS ring by means of a newly developed *in-situ* technique called hollow cathode sputtering, in order to reduce the SEY of the chamber. The efficiency of the coating realized with this technique has been assessed through PyECLOUD buildup simulations for the MBA and MBB dipole magnets and for the QF quadrupole magnets. In order to reproduce the coating as achievable with the hollow cathode procedure, the beam chambers has been modeled including a non-uniform SEY profile. The results confirmed that, in the presence of the magnetic field, the partial coating of the chamber's profile fully suppresses the EC. Concerning the case in which the same chambers are used as drift sections (i.e. which is quite common in the SPS short straight sections), the EC can be fully suppressed only in the MBA and the QF-type chambers. Conversely, when the MBB profile is used as drift, multipacting would still occur due to the secondary electron emission from the uncoated vertical walls of the chamber.

However, even in this case, the effect is strongly mitigated compared to the bare StSt case.

A Sensitivity study

For the purpose of assessing the sensitivity to numerical parameters we have performed a convergence studies for a nominal LHC bunch at injection energy.

Firstly, we tested the sensitivity to the number of beam-EC Interaction Points (IPs) per turn. We assumed EC only in the quadrupoles using an electron distribution taken directly from a PyECLOUD buildup simulation. Figure A.1 shows the evolution of the horizontal and vertical position of the bunch and its emittance for different number of IPs. For the case with a single IP there is a clear evidence of a different behavior in the emittance growth, which becomes visible from the beginning of the simulation (see Fig.A.2). This feature disappears when increasing the number of IPs. In our simulations we have chosen 16 IPs.

Then, we have also investigated the impact of the number of MPs within the proton bunch. In this case, the EC has been localized only in the LHC main dipoles assuming an initial uniform density of $1.3 \cdot 10^{12} \mathrm{e}^{-}/\mathrm{m}^{3}$ (corresponding to $5 \cdot 10^{5}$ macroelectrons). In Fig. A.3 we show the evolution of the vertical position of the bunch and its emittance for different numbers of proton MPs. In the range of interest, a good convergence is reached.

Finally, for the same EC distribution in the dipoles, we tested the impact of the number of bunch slices. The number of MPs in the bunch is $7 \cdot 10^{5}$. The results are shown in Fig. A.4. Converge is seen above 50 slices.

In order to achieve a reasonable computational burden (in terms of time and resources), in all the simulations presented in this work we have used 16 IPs per turn, $7 \cdot 10^{5}$ MPs per bunch and 150 slices.

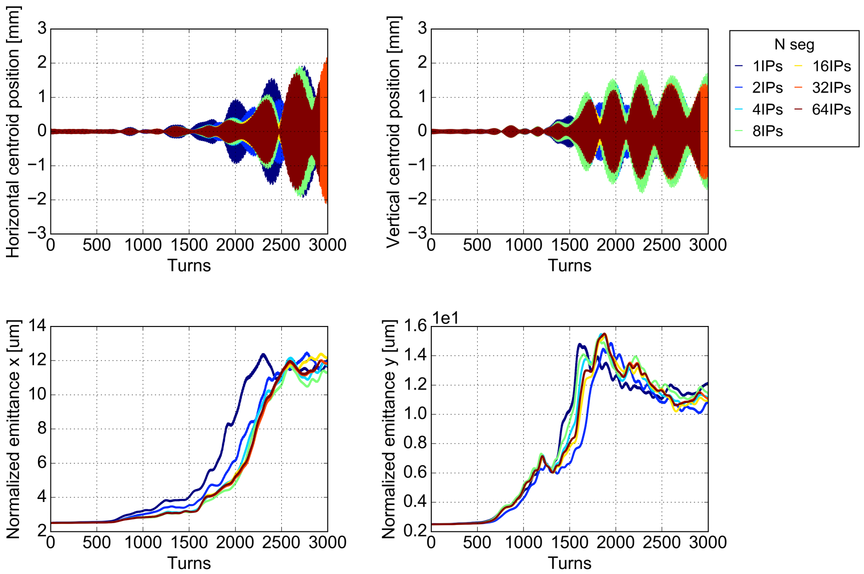

Figure A.1.: Evolution of the transverse position of the bunch and its emittance for different numbers of IPs.

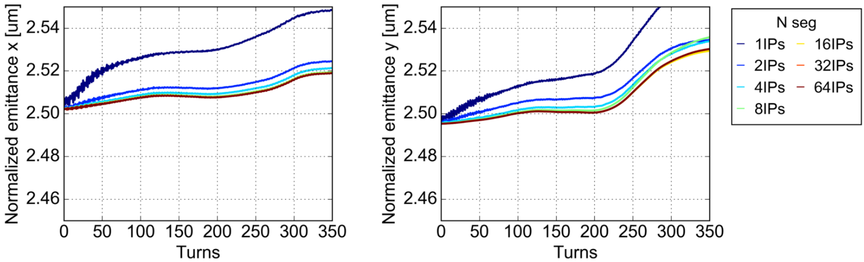

Figure A.2.: Zoom over 350 turns of the transverse emittance for different numbers of IPs.

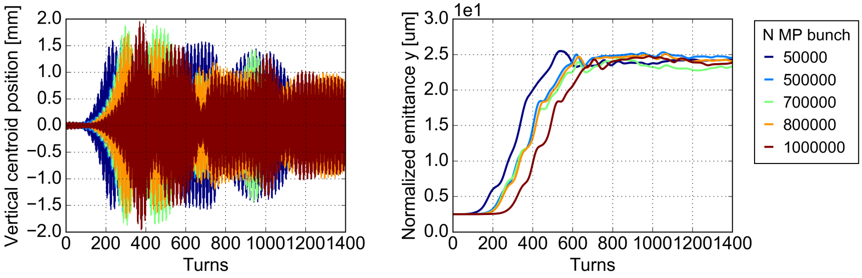

Figure A.3.: Evolution of the vertical position of the bunch and its emittance for different numbers of MPs in the bunch.

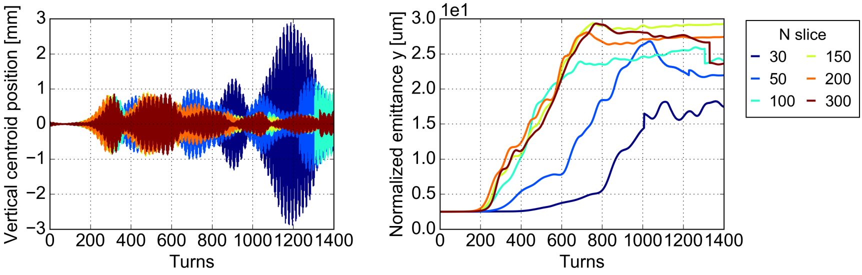

Figure A.4.: Evolution of the vertical position of the bunch and its emittance for different numbers of bunch slices.

List of Figures

List of Tables

Lists of Abbreviations

a-C amorphous-Carbon

ALICE A Large Ion Collider Experiment

ATLAS A Toroidal LHC ApparatuS

BCMS Batch Compression Merging and Splitting

BSRT Beam Synchrotron Radiation Telescope

CERN European Organization for Nuclear Research

CMS Compact Muon Solenoid

EC Electron Cloud

ECM Electron Cloud Monitor

FD Finite Difference

FFT Fast Fourier Transform

HL-LHC High Luminosity LHC

LHC Large Hadron Collider

LHCb Large Hadron Collider Beauty

LINAC2 LINear ACcelerator 2

LIU LHC Injectors Upgrade

LS1 Long Shutdown 1

LSS Long Straight Section

MB Main Bend

MP Macroparticle

MQ Main Quadrupole

PIC Particle In Cell

ppb Proton Per Bunch

PS Proton Synchrotron

PSB Proton Synchrotron Booster

QD Quadrupole Defocusing

QF Quadrupole Focusing

RF Radio Frequency

SEY Secondary Electron Yield

SPS Super Proton Synchrotron

SR Synchrotron Radiation

SSS Short Straight Section

StSt Stainless Steel

Bibliography

[1] L. Austin and H. Starke, “Ueber die Reflexion der Kathodenstrahlen und eine damit verbundene neue Erscheinung secundärer Emission,” *Annalen der Physik*, vol. 314, no. 10, pp. 271–292, 1902.

[2] E. Benedetto, D. Schulte, F. Zimmermann, and G. Rumolo, “Simulation study of electron cloud induced instabilities and emittance growth for the CERN Large Hadron Collider proton beam,” *Phys. Rev. ST Accel. Beams*, vol. 8, p. 124402, Dec 2005.

[3] W. Fischer, M. Blaskiewicz, J. M. Brennan, H. Huang, H.-C. Hseuh, V. Ptitsyn, T. Roser, P. Thieberger, D. Trbojevic, J. Wei, S. Y. Zhang, and U. Iriso, “Electron cloud observations and cures in the Relativistic Heavy Ion Collider,” *Phys. Rev. ST Accel. Beams*, vol. 11, p. 041002, Apr 2008.

[4] H. Maury Cuna, J. G. Contreras, and F. Zimmermann, “Simulations of electron-cloud heat load for the cold arcs of the CERN Large Hadron Collider and its high-luminosity upgrade scenarios,” *Phys. Rev. ST Accel. Beams*, vol. 15, p. 051001, 2012.

[5] F. Zimmermann, “Review of single bunch instabilities driven by an electron cloud,” *Phys. Rev. ST Accel. Beams*, vol. 7, p. 124801, 2004.

[6] M. Zobov, D. Alesini, A. Drago, A. Gallo, S. Guiducci, C. Milardi, A. Stella, S. De Santis, T. Demma, and P. Raimondi, “Operating experience with electron cloud clearing electrodes at DAFNE,” in *Proceedings, 5th Workshop on Electron-Cloud Effects (ECLOUD’12): La Biodola, Isola d’Elba, Italy, June 5-9, 2012*, 2013.

[7] G. Rumolo, F. Zimmermann, H. Fukuma, and K. Ohmi, “Electron cloud studies for KEKB,” in *Proceedings of the 2001 Particle Accelerator Conference (PACS2011): Chicago, U.S.A., June 18-22, 2001*, vol. 3, pp. 1889–1891 vol.3, 2001.

[8] G. Iadarola and G. Rumolo, “Electron cloud in the CERN accelerators (PS, SPS, LHC),” 2013.

[9] G. Iadarola, "Electron cloud studies for CERN particle accelerators and simulation code development," Mar 2014. Presented 23 05 2014.

[10] G. Peach, "Ionization of atoms and positive ions by electron and proton impact," *Journal of Physics B: Atomic and Molecular Physics*, vol. 4, no. 12, p. 1670, 1971.

[11] I. D. Kaganovich, E. Startsev, and R. C. Davidson, "Scaling and formulary of cross-sections for ion–atom impact ionization," *New Journal of Physics*, vol. 8, no. 11, p. 278, 2006.

[12] M. E. Rudd, Y.-K. Kim, D. H. Madison, and J. W. Gallagher, "Electron production in proton collisions: total cross sections," *Rev. Mod. Phys.*, vol. 57, pp. 965–994, Oct 1985.

[13] A. Hofmann, *The physics of synchrotron radiation*, vol. 20. Cambridge University Press, 2004.

[14] E. Willett, *The Basics of Quantum Physics: Understanding the Photoelectric Effect and Line Spectra*. The Library of Physics, Rosen Publishing Group, 2005.

[15] V. Baglin, I. R. Collins, and O. Grobner, "Photoelectron yield and photon reflectivity from candidate LHC vacuum chamber materials with implications to the vacuum chamber design," in *Proceedings of 6th European Particle Accelerator Conference (EPAC'98): Stockholm, Sweden, June 22-26, 1998*, pp. 2169–2171, 1998.

[16] N. Mahne, V. Baglin, I. R. Collins, A. Giglia, L. Pasquali, M. Pedio, S. Nannarone, and R. Cimino, "Photon reflectivity distributions from the LHC beam screen and their implications on the arc beam vacuum system," in *Proceedings of the European Vacuum Congress: 2nd National Conference of the German Vacuum Society and 8th European Vacuum Conference (EVC 2003) (EVC-8): Berlin, Germany, June 13-26 2003*, 2003.

[17] F. Zimmermann, "Electron cloud instability and beam induced multipacting in the LHC and in the VLHC," in *Proceedings: International Workshop on Multibunch Instabilities in Future Electron and Positron Accelerators (MBI97), Tsukuba, Japan, 15-18 Jul 1997*, pp. 221–233, 1997.

[18] R. Cimino, I. Collins, M. Furman, M. Pivi, F. Ruggiero, G. Rumolo, and F. Zimmermann, "Can low-energy electrons affect high-energy physics accelerators?," *Physical review letters*, vol. 93, no. 1, p. 014801, 2004.

[19] M. Furman, “Electron-cloud build-up: Theory and data,” *Lawrence Berkeley National Laboratory*, 2011.

[20] D. Halliday, R. Resnick, and J. Walker, *Fundamentals of Physics*. John Wiley & Sons, 2010.

[21] M. G. Billing, J. Conway, E. E. Cowan, J. A. Crittenden, W. Hartung, J. Lanzoni, Y. Li, C. S. Shill, J. P. Sikora, and K. G. Sonnad, “Measurement of electron trapping in the Cornell Electron Storage Ring,” *Phys. Rev. ST Accel. Beams*, vol. 18, p. 041001, Apr 2015.

[22] R. Cimino and T. Demma, “Electron cloud in accelerators,” *International Journal of Modern Physics A*, vol. 29, no. 17, p. 1430023, 2014.

[23] D. Alesini, A. Drago, A. Gallo, S. Guiducci, C. Milardi, A. Stella, M. Zobov, S. De Santis, T. Demma, and P. Raimondi, “DAϕNE Operation with Electron-Cloud-Clearing Electrodes,” *Phys. Rev. Lett.*, vol. 110, p. 124801. 6 p, Mar 2013.

[24] L. Wang, S. Kurokawa, H. Fukuma, S. S. Win, and A. Chao, “Solenoid effects on an electron cloud,” in *Proceedings of 31st ICFA Advanced Beam Dynamics Workshop (ECLOUD’04): Napa, USA, April 19-23, 2004*, 2004.

[25] G. Stupakov and M. Pivi, “Suppression of the effective secondary emission yield for a grooved metal surface,” in *Proceedings of 31st ICFA Advanced Beam Dynamics Workshop (ECLOUD’04): Napa, USA, April 19-23, 2004*, 2004.

[26] C. Y. Vallgren, G. Arduini, J. Bauche, S. Calatroni, P. Chiggiato, K. Cornelis, P. C. Pinto, B. Henrist, E. Métral, H. Neupert, *et al.*, “Amorphous carbon coatings for the mitigation of electron cloud in the CERN Super Proton Synchrotron,” *Physical Review Special Topics-Accelerators and Beams*, vol. 14, no. 7, p. 071001, 2011.

[27] R. Larciprete, D. R. Grosso, M. Commisso, R. Flammini, and R. Cimino, “Secondary electron yield of Cu technical surfaces: Dependence on electron irradiation,” *Phys. Rev. ST Accel. Beams*, vol. 16, p. 011002, Jan 2013.

[28] R. Cimino, M. Commisso, D. R. Grosso, T. Demma, V. Baglin, R. Flammini, and R. Larciprete, “Nature of the Decrease of the Secondary-Electron Yield by Electron Bombardment and its Energy Dependence,” *Phys. Rev. Lett.*, vol. 109, p. 064801, Aug 2012.

[29] G. Iadarola, H. Bartosik, K. Li, L. Mether, A. Romano, G. Rumolo, and M. Schenk, "Performance limitation from electron cloud in 2015," in *Proceedings of 6 th Evian Workshop on LHC beam operation: Evian Les Bains, France, December 15-17, 2015*, pp. 101–110, CERN, 2015.

[30] S. Berg, "Energy gain in an electron cloud during the passage of a bunch," tech. rep., CERN-LHC-Project-Note-97, 1997.

[31] K. Ohmi and F. Zimmermann, "Head-Tail Instability Caused by Electron Clouds in Positron Storage Rings," *Phys. Rev. Lett.*, vol. 85, pp. 3821–3824, Oct 2000.

[32] G. Rumolo, F. Ruggiero, and F. Zimmermann, "Erratum: Simulation of the electron-cloud build up and its consequences on heat load, beam stability, and diagnostics[phys. rev. st accel. beams 4, 012801 (2001)]," *Phys. Rev. ST Accel. Beams*, vol. 4, p. 029901, Feb 2001.

[33] E. Benedetto, "Emittance growth induced by electron cloud in proton storage rings," CERN-THESIS-2008-096 (2006).

[34] G. Franchetti, I. Hofmann, W. Fischer, and F. Zimmermann, "Incoherent effect of space charge and electron cloud," *Phys. Rev. ST Accel. Beams*, vol. 12, p. 124401, Dec 2009.

[35] L. Tavian, "Performance limitations of the LHC cryogenics: 2012 review and 2015 outlook," in *Proceedings, 4th Evian Workshop on LHC beam operation: Evian Les Bains, France, December 17-20, 2012*, (Geneva), pp. 129–138, CERN, CERN, 2012.

[36] G. Iadarola, E. Belli, K. Li, L. Mether, A. Romano, and G. Rumolo, "Evolution of Python Tools for the Simulation of Electron Cloud Effects," in *Proceedings of 8th International Particle Accelerator Conference (IPAC'17): Copenhagen, Denmark, 14-19 May, 2017*, (Geneva, Switzerland), pp. 3803–3806, JACoW, May 2017.

[37] G. Rumolo and F. Zimmermann, "Practical user guide for HEADTAIL," 2002. CERN-SL-Note-2002-036-AP.

[38] G. Iadarola, "PyHEADTAIL-PyECLOUD development," in *presentation at the Electron Cloud meeting, 27 May 2015, CERN, Geneva*.

[39] G. H. Shortley and R. Weller, "The numerical solution of Laplace's equation," *Journal of Applied Physics*, vol. 9, no. 5, pp. 334–348, 1938.

[40] J.-L. Vay, P. Colella, J. Kwan, P. McCorquodale, D. Serafini, A. Friedman, D. Grote, G. Westenskow, J.-C. Adam, A. Heron, *et al.*, “Application of adaptive mesh refinement to particle-in-cell simulations of plasmas and beams,” *Physics of Plasmas*, vol. 11, no. 5, pp. 2928–2934, 2004.

[41] E. Belli, “Multigrid solver in PyPIC,” in *presentation at the Electron Cloud meeting, 2 September 2016, CERN, Geneva*.

[42] K. Li, H. Bartosik, S. Hegglin, G. Iadarola, A. Oeftiger, A. Passarelli, A. Romano, G. Rumolo, and M. Schenk, “Code development for collective effects,” in *57th ICFA Advanced Beam Dynamics Workshop on High-Intensity and High-Brightness Hadron Beams (HB’16): Malmö, Sweden, July 3-8, 2016*, pp. 362–367, JACOW, Geneva, Switzerland, 2016.

[43] M. Benedikt, G. Clark, F. Pedersen, E. Blackmore, M. Barnes, U. Raich, J. Riunaud, S. R. Koscielniak, G. Cyvoct, K. Metzmacher, *et al.*, “The PS complex produces the nominal LHC beam,” tech. rep., 2000.

[44] R. Bruce and et all., “LHC Run 2: Results and challenges,” in *Proceedings, 57th ICFA Advanced Beam Dynamics Workshop on High-Intensity and High-Brightness Hadron Beams (HB2016): Malmö, Sweden, July 3-8, 2016*, p. MOAM5P50, 2016.

[45] W. Herr and B. Muratori, *Concept of luminosity*. Yellow Report CERN 2006-002, 2006.

[46] G. Apollinari, I. Béjar Alonso, O. Brüning, P. Fessia, M. Lamont, L. Rossi, and L. Tavian, *High-Luminosity Large Hadron Collider (HL-LHC): Technical Design Report V. 0.1*. CERN Yellow Reports: Monographs, Geneva: CERN, 2017.

[47] K. Hanke *et al.*, “The LHC Injectors Upgrade (LIU) Project at CERN: Proton Injector Chain,” in *Proceedings, 8th International Particle Accelerator Conference (IPAC 2017): Copenhagen, Denmark, May 14-19, 2017*, p. WEPVA036, 2017.

[48] O. S. Brüning, P. Collier, P. Lebrun, S. Myers, R. Ostojic, J. Poole, and P. Proudlock, *LHC Design Report*. CERN Yellow Reports: Monographs, Geneva: CERN, 2004.

[49] K. Wille, *The Physics of Particle Accelerators: An Introduction*. Oxford University Press, 2000.

[50] A. Ijspeert, M. Karppinen, and J. Salminen, “Design of corrector magnets for the LHC,” tech. rep., CERN, 1999.

[51] G. Rumolo and et al., “Protons: Baseline and alternatives, studies plan,” *CERN Yellow Reports*, vol. 2, no. 00, p. 166, 2016.

[52] “https://ecloudwg.web.cern.ch/.” Website of the Electron Cloud Working Group.

[53] P. Cruikshank and et all., “Mechanical design aspects of the LHC beam screen,” in *Proceedings of 17th Particle Accelerator Conference (PAC 97): Vancouver, Canada, May 12-16, 1997*, vol. 3, pp. 3586–3588, IEEE, 1997.

[54] O. Malyshev, “The capture factor and pumping speed for slots in the LHC beam screen with buffles.,” tech. rep., 2000. Vacuum Technical Note 00-17.

[55] V. Anashin, R. Dostovalov, and A. Krasnov, “The vacuum studies for LHC beam screen with carbon fiber cryosorber,”

[56] J. Foley, *Computer Graphics: Principles and Practice*. Addison-Wesley systems programming series, Addison-Wesley, 1996.

[57] K. Arduini, G.and Cornelis, W. Hofle, G. Rumolo, and F. Zimmermann, “The electron cloud instability of the LHC beam in the CERN SPS,” in *Proceedings of the Particle Accelerator Conference 2003 (PAC 2003): Portland, Oregon, May 12-16, 2003*, vol. 5, pp. 3038–3040, IEEE, 2003.

[58] G. Iadarola and et all., “Detailed Studies of Beam Induced Scrubbing in the CERN-SPS,” in *Proceedings of 6th International Particle Accelerator Conference (IPAC’15): Richmond, USA, May 3–8, 2015*, (Geneva, Switzerland), JACoW, May 2015.

[59] G. Iadarola and G. Rumolo, “Electron cloud in the CERN accelerators (PS, SPS, LHC),” 2013.

[60] G. Iadarola and A. Romano, “Simulation of multipacting thresholds,” in *presentation at the SPS Scrubbing Review, 8-9 September 2015, CERN, Geneva*.

[61] K. Li, H. Bartosik, B. Goddard, G. Iadarola, L. Mether, A. Romano, G. Rumolo, and M. Schenk, “Simulation of instability thresholds,” in *presentation at the SPS Scrubbing Review, 8-9 September 2015, CERN, Geneva*.

[62] G. Arduini *et al.*, “Measurement of the electron cloud properties by means of a multi-strip detector in the CERN SPS,” in *Proceedings of 8th European Particle Accelerator Conference (EPAC 2002): Paris, France, June 3-7, 2002*, pp. 1437–1439, 2002.

[63] A. Romano, G. Iadarola, and G. Rumolo, “News on EC calculations,” in *presentation at the Electron Cloud meeting, 16 May 2014, CERN, Geneva*.

[64] A. Romano, “Simulation and experimental studies on electron cloud effects in particle accelerators,” 2014. CERN-THESIS-2014-286.

[65] M. Taborelli, P. Chiggiato, P. Costa Pinto, and P. Cruikshank, “Nine years of carbon coating development for the SPS upgrade: achievements and heritage.,” Dec 2015. CERN-ACC-2016-0010.

[66] M. Van Gompel, P. Chiggiato, P. Costa Pinto, P. Cruikshank, C. Pasquino, J. Perez Espinos, A. Sapountzis, M. Taborelli, and W. Vollenberg, “Amorphous Carbon Thin Film Coating of the SPS Beamline: Evaluation of the First Coating Implementation,” in *Proceedings, 8th International Particle Accelerator Conference (IPAC 2017): Copenhagen, Denmark, May 14-19, 2017*, p. MOOCA3, 2017.

[67] P. Costa Pinto, T. Basso, A. Bellunato, P. Edwards, M. Mensi, A. Sublet, and M. Taborelli, “Implementation of Carbon Thin Film Coatings in the Super Proton Synchrotron (SPS) for Electron Cloud Mitigation,” in *Proceedings, 5th International Particle Accelerator Conference (IPAC 2014): Dresden, Germany, June 15-20, 2014*, p. WEPRI043, 2014.

[68] G. Rumolo and F. Zimmermann, “Theory and simulation of the electron cloud instability,” in *Proceedings, 11th Workshop, Chamonix, France, January 15-19, 2001*, pp. 166–175, 2001.

[69] J. F. Esteban Müller, P. Baudrenghien, T. Mastoridis, E. Shaposhnikova, and D. Valuch, “High-accuracy diagnostic tool for electron cloud observation in the LHC based on synchronous phase measurements,” *Phys. Rev. ST Accel. Beams*, vol. 18, p. 112801, Nov 2015.

[70] H. Bartosik, W. Hofle, G. Iadarola, Y. Papaphilippou, and G. Rumolo, “Benchmarking headtail with electron cloud instabilities observed in the LHC,” in *Proceedings of 5th Workshop on Electron-Cloud Effects (ECLOUD’12): La Biodola, Isola d’Elba, Italy, June 5-9, 2012*, pp. 211–217, 2013.

[71] W. Höfle, “Transverse damper,” in *Proceedings, Chamonix 2012 Workshop on LHC Performance, Chamonix, France, February 6-10, 2012*, pp. pp.157–162, 2012.

[72] G. Iadarola, A. Axford, H. Bartosik, K. Li, and G. Rumolo, “Effect of Electron Cloud in Quadrupoles on Beam Instability,” in *Proceedings of 6th International*

Particle Accelerator Conference (IPAC'15): Richmond, USA, May 3–8, 2015, (Geneva, Switzerland), JACoW, May 2015.

[73] K. Li and G. Rumolo, "Mitigation of Electron Cloud Instabilities in the LHC using Sextupoles and Octupoles," in *Proceedings of 3rd International Particle Accelerator Conference (IPAC'12): New Orleans, USA, 20-25 May, 2012*, (Geneva, Switzerland), JACoW, May 2012.

[74] P. Dijkstal, "Electron cloud buildup studies for the LHC," 2017. CERN-THESIS-2017-180.

[75] A. W. Chao, *Physics of collective beam instabilities in high energy accelerators*. Wiley, 1993.

[76] A. Romano, O. Boine-Frankenheim, X. Buffat, I. Iadarola, and G. Rumolo, "Electron cloud buildup driving spontaneous vertical instabilities of stored beams in the LHC," 2018. Manuscript submitted for publication.

[77] G. Rumolo and F. Zimmermann, "Electron cloud simulations: beam instabilities and wakefields," *Phys. Rev. ST Accel. Beams*, vol. 5, p. 121002, Dec 2002.

[78] J. Wenninger, "Approaching the Nominal Performance at the LHC," in *Proceedings of 8th International Particle Accelerator Conference (IPAC'17): Copenhagen, Denmark, 14-19 May, 2017*, (Geneva, Switzerland), pp. 13–18, JACoW, May 2017.

[79] A. Romano, G. Iadarola, K. Li, and G. Rumolo, "Macroparticle Simulation Studies of the LHC Beam Dynamics in the Presence of Electron Cloud," in *Proceedings of 8th International Particle Accelerator Conference (IPAC'17): Copenhagen, Denmark, 14-19 May, 2017*, (Geneva, Switzerland), pp. 2081–2084, JACoW, May 2017.

[80] E. Benedetto, G. Franchetti, and F. Zimmermann, "Incoherent Effects of Electron Clouds in Proton Storage Rings," *Phys. Rev. Lett.*, vol. 97, p. 034801, Jul 2006.

[81] A. Romano, G. Iadarola, and G. Rumolo, "Update on high energy tune footprint studies," in *presentation at the Electron Cloud meeting, 3 June 2015, CERN, Geneva*.

[82] J. Gareyte, J. P. Koutchouk, and F. Ruggiero, "Landau damping, dynamic aperture and octupoles in LHC," 1997. CERN-LHC-PROJECT-REPORT-09.

[83] A. Romano, G. Iadarola, and G. Rumolo, “Effect of the e-cloud on the tune footprint at 450 GeV,” in *presentation at the LHC Beam Operation Cpmmittee meeting, 27 October 2015, CERN, Geneva*.

[84] G. Arduini *et al.*, “High luminosity lhc: challenges and plans,” *Journal of Instrumentation*, vol. 11, no. 12, p. C12081, 2016.

Acknowledgments

These past years of PhD work have been intense and characterized by an important personal and professional growth. In these lines I would like to thank all the people who walked with me through this path.

First of all I want to express my sincere gratitude to my CERN supervisor and thesis director Dr. Giovanni Iadarola. His enthusiasm was always accompanying me during the work, motivating me to do my best. He has been a constant and reliable reference point on which I could always rely on. I warmly thank Gianni, not only for his concrete contribution to this work but also for having supported me in the difficult moments. Thank you!

I would like to address a special thank to Dr. Giovanni Rumolo for believing in me and for giving me the possibility to join the amazing e-cloud team. I also thank him for the valuable advice and the fruitful discussions which shed light on several results presented in this work.

I would like to thank Prof. Oliver Boine-Frankenheim for supervising me during all the years of my PhD activity and for giving me the possibility to join the TEMF community.

I wish to express my gratitude to the e-cloud team, Lotta, Kevin, Hannes, Michael and Eleonora and all my colleagues, in particular my HSC section, for having shared with me ideas and experience. Thanks for having made the work more fun.

Debora, Luca, Mario B., Andrea, Vera, Claudia, Alessia, Alessandro, Domenico, Giordana, Giorgia, Vanessa, Ernesto and Francesca deserve a big thank for their constant support and help. I know sometimes work may seem just like a job, but you guys helped to make this an unforgettable experience and for that I will be forever grateful! E poi c'è lei, che anche se è dall'altra parte del mondo è sempre stata presente .... Grazie Letì!

Infine vorrei ringraziare i miei genitori, mio fratello ed ovviamente Mario per avermi accompagnata in questo percorso (non sempre facile!). Grazie per essere stati sempre al fianco. Questa conquista è anche merito vostro!

AD MAIORA!

Annalisa Romano

Education

2015 - Present	**Ph.D. student at the Institute for Theory of Electromagnetic Fields (TEMF)**, *Technical University Darmstadt (Darmstadt, Germany).* **Thesis title:** *Electron cloud formation in the CERN particle accelerators and its impact on beam dynamics.* **Award:** *EPS-AG best student poster prize at the International Particle Accelerator Conference (IPAC) 2017.*
2011- 2014	**Master's degree in Energy Engineering**, *University of Sannio (Benevento, Italy).* **Thesis title:** *Simulation and experimental studies on electron cloud effects in particle accelerators.*
2007 - 2011	**Bachelor's degree in Energy Engineering**, *University of Sannio (Benevento, Italy).* **Thesis title:** *Methodologies for the integration of a small-scale wind farm in a smart grid*

Experience

Mar 2015 to Feb 2018	**Doctoral student at CERN**, *(Geneva, Switzerland).* **Thesis directors:** *Prof. Dr. rer. nat. Oliver Boine-Frankenheim and Dr. Giovanni Iadarola.*
Mar 2014 - Mar 2015	**Technical Student at CERN for master thesis project**, *(Geneva, Switzerland).*
Sept 2013 - Jan 2014	**Intern Student at INFN-Laboratori Nazionali di Frascati LNF**, (Frascati Italy).

Computer skills

Operating Systems	**Unix based systems** (Scientific Linux CERN 4,5,6, Ubuntu), **Microsoft Windows**, **Mac OSX**
Programming Languages	**Python, Matlab**

Languages

Italian	Native
English	Fluent
French	Intermediate

Publications

- A. Romano, O. Boine-Frankenheim, X. Buffat, G. Iadarola and G. Rumolo, "Electron Cloud Buildup Driving Spontaneous Vertical Instabilities of Stored Beams in the LHC", manuscript submitted for publication
- G. Arduini, ..., A. Romano, et al., "High Luminosity LHC: challenges and plans", Journal of Instrumentation 11, C12081 (2016)
- A. Romano, G. Iadarola, K. Li, and G. Rumolo, "Macroparticle Simulation Studies of the LHC Beam Dynamics in the Presence of Electron Cloud", in Proceedings of IPAC'17, Copenhagen, Denmark, 2017
- G. Iadarola, .., A. Romano, et al., "Evolution of Python Tools for the Simulation of Electron Cloud Effects", in Proceedings of IPAC '17, Copenhagen, Denmark, 2017
- A. Romano, G. Iadarola, K. Li, and G. Rumolo, "Effect of the LHC Beam Screen Baffle on the Electron Cloud Buildup", in Proceedings of IPAC'16, Busan, Korea, 2016
- M. Van Gompel, .., A. Romano, et al, "Measurement of the Energy Distribution Function of Electrons Generated by Radio-frequency Induced Multipacting in a Beam Pipe", in Proceedings of IPAC'16, Busan, Korea, 2016
- K. Li, .., A. Romano, et al., "Code development for collective effects", in Proceedings of HB'16, Malmö, Sweden, 2016
- E. Metral .., A. Romano, et al., "Measurement and interpretation of transverse beam instabilities in the CERN Large Hadron Collider (LHC) and extrapolations to HL-LHC", in Proceedings of HB'16, Malmö, Sweden, 2016

Invited Talks

- "A global view on electron cloud instability simulations in the LHC and HL-LHC", will be presented at the ECLOUD18, La Biodola, Italy, 2018
- "Beam stability in the presence of electron cloud", presented at the 7th HL-LHC Collaboration Meeting, Madrid, Spain, 2017
- "How e-cloud in dipoles and quadrupoles can be source of transverse instability?", presented at the ICFA mini-workshop on impedances and beam instabilities in particle accelerators, Benevento, Italy, 2017
- "Instabilities in Stable Beams", presented at the I1/2-day internal review of LHC performance limitations (linked to transverse collective effects) during run II (2015-2016), Geneva, Switzerland, 2016